Novel modeling approaches for the entrained-flow gasification of bio-slurries

A thesis accepted by the Faculty of Aerospace Engineering and Geodesy of the Universität Stuttgart in partial fulfillment of the requirements for the degree of Doctor of Engineering Sciences (Dr.-Ing.)

by

Quentin FRADET

born in Montivilliers, France

Main referee:	Prof. Dr. rer. nat. Uwe RIEDEL
Co-referee:	Prof. Dr.-Ing. Dieter STAPF
Date of defense:	30. June 2020

Institute of Combustion Technology for Aerospace Engineering (IVLR)
Universität Stuttgart

2020

Acknowledgements

This work has been carried out at the Institute of Combustion Technology of the German Aerospace Center (DLR) in Stuttgart under the direction of Prof. Dr. Uwe Riedel. I would like to express my deep gratitude to him for the chance that he gave me and for the guidance throughout this research work. I would also like to thank Prof. Dr. Dieter Stapf from the Karlsruhe Institute of Technology (KIT) for having taken over the co-assessment of this thesis. This work would not have been possible without the scientific cooperation between KIT and DLR, and especially the input of Prof. Dr. Thomas Kolb, Prof. Dr. Nicolaus Dahmen and Dr. Sabine Fleck.

I would like to thank everyone who supported and accompanied me in many ways during my time at the institute. I would also like to acknowledge Dr. Marina Braun-Unkhoff for her supervision and her always fair advises, Dr. Elke Goos for her personal support and Niranjan Fernando for the mutual help and the company at various conferences. My thanks also to Dr. Markus Köhler for his assistance over the last year. Little would have been possible without all the IT support of Dr. Jan Hendrik Starcke and Dietmar Schmitt. Also, many thanks to my seatmates Aziza Kanz and Dr. Torsten Methling. I truly appreciated the time spent together and the daily liter of coffee. For many memorable times, I must also thank, among others, Dr. Mehdi Abbasi and Astrid Ramirez.

Finally, I'm especially grateful towards my family for their understanding and support throughout these years; the visits in Germany were appreciated. And a very special thank to Alice, who provided unwavering encouragement and support.

Contents

List of Figures

List of Tables

List of Abbreviations

BDF	**B**ackward **D**ifferentiation **F**ormula
bpd	**b**arrel **p**er **d**ay
BtL	**B**iomass-**t**o-**L**iquids
CFD	**C**omputational **F**luid **D**ynamics
CFL	**C**ourant–**F**riedrichs–**L**ewy
CGE	**C**old **G**as **E**fficiency
CtL	**C**oal-**t**o-**L**iquids
CV	**C**ontrol **V**olume
DME	**D**i**M**ethyl **E**ther
DNS	**D**irect **N**umerical **S**imulation
DPS	**D**iscrete **P**article **S**imulation
EBM	**E**ddy **D**issipation **M**odel
EE	**E**ulerian–**E**ulerian
EF	**E**ntrained-**F**low
EL	**E**ulerian–**L**agrangian
EG	**E**thylene **G**lycol
FFFB	**F**ree-**F**all **F**ixed-**B**ed
FRC	**F**inite **R**ate **C**hemistry
FVM	**F**inite **V**olume **M**ethods
GC	**G**as **C**hromatography
GFR	**G**as-to-**F**uel **R**atio
GHG	**G**reen**H**ouse **G**ases
GHV	**G**ross **H**eating **V**alue
GLR	**G**as to **L**iquid **R**atio
GtL	**G**as-**t**o-**L**iquids
HHV	**H**igher **H**eating **V**alue

HPLC	**H**igh-**P**erformance **L**iquid **C**hromatography
HVIGasTech	**H**elmholtz **V**irtual **I**nstitute for **Gas**ification **Tech**nology
IPCC	**I**ntergovernmental **P**anel on **C**limate **C**hange
LES	**L**arge **E**ddy **S**imulation
LHV	**L**ower **H**eating **V**alue
MFR	**M**ass **F**low **R**ate
NS	**N**avier-**S**tokes
ODE	**O**rdinary **D**ifferential **E**quations
OpenFOAM	**Open F**ield **O**peration **A**nd **M**anipulation
PaSR	**Pa**rtially **S**tirred **R**eactor
PDE	**P**artial **D**ifferential **E**quations
PDF	**P**robability **D**ensity **F**unctions
PISO	**P**ressure **I**mplicit with **S**plitting **O**perators
pTGA	**p**ressurized **T**hermo**G**ravimetric **A**nalysis
RANS	**R**eynolds-**A**veraged **N**avier-**S**tokes
REGA	**R**esearch **E**ntrained Flow **GA**sifier
SIMPLE	**S**emi **I**mplicit **M**ethod for **P**ressure **L**inked **E**quations
SMD	**S**auter **M**ean **D**iameter
SST	**S**hear **S**tress **T**ransport
STP	**S**tandard **T**emperature and **P**ressure
TCI	**T**urbulence **C**ombustion **I**nteraction
toe	**t**ons of **o**il **e**quivalent
XtL	Anything-**t**o-**L**iquids

List of Symbols

Following nomenclature is used throughout the thesis:

scalars are designated by lightface italic Roman or Greek letters,
vectors by boldface Roman letters or boldface Greek letters,
tensors by double bar boldface Greek letters,
matrices by double bar upper boldface Roman letters,
geometrical elements by upper calligraphic Roman letters.

Adimensional Numbers

Oh	Ohnesorge number
Nu	Nusselt number
Pr	Prandtl number
Pr_t	Turbulent Prandtl number
Re	Reynolds number
Sc	Schmidt number
Sc_t	Turbulent Schmidt number
Sh	Sherwood number
We	Weber number

Greek letters

α_p	Volume fraction of phase p	-
Γ^{Φ}	Diffusion coefficient of Φ	$\mathrm{kg}/(\mathrm{m}\cdot\mathrm{s}^2)$
$\widehat{\Gamma}_p$	Interface mass transfer	$\mathrm{kg}/(\mathrm{m}^3\cdot\mathrm{s})$
$\widehat{\Gamma}_{p,i}$	Interface mass transfer of species i	$\mathrm{kg}/(\mathrm{m}^3\cdot\mathrm{s})$
δ_{ij}	Kronecker delta	-
ε	Average rate of dissipation	$\mathrm{m}^2/\mathrm{s}^3$
$\varepsilon_{\mathrm{EG}}^{slurry}$	Ethylene glycol volume fraction inside a slurry droplet	-
η	Kolmogorov length scale	m
Θ	Ratio representative of intra-class distribution	-
θ_j	Einstein's characteristic temperature	K
λ	Thermal conductivity	$\mathrm{W}/(\mathrm{m}\cdot\mathrm{K})$
μ	Dynamic viscosity	$\mathrm{Pa}\cdot\mathrm{s}$
μ_t	Turbulent viscosity	$\mathrm{Pa}\cdot\mathrm{s}$

μ_x	Solid molar weight variable	g/mol
ν	Kinematic viscosity	m^2/s
ν_{ir}	Stoichiometric coefficient of species i in the reaction r	-
$\nu_{\varsigma r}$	Partial order of species i in the reaction r	-
ρ	Density	kg/m^3
$\overline{\overline{\sigma}}$	Total stress tensor	Pa
σ_g	Geometric standard deviation	-
σ_{lg}	Liquid-gas surface tension	N/m
$[\varsigma]$	Concentration of species ς	mol/m^3
$\overline{\overline{\tau}}$	Deviatoric stress tensor	Pa
$\overline{\overline{\tau}}_t$	Turbulent stress tensor	Pa
τ	Time period larger than the fluctuation time scales	s
τ_c	Chemical time scale	s
τ_t	Turbulent mixing time	s
Υ	Normalized solid mass fraction	-
Φ	Arbitrary intensive variable	$[\Phi]$
$\overline{\Phi}$	Time-averaged component of Φ	$[\Phi]$
Φ'	Time-fluctuating component of Φ	$[\Phi]$
$\widetilde{\Phi}$	Favre-averaged component of Φ	$[\Phi]$
Φ''	Fluctuating component of the Favre averaging	$[\Phi]$
$\widehat{\Phi}$	Volume-averaged component of Φ	$[\Phi]$
$\widehat{\Phi}_p$	Phasic average of Φ	$[\Phi]$
$\langle\Phi\rangle$	Spatial filtering operation on Φ	$[\Phi]$
$\breve{\Phi}$	PDF associated sample space variables	$[\Phi]$
Φ^n	Variable taken at the time t^n	$[\Phi]$
Φ^*	Variable taken at an undefined time t^*	$[\Phi]$
Φ_g	Φ relative to the gas phase	$[\Phi]$
Φ_l	Φ relative to the liquid phase	$[\Phi]$
Φ_{surf}	Φ taken at the droplet surface	$[\Phi]$
Φ_v	Φ relative to a vaporizing species	$[\Phi]$
Φ_∞	Φ taken far away from the droplet surface	$[\Phi]$
ϕ	Equivalence ratio	-
χ	Carbon conversion degree	-
χ_{char}	Char conversion degree	-
ψ	Ratio of the distances $A;F_{AB}$ and $A;B$	-
ω	Rate at which turbulence kinetic energy is converted into internal thermal energy	1/s
$\dot{\omega}_i$	Chemical source term of species i	$kg/(m^3 \cdot s)$

Roman letters

$\overline{\overline{\mathbf{A}}}$	Matrix of the set of equations for implicit schemes	$[\mathbf{A}]$
A	Centroid of the cell C_A	-
A_E	Empirical constant of the Eddy dissipation model	-
A_l	Average droplet surface	m^2
A_r	Pre-exponential factor	$[k] \cdot \mathrm{T}^{-\mathrm{b}}$
A_r^G	Pre-exponential factor of the gasification reaction rate	$1/\mathrm{s}/(\mathrm{mol}/\mathrm{m}^3)^{0.6}$
a	Thermal diffusivity	m^2/s
$a_1, ..., a_7$	NASA polynomial coefficients	$[a_j]$
$a_A^\star$	Coefficient of the implicit terms of the momentum predictor equation of the cell C_A	$[a_A^\star]$
$a_{B_n}^\star$	Coefficient of the implicit terms of the momentum predictor equation of the neighboring cells to C_A	$[a_{B_n}^\star]$
a_t	Turbulent thermal diffusivity	m^2/s
B_E	Empirical constant of the Eddy dissipation model	-
B_M	Mass Spalding number	-
B_n	Centroid of a neighboring cell to C_A	-
$\mathbf{b}$	Vector on the right side of the set of equations for implicit schemes	$[\mathbf{b}]$
$\mathbf{b}_A^n$	Right-hand side explicit source terms excluding the pressure gradient of the momentum predictor equation	$[\mathbf{b}_A^n]$
b	Temperature exponent of the extended Arrhenius equation	-
$b_1, ..., b_7$	NASA polynomial coefficients by mass	$[b_j]$
C_A	Any FVM cell	-
C_B	Cell adjacent to C_A	-
C_d	Drag coefficient	-
C_{mix}	Constant of the PaSR model	-
C_p	Heat capacity	J/K
C_{td}	Model constant of the turbulent dispersion force	-
c	Concentration	$\mathrm{mol}/\mathrm{m}^3$
c_p	Specific heat capacity	$\mathrm{J}/(\mathrm{kg} \cdot \mathrm{K})$
D	Mass diffusivity	m^2/s
D_{50}	Median diameter of the volume size distribution	m
D_{84}	Particle size where 84 % of the particles are smaller	m
D_i^T	Thermal diffusion coefficient of species i	$\mathrm{kg}/(\mathrm{m} \cdot \mathrm{s})$
D_{ik}	Diffusivity of species pair i,k	m^2/s
D_{im}	Diffusivity of species i with the remaining gas mixture	m^2/s
D_x	Solid particle diameter variable	m
E	Total energy by mass	J/kg

E_a	Activation energy	$\mathrm{J/mol}$
E_c	Chemical total energy	$\mathrm{J/kg}$
$\widehat{E}_h$	Heat flux between gas and liquid phase	$\mathrm{J/(m^3 \cdot s)}$
$\widehat{E}_k$	Kinetic energy exchange due to vaporization	$\mathrm{J/(m^3 \cdot s)}$
$\widehat{E}_p$	Interface energy transfer	$\mathrm{J/(m^3 \cdot s)}$
$\widehat{E}_v$	Heat of vaporization	$\mathrm{J/(m^3 \cdot s)}$
e	Internal energy by mass	$\mathrm{J/kg}$
e_c	Chemical internal energy	$\mathrm{J/kg}$
$\mathbf{F}$	Vector force	N
$\mathbf{F}_{l,d}$	Drag force acting on liquid droplets	N
F	Centroid of the face f	-
F_{AB}	Centroid of the common face between C_A and C_B	-
$\mathbf{f}_V$	Volume force	$\mathrm{N/m^3}$
f	Any face of the cell C_A	-
$\mathbf{G}$	Newton-Raphson's function	-
GFR	Gas-to-Fuel Ratio	-
g	Gravitational acceleration	$\mathrm{m/s^2}$
Δg°	Specific Gibbs free energy	$\mathrm{J/kg}$
$\mathbb{H}_p$	Phase indicator function	-
H	Enthalpy	J
$H^\circ_{\mathrm{f},i}$	Enthalpy of formation of species i	$\mathrm{J/kg}$
$\Delta_\mathrm{r} h^\circ$	Standard enthalpy of reaction	$\mathrm{J/kg}$
h_c	Heat transfer coefficient	$\mathrm{W/(m^2 \cdot K)}$
$h^\circ_{\mathrm{f},i}$	Specific enthalpy of formation of species i	$\mathrm{J/kg}$
h_i	Specific enthalpy of single species i	$\mathrm{J/kg}$
h_s	Sensible specific enthalpy	$\mathrm{J/kg}$
$\bar{\bar{\mathbf{I}}}$	Identity matrix of dimension 3	-
$\mathcal{I}$	Inlet/Injected	-
$\mathbf{j}$	Flux of Φ through $\mathscr{S}$	$[\Phi] \cdot \mathrm{kg/(m^2 \cdot s)}$
$\mathbf{j}_i$	Mass diffusion flux of species i	$\mathrm{kg/(m^2 \cdot s)}$
$\mathbf{j}_i^{*,c}$	Molar diffusion flux of species i due to a concentration gradient	$\mathrm{mol/(m^2 \cdot s)}$
$\mathbf{j}_i^c$	Mass diffusion flux of species i due to a concentration gradient	$\mathrm{kg/(m^2 \cdot s)}$
$\mathbf{j}_i^p$	Mass diffusion flux of species i due to a pressure gradient	$\mathrm{kg/(m^2 \cdot s)}$
$\mathbf{j}_i^T$	Mass diffusion flux of species i due to a temperature gradient	$\mathrm{kg/(m^2 \cdot s)}$
$\mathbf{j}_q$	Energy flux due to species diffusion	$\mathrm{J/(m^2 \cdot s)}$

$\bar{\bar{\mathbf{J}}}$	Jacobian matrix	-
k	Kinetic energy	$\mathrm{m}^2/\mathrm{s}^2$
k_r	Kinetic rate constant	$[k]$
k_t	Turbulent kinetic energy	$\mathrm{m}^2/\mathrm{s}^2$
L	Characteristic length	m
L_{vap}	Latent heat	J/kg
l_{sf}	Liter of synthetic fuel	$10^{-3} \cdot \mathrm{m}^3$
$\widehat{\mathbf{M}}_F$	Momentum transfer due to forces acting on droplets	$\mathrm{kg}/(\mathrm{m}^2 \cdot \mathrm{s}^2)$
$\widehat{\mathbf{M}}_p$	Interface momentum transfer	$\mathrm{kg}/(\mathrm{m}^2 \cdot \mathrm{s}^2)$
$\widehat{\mathbf{M}}_v$	Momentum transfer due to mass transfer	$\mathrm{kg}/(\mathrm{m}^2 \cdot \mathrm{s}^2)$
$\mathcal{M}$	Particle mass distribution w.r.t. molar weight	mol/g
M	Average molar weight	g/mol
M_i	Molar weight of species i	g/mol
m	Mass	kg
$\dot{m}_{\mathrm{EG}}^{slurry}$	Evaporation rate of ethylene glycol in the presence of solid	kg/s
$\dot{m}_{\mathrm{EG}}^{pure}$	Evaporation rate of ethylene glycol in the absence of solid	kg/s
m_{inf}	Total mass injected during a time span	kg
$\dot{m}_l$	Mass evaporation rate of one droplet	kg/s
$\dot{m}_{tot}^{slurry}$	Total mass transfer rate of a slurry droplet in the gas phase	kg/s
$\mathcal{N}$	Particle number distribution w.r.t. molar weight	$\mathrm{mol}^2/\mathrm{g}^2$
N_3	Cumulative particle size distribution by volume	-
N_A	Avogadro number	1/mol
N_c	Number of classes for the sectional approach	-
N_i	Number of chemical species	-
N_l	Number of liquid elements	-
N_{R_p}	Number of result points	-
N_r	Number of reactions	-
n_3	Particle size distribution by volume	1/m
n_l	Number density of liquid elements	$1/\mathrm{m}^3$
$\mathcal{O}$	Outlet	-
P	Joint probability density function	$[P]$
p	Pressure	Pa
$(\nabla p)_A^\star$	Corrected pressure gradient	-
p°	Standard pressure	Pa
$p_{v,sat}$	Vapor pressure	Pa
$\dot{Q}^\Phi$	Sinks or Sources of Φ	$[\Phi] \cdot \mathrm{kg}/(\mathrm{m}^3 \cdot \mathrm{s})$
$\dot{Q}_c$	Heat release rate	W/m^3
$\dot{Q}_I^\Phi$	Flux of Φ through $\mathscr{S}_{I,p_i p_j}$	$[\Phi] \cdot \mathrm{kg}/(\mathrm{m}^2 \cdot \mathrm{s})$
$\dot{\mathbf{q}}$	Heat conduction	W/m^2

$\dot{q}_r$	Radiation source term	W/m^3
$\dot{q}_V$	Energy volume sources	W/m^3
R	Ideal gas constant	$J/(K \cdot mol)$
R_l	Average droplet radius	m
R_p	Result points	-
r	Radial distance from the axis of symmetry	m
$d\mathscr{S}$	Any differential area, $\mathscr{S}$ normal outward-pointing at the surface $\mathscr{S}$	m^2
$d\mathscr{S}_A$	Any differential area, normal outward-pointing at the surface $\mathscr{S}_A$	m^2
$\mathscr{S}$	Surface of CV	m^2
$\mathscr{S}_A$	Surface of the cell C_A	m^2
$\mathscr{S}_{I,p_i p_j}$	Interface separating several phases p in the CV	m^2
$\mathscr{S}_p$	Surface of phase p of the CV	m^2
$\mathcal{S}$	Section of the reactor at a distance z from injection	-
S	Entropy	J/K
S_{BIN}	Surface of particle	m^2
S_f	Surface of the face f	m^2
$S_{l,\mathcal{S}}$	Area that occupies the liquid at the section $\mathcal{S}$	m^2
S_r	Rate of reaction r	$mol/(m^3 \cdot s)$
s°	Standard specific entropy	$J/(K \cdot kg)$
Δs°	Standard entropy of reaction	$J/(K \cdot kg)$
T	Temperature	K or °C
T°	Standard temperature	K
T_{ref}	Temperature according to the 1/3-rule	K
$t_{1/2}$	Reaction half-time	s
t	Time	s
Δt	Time step	s
t_η	Kolmogorov time scale	s
$\mathscr{V}$	Volume of CV	m^3
$\mathscr{V}_A$	Volume of the cell C_A	m^3
$\mathscr{V}_p$	Volume of phase p of the CV	m^3
$\dot{V}$	Volumetric flow rate	m^3/s
V_l	Average liquid droplet volume	m^3
$\mathbf{v}$	Velocity	m/s
$\mathbf{v}^\star$	Predicted velocity	-
$\mathbf{v}_m$	Mixture velocity	m/s
$\mathbf{v}_r$	Relative velocity	m/s
v^z	Velocity component in direction z	m/s

X_i	Mole fraction of species i	-
$\mathbf{x}$	Vector position	m
Y_c	Mass fraction of solid contained in the class c	-
Y_{EG}^{slurry}	Ethylene glycol mass fraction in the slurry droplet	-
Y_i	Mass fraction of species i	-
Y_{solid}^{slurry}	Solid mass fraction in the slurry droplet	-
z	Component from coordinate system ($z = 0$ at injection point)	-

Résumé

Nouvelles approches de modélisation pour la gazéification à flux entrainé de bio-suspensions

En limitant l'utilisation des combustibles fossiles et en contribuant à la réduction des gaz à effet de serre, les biocarburants devraient jouer un rôle majeur au cours des prochaines décennies. Les carburants synthétiques produits par des procédés de Biomass-to-Liquid présentent des avantages intrinsèques par rapport aux biocarburants conventionnels. Les matériaux biogéniques inutilisés et de faible qualité, présentant un faible pouvoir calorifique et une teneur élevée en espèces inertes, peuvent être convertis par gazéification, puis par synthèse de carburant, en vecteurs énergétiques de grande valeur. Cependant, les voies de conversion thermochimique sont complexes et ne sont pas encore complètement comprises.

La gazéification à flux entraîné est la technologie la plus prometteuse pour obtenir du gaz de synthèse de haute qualité, avec des quantités minimales d'hydrocarbures et de goudrons. Dans le processus bioliq®, par exemple, un gazéifieur à flux entraîné effectue la conversion de ce qu'on appelle la bio-suspension, qui est un mélange d'huile de pyrolyse et de charbon, provenant du prétraitement décentralisé de la biomasse. La gazéification de la bio-suspension implique un système triphasé à haute température montrant de nombreux sous-processus qui interagissent entre eux, tels que l'atomisation et l'évaporation du liquide, les réactions hétérogènes et la chimie de la phase gazeuse dans des conditions riches. Le défi scientifique majeur est le développement et la validation d'un outil de simulation numérique pour la description mathématique des processus de gazéification à flux entraîné. Des outils de simulation fiables peuvent être utilisés pour la conception et la mise à l'échelle de gazéifieur à flux entraîné technique.

Le but de ce travail est d'étudier une telle description mathématique basée sur de nouvelles approches. Comme l'effort de calcul pour les simulations détaillées est assez élevé, une modélisation fiable mais aussi efficace est recherchée. La modélisation des nombreux sous-processus est abordée.

Tout d'abord, le traitement de la phase gazeuse est présenté. Les bases de la dynamique des fluides constituent le cœur de l'outil numérique. La turbulence et l'oxydation du carburant doivent être prises en compte, elles sont importantes pour l'interaction de la chimie et de l'écoulement. Ensuite, la modélisation de

la phase liquide est présentée. Une approache eulérienne à deux phases est développée, avec de l'éthylène glycol comme substitut pour l'huile de pyrolyse. Enfin, une approche par section appliquée à la conversion des solides est proposée. Cette approche prend en compte la distribution granulométrique du solide, sa composition et également son évolution, du charbon initial aux cendres résiduelles.

Dans la dernière partie, l'outil numérique développé est comparé aux données expérimentales du gazéifieur atmosphérique de laboratoire REGA exploité au Karlsruhe Institute of Technology. La validation réussie des résultats obtenus avec l'outil numérique proposé est effectuée pour différents coefficients d'équivalence et également pour deux types de solides, du charbon de bois et de paille. Enfin, l'outil validé est utilisé sur des plages étendues de conditions de fonctionnement dans le but de maximiser l'efficacité du gazéifieur et de minimiser la formation de polluants.

Kurzfassung

Neuartige Modellierungsansätze für die Flugstromvergasung von Bioslurries

Biokraftstoffe werden in den nächsten Jahrzehnten voraussichtlich eine wichtige Rolle spielen. Sie können den Einsatz fossiler Brennstoffe reduzieren und zur Minderung von Treibhausgasen beitragen. Synthetische Kraftstoffe, die durch Biomass-to-Liquid-Verfahren hergestellt werden, bieten im Vergleich zu herkömmlichen Biokraftstoffen inhärente Vorteile. Reststoffe und minderwertiges biogenes Material mit niedrigem Heizwert und hohem Gehalt an inerten Spezies können durch durch Vergasungsprozesse mit anschließender Kraftstoffsynthese in wertvolle Energieträger umgewandelt werden.

Flugstromvergasung ist dabei die vielversprechendste Technologie, um hochwertiges Synthesegas mit minimalen Mengen an Kohlenwasserstoffen und Teeren zu erzielen. Im Bioliq®-Verfahren erfolgt beispielsweise die Umwandlung sogenannter Bioslurries in einem Hochdruckflugstromvergaser. Bioslurries sind eine Mischung aus Pyrolyseöl und Biokohle, die aus der dezentralen Vorbehandlung von Biomasse entsteht. Bei der Bioslurry-Vergasung handelt es sich um ein dreiphasiges Hochtemperaturverfahren mit zahlreichen wechselwirkenden Teilprozessen, wie der Zerstäubung und Verdampfung von Flüssigkeiten, dem Ablauf von chemischen Reaktionen an der Oberfläche von Feststoffen und in der Gasphase unter brennstoffreichen Reaktionsbedingungen. Eine wesentliche wissenschaftliche Herausforderung ist die Entwicklung und Validierung von numerischen Simulationstools für die mathematische Beschreibung der Flugstromvergasungsverfahren. Zuverlässige Simulationswerkzeuge können für das Design und für die Skalierung eines technischen Flugstromvergasers eingesetzt werden.

Das Ziel der vorliegenden Arbeit ist die Untersuchung der mathematischen Beschreibung eines Flugstromvergasers auf Basis neuartiger numerischer Ansätze. Da der Rechenaufwand für detaillierte Simulationen sehr hoch ist, wird eine zuverlässige, aber auch effiziente Modellierung angestrebt. Die Modellierung aller relevanten Teilprozesse wird berücksichtig.

Zunächst wird die Behandlung der Gasphase vorgestellt. Die Grundlagen der Strömungslehre bilden das Kernstück des numerischen Werkzeugs. Turbulenz und die Oxidation des Brennstoffs müssen auch berücksichtigt werden, da beide wichtig sind für die Wechselwirkung von Chemie und Strömung. Dann

wird die Modellierung der flüssigen Phase vorgestellt. Ein zweiphasiges Euler'sches Modell wird entwickelt, mit Ethylenglykol als Surrogat für Pyrolyseöl. Schließlich wird ein Sektionalansatz für die Umwandlung von Feststoffen vorgeschlagen. Dieser Ansatz berücksichtigt die Feststoffgrößenverteilung, ihre Zusammensetzung und auch ihre Umwandlung von der Ausgangskohle bis zur Restasche.

Im letzten Teil der Arbeit wird das Vorhersagekraft des entwickelten numerischen Tools mit experimentellen Daten des atmosphärischen Laborvergasers REGA des Karlsruher Instituts für Technologie überprüft. Erfolgreiche Validierungen werden für unterschiedliche Äquivalenzverhältnisse sowie für zwei Arten von Feststoffen durchgeführt, nämlich Holzkohle und Kohle aus Stroh. Schließlich wird das validierte Werkzeug über einen erweiterten Bereich von Betriebsbedingungen angewandt, um die Effizienz des Vergasers zu maximieren und die Schadstoffentstehung zu minimieren.

Abstract

Novel modeling approaches for the entrained-flow gasification of bio-slurries

By limiting the use of fossil fuels and contributing to the mitigation of greenhouse gases, biofuels are expected to play a major role over the next decades. Synthetic fuels produced by Biomass-to-Liquid processes show inherent benefits when compared to conventional biofuels. Unused and low-grade biogenic materials, featuring low calorific value and high content of inert species, can be converted through gasification followed by fuel synthesis into highly valuable energy carriers. However, the thermo-chemical conversion paths are complex and not yet fully understood.

Entrained-flow gasification is the most promising technology to obtain a high quality syngas, with minimum amounts of hydrocarbons and tars. In the bioliq® process, for instance, an entrained-flow gasifier performs the conversion of a so-called bio-slurry, which is a mixture of pyrolysis oil and biochar, originating from the decentralized pretreatment of biomass. The bio-slurry gasification involves a three-phase high temperature system showing numerous interacting sub-processes, such as liquid atomization and evaporation, heterogeneous reactions, and gas phase chemistry under rich conditions. The major scientific challenge is the development and validation of a numerical simulation tool for the mathematical description of entrained-flow gasification processes. Reliable simulation tools can be used for the design and scale-up of technical entrained-flow gasifiers.

The purpose of the present work is to investigate such mathematical description based on novel approaches. As the computational effort for detailed simulations is quite high, reliable but also efficient modeling is sought. The modeling of the numerous sub-processes is addressed.

First, the treatment of the gas phase is presented. The basics of fluid dynamics constitute the core of the numerical tool. Turbulence and fuel oxidation have to be considered, they are important for the interplay of chemistry and flow. Then, the modeling of the liquid phase is presented. A two-phase Eulerian approach is developed, with ethylene glycol as a surrogate for pyrolysis oil. Finally, a sectional approach applied to the conversion of char is proposed. This approach takes into account the solid size distribution, its composition and also its evolution, from the initial char to the residual ashes.

In the last part, the developed numerical tool is compared to experimental data from the atmospheric lab-scale gasifier REGA operated at Karlsruhe Institute of Technology. Successful validation of the results obtained with the proposed numerical tool is performed for distinct equivalence ratios and also with two types of solids, char originating from wood and from straw. Finally, the validated tool is used over extended ranges of operating conditions in an attempt to maximize the gasifier efficiency and to minimize the pollutant formation.

Chapter 1

Introduction

1.1 Synthetic fuels

1.1.1 Synthesis routes

A single definition of synthetic fuels does not exist. The broadest definition encompasses all fuels, gaseous or liquid, that are derived from petroleum substitute [1]. In some context, however, synthetic fuels only designate liquid fuels, similar to traditional gasoline, diesel, or kerosene, obtained from the conversion of syngas [2]. These synthetic fuels are produced in an indirect, multi-step process that includes syngas production and syngas conversion. Depending on the initial feedstock for the syngas production, this process is designated **C**oal-**t**o-**L**iquids (**CtL**), **G**as-**t**o-**L**iquids (**GtL**), **B**iomass-**t**o-**L**iquids (**BtL**), or Anything-**t**o-**L**iquids (**XtL**) generically. In the following, the fuels obtained with syngas will be referred to XtL fuels to make a distinction with other types of synthetic fuels.

As mentioned above, XtL fuels are obtained after two distinct and successive stages, the syngas production and the syngas conversion.

The syngas production depends on the feedstock. Coal and biomass are solid materials and can be both converted through gasification [3], i.e. the carbonaceous material is partially oxidized to form carbon monoxide and hydrogen. GtL-fuels are obtained from natural gas. Methane, the main component of natural gas, can be converted into syngas through steam reforming [4].

The syngas conversion is independent on the initial feedstock. Only the ratio of carbon monoxide and hydrogen and the technology employed will play a role for the final product. Two main roads [5] are commonly used for the fuel synthesis, the Fischer-Tropsch process [6] and the Methanol-to-Gasoline process [7], also called Mobil process. The Fischer-Tropsch synthesis is a catalytic (cobalt or

iron) conversion of the syngas into wide range of hydrocarbons, mainly alkanes, ranging from methane to waxes. The product distribution depends on the operating conditions, mainly the temperature, the pressure, and the $H_2 : CO$ ratio. Due to the low product selectivity, a refining step follows. The second road to synthetic fuels production is the Methanol-to-Gasoline process [8]. This process uses methanol as an intermediate. The methanol is formed from the low-pressure reaction of syngas. This reaction achieves very high yields with a Copper-Zinc Oxide catalyst. The methanol is further converted into gasoline in the presence of a zeolite catalyst. Several mechanisms have been proposed [9], which include **D**i**M**ethyl **E**ther (**DME**) as an intermediate.

Synthesis of fuels is not a novel concept, since it has been achieved as soon as 1913 by Friedrich Bergius [10] in a direct coal conversion into liquid fuel. The Fischer-Tropsch process itself was developed in 1925 [11]. Coal liquefaction, that is direct, as in the Bergius process, or indirect in CtL processes, presents the advantage to not rely on petroleum. For this reason, the interest in synthetic fuels rises in case of petroleum unavailability or increase of crude oil prices. For these reasons, peak of synthetic fuel production of the 20^{th} century happened during second world war. Germany that had no petroleum stocks, but possessed abundant coal reserves, exceeded a production of 100,000 **b**arrels **p**er **d**ay (**bpd**) (42 million barrels in 1943 [12]). Correlation between scientific research on Fischer-Tropsch synthesis and oil price has been shown in [6] (Figure 4). In 2014, the worldwide production is only around thrice that of the precedent peak, with a daily production of 400,000 bpd [13]; a figure to put in perspective with the oil refinery throughput of 82 millions barrels per day in 2017 [14]. Most of the synthetic fuel produced is CtL-fuel. However, the last few years have shown a regain of interest for these processes with many projects in the planning stage or under construction.

1.1.2 Biomass-to-Liquid

Biomass-to-Liquid fuels are only marginally produced, though they could play a bigger role in the context of **G**reen**h**ouse **G**ases (**GHG**) reduction. If all XtL fuels have the benefit to substitute petroleum dependency, only BtL fuels have the possibility to be carbon neutral along the whole process chain.

The **I**ntergovernmental **P**anel on **C**limate **C**hange (**IPCC**) [15] is an intergovernmental organization for assessing the science related to climate change.

Anthropogenic GHG emissions increase the global temperature relative to pre-industrial levels. It has been stated in 2015 in the Paris Agreement [16] that the long-term goal is to hold this temperature increase to well below 2 °C and to pursue efforts to limit it to 1.5 °C. Holding this rise to 1.5 °C would reduce the worst impacts of climate change of a rise by even 2 °C, such as extreme drought, temperature extremes, or ecosystem (terrestrial, freshwater, wetland, coastal and ocean) degradation [17]. The IPCC showed that limiting the global warming to below 2 °C *reaching net zero CO_2 emissions globally around 2050*. Mitigation scenarios based on different GHG emission pathways that would limit the global warming to 1.5 °C have been elaborated [17]. Theses scenarios point out the role that bioenergy has to play.

Bioenergy comprises all energy derived from biogenic resources. By analogy, biofuels designate combustible materials derived from biogenic resources. We distinguish biofuels according to its feedstock or the process used:

- First-generation biofuels or conventional biofuels are made from dedicated food crops.
- Second-generation biofuels or advanced biofuels are made from non-food biomass.
- Third and fourth-generation biofuels are produced on non-arable lands, i.e. algae fuels.

Biofuels in general have pros and cons, and not all biofuels perform equally. On the one hand, they have the capacity to provide high amount of energy while mitigating emissions, to promote rural development while being economically efficient. On the other hand, the growing demand on biofuels – 11.4 % world wide growth rate per annum for the period 2006-2016 [14] – can have harmful effects, including competition between food and fuel or expansion of land use that support biodiversity. For these reasons, biofuels must meet standards that are assessed throughout the analysis of the entire life-cycle.

Second-generation biofuels, such as BtL fuels, have the advantage not to compete with the production of food crops. Many feedstocks are therefore usable, such as woody crops, agricultural residues or municipal wastes. In fact, any organic material is theoretically convertible with the adequate technology. This advantage of feedstock flexibility has a counterbalance: the material has a lower energy content and its conversion is often more complex (due to lignin for example). The conversion requires a more advanced technology, with thermochemical routes for example.

Today, biofuels are already a major actor in the transportation sector, with an annual production of 84 millions **t**ons of **o**il **e**quivalent (**toe**) in 2017 [14]. It represents 3 % of the total transport consumption [18]. In Germany, the part of energy from biofuel was 4.9 % in 2018 [19] (5.6 % from renewable sources if we include electrical vehicles), and target objectives have been defined for the next decades. According to the so-called "Klimaschutz 2050", the contribution of the transportation sector to GHG should be reduced to 40-42 % as compared to 1990 [20]. The same trend is expected globally. Nowadays, the market is dominated by two products, bioethanol and biodiesel. Both are first-generation biofuels. Bioethanol is mainly produced by microbial fermentation of sugar. Biodiesel is produced by chemically reacting lipids with an alcohol producing fatty acid esters.

As we have seen, BtL fuels are not commercialized at large scale, despite the fact that the technology is old. Two reasons can explain this. First, no major technological break-through happened, nor for the syngas production, nor for the syngas conversion. Second, the competition with other sources, e.g. the reliance of the well implemented oil industry and the other types of biofuels with conversion easier to perform. However, many R&D projects are underway in this domain because BtL fuels have a high estimated potential. As mentioned above, using non-edible feedstocks, it can convert very low energetic materials. The final product is also of interest. Unlike bioethanol and biodiesel, BtL fuels are very close to conventional gasoil or diesel, with a very high energy content and can also be used as jet–fuel. Unlike conventional gasoil or diesel, the fuel contains almost no sulfur and fewer aromatics [21]. The potential of a large deployment of biodiesel based on gasification and Fischer-Tropsch synthesis was estimated to be around 6.1 $GtCO_2$ storage on an annual basis in 2050 [22]. It would represent a large reduction when compared to the global CO_2 emissions, which amounted 30.6 $GtCO_2$ in 2010.

Many pilot and demonstration projects have been achieved or are planned. Some projects were not successful, but new ones are undergoing. Choren was the first enterprise that aimed at commercializing BtL fuels from forest residues. The objective was a production of 15,000 tons of fuels per year (347 bpd) starting from 2009. However, the German company went insolvent 2 years later [23]. Other projects have been discontinued for different reasons. Piteå Black Liquor Gasification to DME of Chemrec shut down in 2016 after running for 5 years, NSE biofuels Oy did not get the EU's NER 300 funding [24]. The Forest BtL project [25] planned in 2014 to produce 130,000 t/a (3,000 bpd) for Ajos in Kemi (Finland) with the Choren gasification technology, but a partner withdraw from

the project, the reasoning given was that *EU's climate and energy strategy published in January did not agree on new binding limits for the share of the renewable component in traffic fuels after 2020* [26]. This project has known a renewal in 2016 with the investment of 1 billion € from China's bioenergy giant Kaidi [27] to build the plant in Kemi. They also received funding from the EU's NER 300 of 88 millions € [28] and was supposed to be operational in 2019 for a production of over 200,000 t/a.

Two strategies are possible to scale-up the capacity of production. It can be a multiplication of small units to adapt to local needs. This has shown good results in methanation units for example. This solution is more difficult to apply for complex processes. The second possibility is to scale-up the facility. Figure 1.1 shows an estimation of the cost of one liter BtL fuel for different sizes; the details of these estimations can be found in Appendix A. A biomass throughput of 10, 100 and 1,000 MW_{th} was considered, with corresponds to a production of about 85, 850 and 8,500 bpd.

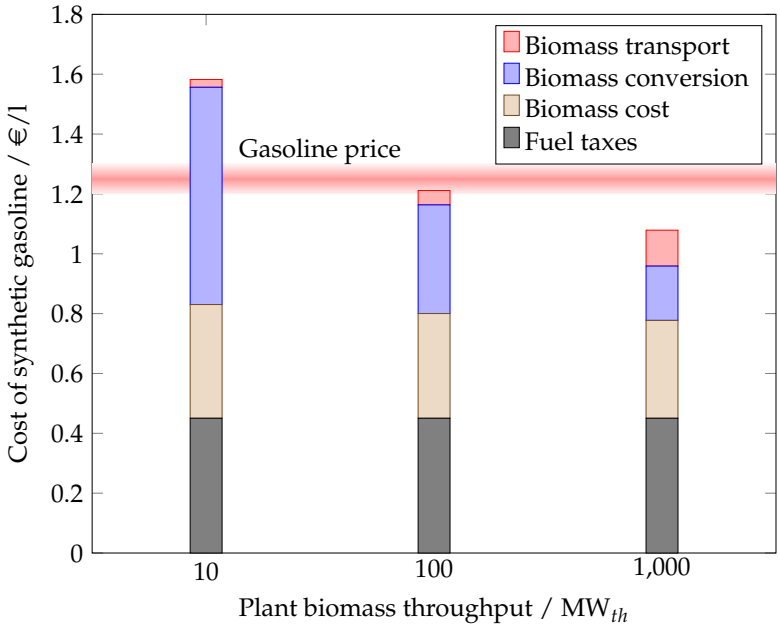

FIGURE 1.1: Estimation of the cost of one liter BtL fuel for various plant sizes; the calculations are detailed in Appendix A

The calculations are performed based on a regular biomass gasification technology. Some costs are irreducible (taxes) or decrease slightly by scaling up (biomass cost). However, significant costs reduction in term of biomass conversion can be obtained by scaling up. The case with the smallest throughput is well under a commercial scale, and as shown in Figure 1.1, the associated costs are too high. Scaling up by a factor of ten reduces the conversion costs by about

a factor two. But, as a side effect, the transport cost increases. The biggest plant requires a higher amount of biomass throughput that has therefore to be conveyed from greater distance.

This is a reason why the number of large-scale facilities of second-generation biofuels is not expanding. The gain associated to a facility scale-up is too small in comparison with the associated investment. The transport of low energy density material like straw bale is very costly. Also, the material cannot usually be collected at a central place but has to be conveyed from a multitude of distributed sites. The bioliq® process is a concept that attempts to solve this issue and be able to scale-up the usage of BtL.

1.2 The bioliq process

1.2.1 Principle

The idea behind the bioliq® process is to perform a liquefaction of the lignocellulosic biomass directly where the biomass is found, and then to convey the transformed material to a central plant for the gasification and fuel synthesis. The process steps can be seen in Figure 1.2. The terms *centralized* and *decentralized* describe if the step is performed at a single central facility or at distributed regional places. Thus, the bioliq® process can be divided in two parts, a decentralized and a centralized part.

The *decentralized* part of the bioliq® process aims at performing a primary conversion of the biomass to ease its transportation. It is achieved with the fast pyrolysis of biomass that produces pyrolysis oil and char.

The low-grade energy resources considered for this process is typically wood residues and straw, as they constitute together two-thirds of the unused non-food biomass [30]. Forest residues cover a wide range of material left during forest thinning or felling. It can consist of barks, branches, tops, but also leaves for deciduous trees and needles for coniferous trees. Four potential examples of forest and agricultural residues for BtL production are illustrated in Table 1.1. The **H**igher **H**eating **V**alue (**HHV**) is a measure often used to estimate the amount of heat that the complete combustion of the fuel will produce, the end-product water being considered in the liquid state. This value is determined experimentally in a bomb calorimeter. Typically, wood residues and straw have a HHV of about 18 MJ/kg. However, these figures are always given on a dry basis. The

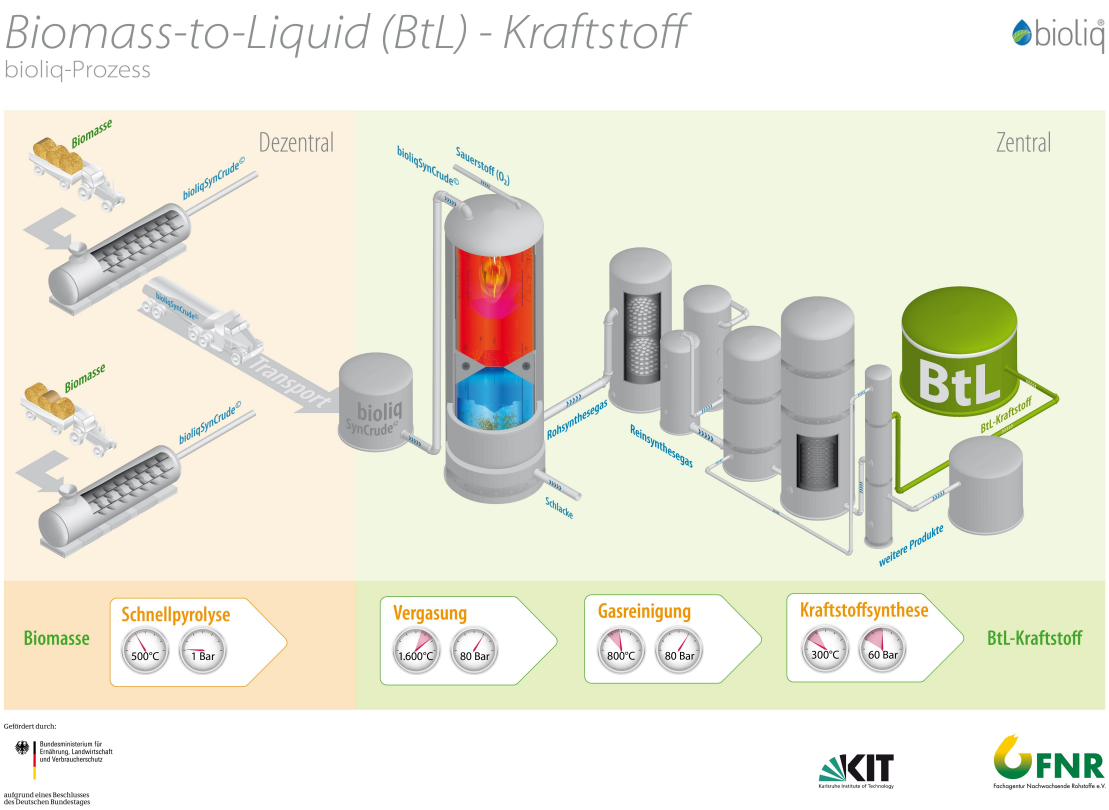

FIGURE 1.2: Schematic overview of a BtL manufacturing process (picture taken from Fachagentur Nachwachsende Rohstoffe e.V. [29])

freshly-harvested biomass can have a high moisture content, lowering its true energy and economic potential [31]. The **G**ross **H**eating **V**alue (**GHV**) is a better indicator [32] as it is calculated on a wet basis. GHV and HHV are connected by the relation $\mathrm{GHV} = \mathrm{HHV}\,(1 - \%_{moisture})$. Forest residues have a varying moisture content that can reach up to 60 %. This is not so substantial for straw, with an average value of 15 %. However, straw density is considerably low, for example 140 $\mathrm{kg/m^3}$ for block bales. Forest residues density is somewhat higher, but also depends on many parameters. All in all, the energy density, i.e. the calorific value per volume, of both materials is similar and very low, at around 2 $\mathrm{GJ/m^3}$ (Table 1.1).

As pointed out in the first part, this low energy density results in high transportation costs, hence there is an advantage to convert the raw material locally. The pyrolysis of lignocelullosic biomass yields a gas phase, liquid compounds, and a solid part. The products distribution depends strongly on the process conditions and type of biomass. Terminology used for the liquid includes pyrolysis oil, bio-oil but also pyrolytic oil and biocrude, while the solid is denoted char, charcoal or biochar. Mixed together, pyrolysis oil and char form a slurry or a

TABLE 1.1: Typical physical properties of initial, intermediate and final products in the bioliq® process

	Forest residues [33]		Straw [33]		Fast pyrolysis products [34]			End-product [35]
	Spruce (coniferous)	Beech (deciduous)	Wheat	Rice	Bio-oil	Char	Slurry	BtL fuel
HHV $[MJ/kg]$	18.8	18.4	17.2	12.0	20.5	26.4	21.9	46
Moisture content [%]	50	50	15	15	21	4.4	17.7	-
GHV $[MJ/kg]$	9.4	9.2	14.6	10.2	16.2	25.2	18.0	46
Bulk density $[kg/m^3]$	195	260	140	140	1220	538	1270	780
GHV $[GJ/m^3]$	1.8	2.4	2.0	1.2	19.8	13.6	23.2	36

paste that is called bioSyncrude in the bioliq® process.

Similar analysis of the calorific value to the one performed for the biomass residues can be done for the pyrolysis products. The example shown in Table 1.1 is taken from the pyrolysis of mallee [34], a woody biomass. As reported, the HHVs of pyrolysis oil and biochar expressed by mass are only slightly higher than those of wood and straw. Despite important moisture content, bio-oil presents a high energy density of $18 - 25\ GJ/m^3$ due to its important bulk density. Biochar is not a dense solid due to its high porosity. It is however compensated by its low moisture content and high HHV by mass. The preparation of the slurry assures the best use of both pyrolysis products. The liquid fills the pores the solid particles, leading to a density of the new material higher than those of both components taken separately. This new product, to be conveyed to the central plant, shows an energy density much greater than the initial feedstocks. The factor of energy densification is case dependent. It varies according to the type of biomass, in which state it is pyrolyzed (for example if the biomass has been pre-dried). It also depends on the process conditions, and especially of the ratio liquid/solid of the slurry. Taken a biomass of very low energy density as in the example shown in Table 1.1, and a slurry that exceed $20\ GJ/m^3$, the energy densification is therefore greater than a factor of ten.

The higher energy density is not the only advantage of the slurry. It can be pumped, facilitating the storage and transport. It is also noticeable that biochar powder can easily self-ignite as well as penetrate breathing masks. The slurry preparation prevents these problems by trapping the particles in the oil.

Although many pyrolysis technologies are being developed, the attention will be restricted to the investigations led at KIT in the following. In the bioliq® process, fast pyrolysis is performed. *Pyrolysis* stands for the thermal decomposition under inert atmosphere (absence of an oxidant) while *fast* stands for very

high heating rates [36]. Fast pyrolysis of biomass generates a majority of pyrolysis oil by opposition to slow pyrolysis where the fraction of charcoal and gas is higher or even the only products [37].

Parallel to investigations on various woods and straw in a bench-scale pyrolyser ($5 - 10$ kg/h), a pilot plant (500 kg/h) was contracted to Air Liquide (former Lurgi). A detailed description of the bioliq® fast pyrolysis pilot plant can be found in Pfitzer et al. [38]; the pyrolysis of wheat straw is presented. The biomass conversion takes place in a twin screw mixer reactor (also called auger reactor). Prior to entering the reactor, the pre-dried biomass is cut to smaller particles and impurities are removed. The biomass is fed in the reactor simultaneously with heated sand. The cold biogenic material is quickly warmed by the mixing with the hot heat carrier. This carries the high heating rates necessary for fast pyrolysis [39]. Fast pyrolysis is also characterized by a short residence time and a reactor temperature of about 500 °C [36]. The short residence time is obtained here with a compact reactor design and a high rotation speed. The reactor temperature of 500 °C is achieved by injecting the sand at a slightly higher temperature. Straw or other lignocellulosic materials decompose into vapors, aerosol and charcoal. Some of the biochar is lost at the heat carrier outlet, even if some heat is gained with the combustion of this residual solid.

The valuable products, the gas and the remaining char, leave the reactor overhead. The char is separated from the gas in a cyclone. The gas is composed of condensable and non-condensable species. The condensate obtained after cooling corresponds to our desired bio-oil. A particularity of the present pilot plant is to perform two condensation steps, forming two condensates. The vapors and gases enter a first condenser at 90 °C. The so-called organic condensate is obtained. On top of this first condenser, an electrostatic precipitator removes the aerosols from the remaining vapors and gases. The second condensation step, performed at 30 °C, gives an aqueous condensate. The incondensable gases can provide heat to the system in an optimized process [40]. Three valuable products are therefore obtained after the fast pyrolysis of biomass, charcoal, an organic condensate and an aqueous condensate. Typical distribution of these products for wheat straw is 30/40/30 %, respectively. The tar condensate contains around 10 % of solids and also 15 % of water. The aqueous condensate is mostly composed of water, around 80 %, without the presence of a solid. The organic condensate is of higher energy content than the aqueous condensate due to the difference in water content. Nevertheless, the aqueous condensate is also valuable, a slurry containing up to 40 % of solids can be prepared, against 20 % for the organic condensate. Both slurries are intended for gasification.

Although early estimations projected more than 20 pyrolysis plants for one gasifier [41], recent and advanced techno-economic studies find an optimal ratio of ten fast pyrolysis units [42] for one central gasification plant.

The *centralized* part of the bioliq® process aims at performing a second conversion of the biomass to obtain high-quality transportation fuel. This is done in three steps: gasification of the bio-slurry, gas cleaning, and fuel synthesis.

The gasification step has the objective to convert the bioslurries into syngas. Gasification is a partial oxidation of the fuel at high temperature. The chosen technology is pressurized **E**ntrained-**F**low gasification. Insight of this technology and its novelty is further detailed in the next section. The EF gasifier of the bioliq® plant has a 5 MW capacity, or 1 t/h, operates between 1,200 and 1,600 °C and can reach a pressure up to 80 bars. The gas leaving the reactor mainly contains syngas (hydrogen and carbon monoxide), carbon dioxide, water and nitrogen. Almost no soot, methane and tars are obtained.

A step of gas cleaning and conditioning is necessary prior to the fuel synthesis. Indeed, catalysts for fuel synthesis are easily poisoned by impurities. The threshold is very strict with a maximum of 0.1 ppmv for all pollutants. This step is performed at high temperature (from 500 °C to 800 °C) and pressure (up to 80 bars), and can be decomposed into four stages. In the first stage, ceramic filter elements remove particulates from the hot syngas. The second stage cleans the gas from gaseous acids, such as HCl, H_2S, or COS, in a fixed bed sorption. In the third stage, a catalytic reactor decomposes any organics or compounds containing nitrogen (ammonia, cyanides). The fourth stage separates CO_2 from the gas in a conventional Selexol scrubber. While not part of the actual plant, it is also possible to optimize the H_2/CO ratio before the fuel synthesis. It can be done by water addition through the shift reaction, though more CO_2 is then produced. An alternative is to inject pure hydrogen from another source. For example, the Winddiesel technology [43] combines the CO-rich syngas from lignocellulosic feedstock gasification and the H_2 produced by electrolysis.

The last step proceeds to synthesize the fuel. The process takes fully advantage that the gas is at very high pressure due to the gasifier operating conditions. While Fischer-Tropsch syntheses are performed up to 35 bars (above, the catalyst activity decreases [44]), the present method can go up to 80 bars. It avoids a costly additional compression of the gas. The method employed is close to the Methanol-to-Gasoline process. Methanol is formed and immediately dehydrated to produce DME, with a Cu/Al_2O_3 catalyst. Finally, gasoline is obtained by the reaction of DME with a zeolite catalyst.

1.2.2 Entrained-flow gasification of bio-slurry

Gasification is the central element of the bioliq® process. It is the step that must process the highest fluxes, at the highest temperature and pressure. It is also certainly the most unknown and complex to design. While fuel synthesis is a matured technology, as seen in the first part, the high-pressure entrained-flow gasification of bio-slurry is a new concept. The challenges are numerous to convert a low-grade fuel like bio-slurry, whose composition and energy content can vary greatly, in a high-quality syngas, with good process efficiency.

HVIGasTech [45] (**H**elmholtz **V**irtual **I**nstitute for **Gas**ification **Tech**nology) aims at investigating the gasification process of solid/liquid fuel in an entrained-flow reactor. Experimental and fundamental works are conducted for a better understanding and a mathematical description of the process.

In an EF gasifier, the fuel is injected concurrently with the gasification medium. The gasification medium can be oxygen, enriched air or steam. A principle scheme of the high-pressure EF gasifier of the bioliq® process can be seen in Figure 1.3. The fuel considered here is bioSyncrude, thus the slurry is injected by atomization at the reactor inlet. In case of a solid fuel, it is finely pulverized before injection. Together, fuel and oxidant form a turbulent flame leading to temperature above 1,200 °C where gasification occurs. Ash contained in the fuel melts at these temperatures. The slag formed and the syngas produced are cooled in the quench water at the bottom of the reactor.

EF gasification has been preferred to other gasifier technologies like fixed-bed gasifier or fluidized-bed gasifier because it presents advantages regarding feedstock flexibility, throughput capacity, and output quality.

- Feedstock flexibility: an EF gasifier can convert fuel in any form, powder, liquid or gas. In our case the fuel could be a slurry, or biochar/bio-oil separately. It requires only an adequate burner head and conveying system, pump/compressor. The feedstock quality does not need to be high, a higher heating value greater than 10 MJ/kg being sufficient [41].

- Throughput capacity: pressurized EF gasification is an optimal technology to process large quantities of feedstock. Gasifiers with a capacity larger than 1 GW_{th} can be designed. This high throughput capacity is due to the high temperature and pressure leading to short conversion times and compact reactors.

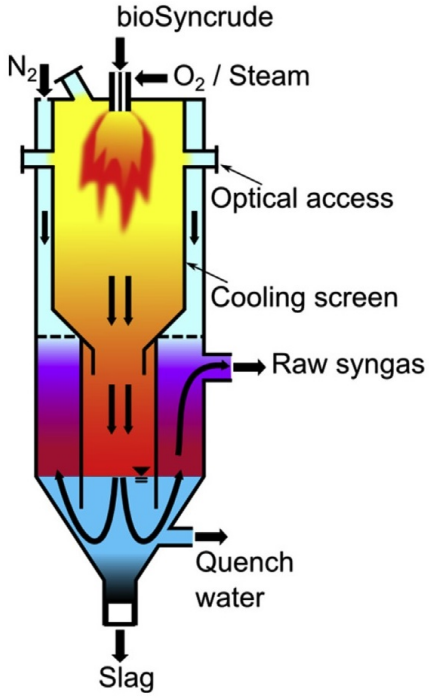

FIGURE 1.3: bioliq® high-pressure entrained-flow gasifier (image taken from Kolb et al. [46])

- Output quality: EF gasification shows the best syngas quality of all existing gasification technologies. This is particularly important for the succeeding fuel synthesis. The raw syngas is almost tar-free and shows low methane content. Carbon conversion is almost total, with values greater than 99 %, which can even reach 99.9 % [47]. The ash is also withdrawn from the exiting gas stream because at these temperature conditions, the ash melts and forms a slag layer on the walls that drains down to the bottom of the gasifier.

This technology, nevertheless, presents inherent disadvantages. One requirement concerns the feed preparation. In case of solid fuel gasification, the dry feedstock is conveyed by pneumatic transfer via a lock-hopper. This system shows limitations in the maximal permissible pressure [48]. Also, the solid has to be pulverized to micron-sized particles, a source of risks regarding self-ignition and dust explosion. Recently, on July 19^{th}, 2019, an explosion killed 15 people in the Yima coal gasification plant in China. The causes for this explosion are still uncertain [49]. These important safety risks explain why, even with coal gasification, a water slurry is usually prepared. A wet transfer with a pump-system

is safer, but also technically simpler and economically cheaper. Other disadvantages of this type of gasifier is the greater oxygen content needed in order to yield the high syngas quality. Also, the heat loss is non-negligible through the wall made of a thin membrane. The scaling-up reduces this loss by diminishing the ratio of surface to volume of the reactor. To summarize, due to the advantages and disadvantages mentioned above, EF gasification is suited for high throughput only.

Entrained-flow gasification is nowadays the most widely employed gasification type, mainly for coal gasification [50]. The design of gasifiers is mainly based on practical experiences, as well as basic models [46]. For example the syngas composition can coarsely be estimated by the water-gas shift equilibrium constant, knowing the reactor temperature. It is clear that the development of high-fidelity simulation tools would accelerate this technology spread. Especially for BtL fuels that need a breakthrough to compete with other conventional fuels or biofuels. Those simulation tools can provide process optimization and help design and scale-up reactors. However, the sub-processes involved in a pressurized EF gasifier are numerous and complex. An overview of the in detail phenomena occurring in case of bioslurry gasification is given below.

Bio-slurry atomization

We consider the case of high-pressure EF gasification of bio-slurry typical to bioliq® process conditions. Thus, the solid represents a minor part of the slurry. We inject a highly viscous suspension. The first major modeling challenge concerns the spray description. It is a somehow matured field of research [51], mainly due to high investigation efforts in internal combustion engines [52]. Typically, two regions are identified, the spray formation region and the spray region [53]. In the first region, the challenge lies in capturing the successive steps from the bulk liquid at the injection orifice to the small droplets characteristic of the second region. The liquid jet will disintegrate into large drops under the effect of disruptive forces [54]. Theses drops are generally of consequent sizes and thus instable. They undergo a second breakup that produces smaller droplets [55]. We usually distinguish between primary and secondary atomization [51]. Both the jet breakup and the drops breakup are governed by the action of internal and external disruptive forces over the consolidating surface tension. On the one side, the surface tension pulls the liquid in the forms of a sphere to minimize the surface energy. On the other side, aerodynamic forces and liquid primary disturbance deform the liquid, which can lead to its breakup. Thus, the

Weber number, a dimensionless number defined as the ratio between the liquid inertia to its surface tension, is a key parameter for determining jet and drop behavior. For the primary breakup, the Ohnesorge number is also of importance because it accounts for the viscous force of the liquid. For a same nozzle, higher inertial forces are required for the breakup of a highly viscous fluid. Weber (We) and Ohnesorge (Oh) numbers are given by:

$$\mathrm{We} = \frac{\rho_l v_l^2 L}{\sigma_{lg}} \quad \& \quad \mathrm{Oh} = \frac{\sqrt{\mathrm{We}}}{\mathrm{Re}} = \frac{\mu_l}{\sqrt{\rho_l \sigma_{lg} L}}. \tag{1.1}$$

Different regimes can be identified for the primary and secondary breakup based on these numbers [56]. Besides breakup, droplets can also collide and coalesce to form larger droplets, which can also subsequently undergo secondary atomization. In the spray region, far from the nozzle injection zone, the droplets are well-formed, small and spherical. Other parameters characterizing the spray are the size distribution, the droplet number density, or the velocity. Practical nozzles do not produce a homogeneous spray. Beside the mean diameter, the knowledge of the shape and deviation to the mean of the size distribution is important. A population distribution can be expressed in terms of number percentage, surface, volume, or mass. That is why several representative diameters can be used to characterize the atomization quality. By convention, the **S**auter **M**ean **D**iameter (**SMD**) defined as the ratio between the surface area mean diameter and the volume mean diameter is used. Parameters like SMD or spray angle have a high influence on fuel conversion and syngas quality in a EF gasifier.

Three mains types of atomizers can be found, pressure atomizers, rotary atomizers and twin-fluid atomizers. The former ones inject the liquid at a high velocity in still air, the latter uses a high velocity gas stream to accelerate the liquid. This last mentioned technology is employed in the bioliq® process. Many studies of twin fluid atomizers have been published, delivering correlations for SMD that facilitate nozzle design and predictions of spray quality. However, most of the studies focus on low viscosity fuels at atmospheric pressure. The current case presents particularities as compared to the aforementioned cases:

- Pyrolysis oil is a highly viscous fluid. In addition, the presence of char accentuates greatly the non-Newtonian behavior [57].
- Entrained-flow gasification operates at very high pressure.

- The atomization medium is also the gasification medium. As gasification operates at low stoichiometry, this poses limitations on the gas flow available for atomization.

Investigations, under the umbrella of HVIGasTech, have been performed to better understand and evaluate these peculiarities. Low viscosity, high viscosity and non-Newtonian fluids have been investigated in a twin-fluid atomizer [58]. As expected, the SMD increases with increasing viscosity. If we compare a non-Newtonian fluid with a zero-viscosity (viscosity in absence of shear stress) equal to that of a Newtonian fluid, the non-Newtonian fluid will produce a finer spray. This arises from the high shear rates at the nozzle exit that lower the viscosity of the non-Newtonian fluid [46]. Other parameters that act on the atomization quality are the gas velocity or the **G**as to **L**iquid **R**atio (**GLR**). All fluids, independent of their rheological properties, show a decrease in SMD with increasing gas velocity [46, 58]. As the gas flow rate is limited, this is an important aspect to consider. Finally, the effect of ambient pressure has been tested [59, 60]. It appears that an increase in reactor pressure, at similar Weber number, increase also the SMD.

All these elements show the difficulty to achieve good atomization of the slurry in an EF gasifier. It requires appropriate atomizer design, which takes into account, the range of operating conditions, such as liquid flow rate, gas velocity, reactor pressure, slurry rheology. With respect to this, upstream tailoring of the slurry can be coupled to atomizer design. For example, we can adjust the temperature of the liquid to reduce its viscosity, we can reduce the slurry viscosity by applying shear stress, we can also vary the solid content of the suspension, and so on.

Once the slurry droplets have been formed, they will undergo a series of thermo-chemical processes to lead to the formation of syngas. We can divide these processes into the liquid conversion and the solid conversion. The phenomena involved can be consecutive or happen concurrently. The liquid conversion is achieved much faster than the solid one; we will thus see the liquid conversion first and then the solid conversion.

Bio-oil conversion

If the main phenomenon involved in the liquid conversion is evaporation, complexity arises from the intricacy of bio-oil. It is a liquid that can comprise hundreds of species, many of them are volatiles but a certain fraction is non-volatile.

The determination of the bio-oil species itself is difficult. Indeed, the **G**as **C**hromatography (**GC**) gives only information about the volatile compounds, letting the high molar weight species undetermined [61]. Derivatization is a technique that can be used to increase species volatility and thus the number of eluents from the gas chromatography column [62]. **H**igh-**P**erformance **L**iquid **C**hromatography (**HPLC**) is another technique to analyze non-volatiles of the bio-oil [63]. Meir et al. [64] estimated the bio-oil composition as follows: 20 $\%_{wt}$ of water, 40 $\%_{wt}$ of GC-detectable species, 15 $\%_{wt}$ of non-volatiles HPLC-detectable species, and around 15 $\%_{wt}$ of non-identifiable species because of a too high molar weight. Even though a pyrolysis liquids sample would be fully analyzed, the results would not necessarily be transposable, as bio-oil composition differs greatly according to the biomass used, the pyrolysis conditions, or the post-treatment. Attempts have been made to describe the pyrolysis products of the basic constituents of biomass, namely cellulose, hemicellulose and lignin [65]. This is a more systematic way to describe the bio-oil composition. Most of the largest species originate from the pyrolysis of lignin. The term pyrolytic lignin is used to describe the water-insoluble fraction of the bio-oil. The pyrolytic lignin contains a very wide molecular weight product distribution because it consists of monomers, dimers and oligomers from phenolic derivatives. While authors suggested that pyrolytic lignin are molecular fragments from lignin [66], other studies suggest that the pyrolyzed lignin only forms monomers that will undergo further re-oligomerization during vapors condensation [67, 68].

Beside the dilemma to adequately describe the largest species of bio-oil, their lack of propensity for evaporation will play a major role in the liquid conversion in an EF gasifier. Part of the oligomers can undergo thermal-cracking, producing shorter-chained lower-boiling hydrocarbons. However, a consequent part of the liquid phase will form char through re-polymerization. This phenomenon has been observed in various application fields of pyrolysis oil, such as pyrolysis oil secondary pyrolysis [69], pyrolysis oil gasification [70], and pyrolysis oil combustion [71]. This coking tendency is an obstacle for the direct combustion of pyrolysis oil, for example in internal combustion engines, with clogging problems, pollution constraints or combustion inefficiency [72–74]. The solid residue is often found in the form of hollow spheres called cenospheres. A SEM picture of cenosphere obtained from the pyrolysis of bio-oil can be seen in Figure 1.4a.

This behavior can be compared to the one of heavy fuel oil or residual oil. Fuel coking is a well-known process and cenospheres were already investigated at the early 1976 [75]. Cenosphere formation has been studied from a chemical and physical point of view. A major component that leads to solid formation is

asphaltene, a macromolecule, highly aromatic, that can agglomerate.

Similarity with the pyrolytic lignin fraction of bio-oil is obvious. Nevertheless, the mechanism of cenosphere formation may show major differences, due to the differences of the liquids themselves. Heavy fuel oil is a much more viscous liquid than bio-oil, while bio-oil contains an important portion of water and oxygenated species. Cenosphere formation from the combustion of bio-oil has first been observed by Wornat [71]. He noted that these cenospheres *bear no resemblance* to the one produced from fuel oil. Later on, numerous studies of bio-oil pyrolysis or combustion have been conducted that help understanding the successive steps. Several studies on bio-oil conversion do not refer to cenosphere formation [70]. On one side, because these solid residues are found only if the conversion is incomplete. The cenospheres, if found, are the unburnt fraction of the fuel. Also, the liquid is subject to microexplosions, a tendency typical of fuel with components of widely varying boiling points [71]. The microexplosion can entirely disrupt the droplet [70, 76, 77], an•d thus no solid shells are found. In other cases [71, 78], microexplosions are observed but result in limited matter ejections. In the latter case, cenospheres or fragment of cenosphere can be found. Particulates found by many groups were of size about equal or larger to the original droplet size, typically with a factor in the range 0.8-2. This indicates that each cenosphere is the result of one droplet polymerization that can undergo swelling or shrinking. Two mechanisms for the microexplosion are discussed in the literature, the viscous shell microexplosion mechanism and the polymer shell mechanism. In both hypotheses, the droplet first undergo heat up and light volatiles evaporate. Evaporation is an interphase phenomenon; the volatile components must diffuse to the surface prior to evaporate. In a multicomponent droplet with highly different boiling points, the mass transfer can rapidly become the rate limiting step. In this viscous shell microexplosion mechanism, the formation of a viscous outer layer is assumed, with the lighter compounds trapped in the core. As the droplet temperature keeps increasing, the core reaches a superheated state and internal bubbling occurs [79]. The second mechanism postulates that the heavy components of bio-oil pyrolyze quickly and form a solid shell [78], which results in an internal pressure increase until the rupture of the shell. Teixeira et al. [76] observed these two phenomena successively. The droplets faced initially strong deformation, without disruption, indicating the high viscoelastic force of the outer layer. Then, in the later stage of the droplet conversion, more rigid shells formed followed by droplet atomization from microexplosion.

The condition under which bio-oil droplets undergo complete disruption or

form cenospheres have not been identified yet. It may depend on the droplet size, the heating rate, the presence of oxidant and of course on the composition of the pyrolysis oil. A series of experiments have been conducted [80] with pyrolysis oil produced within the scope of the bioliq® process. To keep intact the solid formed, i.e. to avoid its oxidation, they performed a secondary pyrolysis of the oil. The term secondary is used to distinguish it from the primary pyrolysis that produced the bio-slurry. The research group at KIT [80] tested with mean of a drop tube reactor two different droplet sizes, 15 and 500 μm. In both cases, cenospheres were found. One of the hollow spheres obtained with the largest droplet size is shown in Figure 1.4a. The cenospheres formed presented a diameter of about the size of the initial liquid droplet and the solid mass accounted for 20% of the injected liquid. Microexplosions were not mentioned by Stoesser et al [80], but some particulates were fractured and other presented blowholes, indicating strong inner pressure acting against a solid outer shell. The research group also performed the case of bio-slurry secondary pyrolysis. Cenospheres were also found whose morphologies are quite different, as shown in Figure 1.4b. The primary char, i.e. the char that compose the bio-slurry, is trapped, or glued, in the second type of char obtained from the liquid conversion. This also suggests a cenosphere formation in two steps. The primary char particles are outwardly pushed by the internal forces and are retained by the viscous outer layer. In a second step, the viscous layer polymerizes and becomes rigid, trapping in the meanwhile the primary char particles.

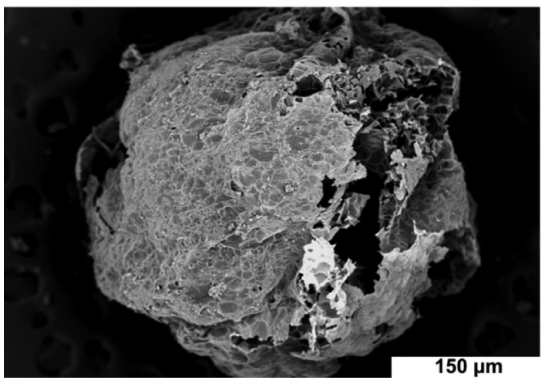

A) Cenosphere formed after pyrolysis of a 500 μm straw oil droplet

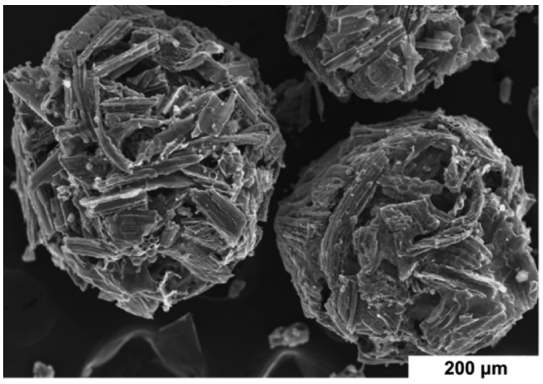

B) Slurry cenospheres with embedded former primary char

FIGURE 1.4: SEM images of cenospheres, taken from [80]

A better understanding of pyrolysis oil conversion mechanism is necessary to fully describe bio-slurry EF gasification. Two distinct scenarios are plausible. In the first one, droplets are unstable and microexplosions prevent the formation

of cenospheres. Depending on the time available for this process, solid formation from thermal cracking and solid burnout could overlap [78] in a similar way as in combustion cases. The primary char would also be isolated from the former droplet and be quicker in contact with the surrounding gas. The second scenarios, as likely, would see droplets leaving the flame zone at the early stages of liquid conversion, with an important quantity of volatiles still in the core of the droplet. Droplets would exit the oxygen rich zone of the reactor and this would favor cenospheres formation. Both cases could result in different reactor performances. In combustion applications, microexplosions are beneficial [76] to increase evaporation and reduce the solid yield. Straightforward conclusions can not be made in gasification applications. That the volatiles are either quickly evaporated or not, has an influence on the flame properties, on the heat release or on the product composition. Also, the solid conversion would follow different mechanisms based on the surrounding gas composition, as it will be addressed in the following hereinafter.

Solid conversion

As seen above, the solid that must be converted in bio-slurry entrained-flow gasification are of two types, the so-called primary char, which is a result of the fast pyrolysis of biomass, and the char formed by oil polymerization. Both account for similar quantities if we consider a slurry in 20/80 char/oil proportion and 20 % of the liquid that polymerizes. In this context, the mechanism of conversion in an EF gasifier for the two types of solids has to be described.

The mechanism of the primary char conversion is extensively documented, in particular because of the similarities with coal [81] and charcoal obtained from the slow pyrolysis of biomass [82] or with other solid fuels [83]. Theories developed for their conversion can be applied in case of char obtained by fast pyrolysis, and we can also reemploy the analytic techniques developed, with for example specific surface area measures, reactivity or proximate composition.

Char combustion or gasification is characterized by a first step of drying and devolatilization. The solid looses mass under the sole effect of the surrounding heat, consequently this step is also referred as pyrolysis in the literature [84]. As the char already originates from the pyrolysis of biomass, we denote this step *secondary pyrolysis* and the product *secondary char*. The fast pyrolysis of biomass is limited to a temperature of 500 °C, well below the gasifier temperature. Therefore the solid is further converted, up to a point where the solid is

close to graphite (almost pure carbon). The study of Stoesser et al. [80] investigated this step solely. In the same drop tube used for the study of bio-oil, they performed the secondary pyrolysis of primary char. Their results show that the solid looses an important quantity of volatile organic matter, of about 40 %. Hydrogen and oxygen content decreased radically in favor of carbon. For example wood char oxygen content decreased from >10 % to <0.1 % while carbon mass fraction increased from 83 % to 98.5 % (measured on ash free basis). A second information is that the ash content before and after secondary varied pyrolysis only slightly, with an increase with wood char and a decrease with straw char. Complexity of the devolatilization step resides in the description of the released products. Many light gases are released, H_2O in the drying phase, then CO, CO_2, H_2, or CH_4. More complex organic or inorganic molecules are also released in gaseous or liquid form, mostly tars. Determination of the gas composition leaving the solid is important because these species will participate in the second step.

The second step is denoted char combustion or char gasification depending on the gaseous reaction partner, O_2 or $H_2O/CO_2/H_2$. This endothermic conversion corresponds to the rate-limiting process of EF gasification and determines the rate of the overall conversion [85]. This char conversion is governed by heterogeneous reactions. In this sense, the oxidizing agent needs to have contact with the solid surface for a reaction to happen. The reaction can therefore be limited by the intrinsic reaction rate, but also by the transport capacity. Three regimes are commonly identified [86, 87], as illustrated in Figure 1.5.

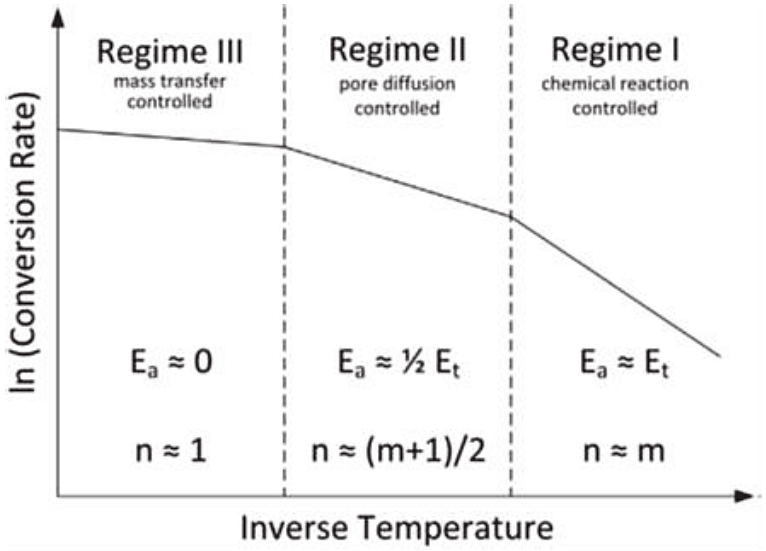

FIGURE 1.5: Reaction rate of a porous carbon in function of versus temperature, taken from [86]

The regime I, or chemical reaction controlled regime, corresponds to low temperature conditions. The intrinsic reaction rate limits the overall reaction rate. As temperature increases, this intrinsic reaction rate also increases exponentially, and the conversion becomes limited by the diffusive transport of the reactant inside the pores of the solid. This corresponds to regime II, or pore diffusion controlled regime. At the highest temperature zone, Regime III, the overall reaction rate is limited by the transport of oxidant agents from the bulk phase to the particles. Because of this conversion mechanism, many char properties play a role in the conversion efficiency. Char composition, particle size, pore structure, morphology, total surface area, number of reactive sites and so on, influence the intrinsic reaction rate and the transport limitations. Besides the char properties, kinetic mechanisms have also been developed [88] for the principal oxidants. In industrial EF gasifiers, the high temperature conditions favor a transport controlled process. The high-pressure conditions, on the other hand, increase the oxidants partial pressure, and thus increase the surface contact of gas phase species. It has been suggested that all three regimes can be found in EF gasification [89] and should be considered. Stoesser et al. [80] also performed measures on primary char and secondary char for wood and straw. They measured an increase of the total surface area of a factor ten for both chars. But unexpectedly, the intrinsic reaction rate decreased slightly. This is attributed to the solid microstructural changes. Besides char surface area and solid structure, the inorganic content contained in the char acts as a catalyst. Potassium, for example, has a strong catalytic effect, but its action is complex and can be inhibited under certain conditions (evaporation, thermal deactivation).

For the second type of solid, the char produced by pyrolysis oil polymerization, less documentation exists because of the singularity of this solid. The most complete information is also provided in [80]. Whilst the solid is the result of a pyrolysis, 21 $\%_m$ of volatiles have been measured. This means that the cenosphere pyrolysis was not complete at the outlet of the laboratory-scale drop tube. Even though the straw oil cenospheres show an ash content as low as 0.1 $\%_m$, the solid is nevertheless prone to gasification with CO_2, as tested by Stoesser et al [80]. The solid shows a reactivity analogous to secondary char up to a conversion of 50 $\%_m$. After this point, the reactivity of the oil cenosphere decreases notably. Finally, bio-slurry reactivity cenosphere has been measured. An intermediate reactivity could be expected. The results show same reactivity up to 50 $\%_m$, then the reactivity sinks even stronger than for oil cenosphere. The underlying mechanism has not been understood yet.

Slag

As mentioned above, inorganic contents of char can be an asset for the conversion efficiency. However, this inorganic part can have adverse effects, such as syngas contamination or wall impairment. Three elements must be considered in order to prevent these issues:

- A maximum amount of ash escape as slag
- Good slag behavior to prevent clogging
- Ensure the reactor walls sustainability

First, it is preferable that a majority of ash forms slag on the reactor wall and drains out in the water bath where they solidify. Slag is a fused material that resembles glass. Ash that escapes with the raw syngas is called fly ash [90]. Fly ash particles can then foul or pollute further equipment [91]. In order to minimize the probability that ash escapes as fly ash, we need to increase collisions with the wall but also the particle sticking probability. This probability depends directly on the particle properties (size/velocity/impact angle/surface tension/temperature/conversion) and on the slag behavior (viscosity/temperature/composition).

Then, we need to ensure a continuous flow of the slag. The liquid flow is directly controlled by its viscosity. An upper threshold of 25 $Pa \cdot s$ has been defined by Highman et al [92]. The slag viscosity has two main dependencies, the temperature and its composition. At high temperature, the slag formation features a Newtonian fluid behavior, and thus the viscosity decreases strongly with an increase of temperature. An Arrhenius type formulation is regularly employed, with an exponential decrease with the temperature. Another approach is the one proposed by Urbain [93]. Lower temperatures induce liquid crystallization or phase separation, increasing dramatically the viscosity. Consequently, an option to improve the slag draining is to produce more heat by injecting more oxidant. However, this may lower the gasification efficiency and increase the operating costs. The slag composition also determines the slag properties. The slag composition depends directly on the chars' one. Measures can be taken to adjust the slag composition, like fuel blending or addition of fluxing agents. Indeed, while the slag logarithm viscosity is usually defined by the weighted sum of the constituents logarithm viscosities, adding other oxides in small quantities to silica results in a sharp decrease of the viscosity called lubricant effect. In addition to the development of models to estimate the viscosity of molten slag, phase

diagrams of binary, ternary or even quaternary systems are developed to predict the systems' physical states. Unusual oxides arise with the use of biomass, such as P_2O_5 or Na_2O [94]. A dedicated slag behavior study for the bioliq® process has been conducted [95], and a self-consistent thermodynamic database permits the establishment of phase diagrams and thermodynamic properties for any composition [96].

Finally, the reactor walls must be designed to handle the slag formation and drain out. First wall technology employed is refractory linings, made of several layers. But these walls are subjects to corrosion, for example due to silica, and are also subject to erosion because of the hot liquid. Aluminium oxide-based walls would not last longer than weeks [92]. Chromium oxide-based or zirconium oxide-based walls are usually employed for the inner hot face, but a replacement or repair is nevertheless necessary every 6 months to 2 years. In particular, biomass' ashes are extremely corrosive due to its high salt content [92]. Another technology used is membrane walls. They are cooled by water on the exterior, and in the interior face, the liquid slag in contact forms a protective layer on which flows the rest of the slag. This layer is self-repairing and thus improves greatly the life-time of the reactor. On the other side, these types of walls are more expensive and also heat loss is higher.

Gas phase

The last aspect to describe EF gasification encompasses all the sub-processes related to the gas phase. They are numerous, complex but also very important. The gas phase is the phase carrier of the process. Rapid calculations indicate that the gas occupies more than 99% of the total volume. Indeed, the gas at 60 bars and 1,600°C has a density of about 10 kg/m^3, and usual gas-to-fuel mass ratio is 0.5 [41]. Also, the liquid phase is quickly vanishing, and the solid mass continuously sinks up to the ash residual mass. Thus, the gas phase volume fraction most likely exceeds 99.9%. Therefore, the gas phase constitutes the core of the process. On one side, there are the numerous sub-processes involving only the gas phase, such as gas phase chemistry, flow field, radiation, diffusion. And on the other hand, the gas phase exchanges with the other phases, namely mass, momentum and energy. Although the underlying mechanisms in the gas phase are particularly complex, they are the most studied and understood. The theory of fluid mechanics has been grounded nearly 2 centuries ago, with the work of Navier and Stokes. The theory developed describes the fundamental physical laws that fluids follow. In a similar way as Newton's second law describes the

mechanic of objects, the Navier-Stokes equations are able to describe fluid flow, mass and heat transfer. The real issue lays in solving these equations. As non-linear partial derivative equations, no analytic solutions can be found, except for cases of reduced complexity. These equations are therefore solved numerically. This forms the foundation of **C**omputational **F**luid **D**ynamics (**CFD**). Chapter 2 will be dedicated to the principles of CFD in combustion applications.

1.3 Modeling the entrained-flow gasification

1.3.1 Experimental data from the laboratory gasifier REGA

A laboratory-scale gasifier named **REGA** (**R**esearch **E**ntrained Flow **GA**sifier) [97] has been built and is operated by KIT at Karlsruhe. This reactor has been especially designed to offer a better understanding and facilitate the mathematical description of the gasification process within the scope of HVIGasTech [45]. The experiments conducted using this reactor are at the core of the present work, both for model development and validation.

As compared to a high-scale EF gasifier, some simplifications are done in the experiment that induces subsequent simplifications in the modeling. The first of these simplifications concerns the fuel used. Instead of using pyrolysis oil, a surrogate is used, namely **E**thylene **G**lycol (**EG**). As it has been shown in Kathrotia et al. [98], EG has similar physical-chemical characteristics to pyrolysis oil from varying feedstocks, such as its viscosity, its density or its enthalpy of combustion. This reduces the complexity of the liquid, normally composed of species from various families and sizes, but also the complexity of the gas phase. A mechanism dedicated to ethylene glycol has been elaborated [98]. This surrogate furnishes well-defined conditions. The reactor is also able to operate with slurries, whose solid particles originate from different biochar. Contrary to high-pressure EF gasifier, REGA operates under atmospheric conditions. Many models and correlations lose their validity as the pressure increases. For example, we will be able to use the perfect gas theory for simulations on REGA, totally inapplicable at 60-80 bars. Slag is not investigated neither in REGA nor in the models used in this thesis.

The gasifier consists of a cylinder with electrically heated walls. The reactor has a length of 3 m and a diameter of 28 cm. With a set point at 1,200 °C, the gas mean residence time is about 3 s. The process flow sheet of this reactor can

be found in the recent publication of Fleck et al. [97]. The fuel and gasification medium (enriched air) are injected through an external mixing twin-fluid atomizer. The reactor is equipped with many in-situ measurement options for the validation of numerical tools. Thermocouples are used to measurement the temperature and gas species profiles are available through probe sampling.

1.3.2 Traditional models and their limitations

Some modeling works have already been done on entrained-flow gasification. Early **RANS** (**R**eynolds-**A**veraged **N**avier-**S**tokes) simulations for the modeling of REGA were performed by Hafner et al. [99]. Too little experimental data were available to validate the CFD models. However, a first detailed chemistry mechanism on EG was successfully developed. Later on, two papers on RANS simulation [100] and **LES** (**L**arge **E**ddy **S**imulation) [101] were published along with the experimental data set given in [97]. These numerical simulations are restricted to ethylene glycol gasification (no solid content). In Mancini et al. [100], two global kinetics mechanisms of 6 reactions were used. It can be seen that the choice of the reactions and their parameters have a major impact on the species and temperature results. Important deviations can be observed, and notably concerning the methane concentrations. The use of a detailed mechanism may appear much more reliable. The work of Eckel et al. [101] allowed having an insight into the injector near-field. The use of Large Eddy Simulation and detailed chemistry captures the details of the injection system and the confined turbulent jet-flow. However, this approach is computationally very expensive, only one simulation was performed (no sensitivity analysis possible for example, even with a reduced geometry (only 70 cm was simulated). Simulating a slurry case with this approach would not be possible with the current computational capacities. More recent simulations on bio-slurries (EG + biochar) were published [102], but the model was unable to capture accurately the presence of solids in the fuel. For 10 % of char particles mixed with ethylene glycol, the results are still coherent because the solid content is still low. However, the test case with 30 % of char showed significant deviations.

The simulations mentioned above, as well as other examples of simulations of entrained-flow gasifiers [103–106], rely on the conventional Lagrangian particle tracking method for the dispersed phase modeling. In this approach, discrete fluid parcels representing fuel droplets or fuel particles are followed in time and provide point sources for the gas field. This multiphasic Euler-Lagrange approach is usually adopted because of the low volume fraction of the dispersed

phase. However, this approach presents limitations when it comes to the modeling of slurry fuels: on the one hand, some assumptions are required. Since the liquid evaporation is faster than the solid conversion, it is usually assumed that each fuel particle is made of a solid core surrounded by liquid. In this way, the liquid evaporation occurs first and when the amount of liquid in the particle is negligible, the solid conversion is taken into account. This is a simplification of the thermophysical phenomena where slurry droplets contain a wide solid particle size distribution that are released continuously during the liquid evaporation. On the other hand, high computational costs arise from the high particle loading and from time-scales differing by several orders of magnitude. Typical chemical time scales of the gas phase fuel oxidation are between 10^{-10} s and 10^{-3} s [107]. The liquid evaporation of one slurry fuel droplet is a fast process, between 10^{-3} s and 10^{-1} s, but the residence time of the solid content in the reactor is high and can exceed 10 s. Concerning the particle loading and taking into account the dataset 15 used in the present work from the laboratory-scale REGA gasifier with a solid mass flow rate of about 1.25 kg/h and a particle mean diameter of 22 μm, the loading exceeds 10^7 particles per second entering the reactor. This number is an under-estimation if we consider smaller particles or the case of an industrial gasifier.

1.4 Scope of this thesis

This thesis is organized as follows: in Chapter 2 we will present computational fluid dynamics fundamentals applied to gas phase combustion. This constitutes the core of the simulations that will be later performed. The conservation equations are presented, with a particular focus on the gas phase chemistry. At this point, a simple test case of a laminar flame is presented to ensure the reliability of the numerical tools that are used. Many approaches are conceivable to model turbulence, combustion turbulence interaction and multiphase flows. These approaches are presented and the choices retained for EF gasification are discussed. Chapter 3 will be dedicated to the derivation of an Euler/Euler approach to model liquid gasification fuels; ethylene glycol as a surrogate for pyrolysis oil in our case. The derivation of the governing equations for two-phase flows is performed. Additional modeling is required to describe the coupling between liquid and gas phase. Main interactions are induced by evaporation,

but momentum exchanges are also investigated. A validation test case is considered for comparison with a traditional Lagrangian approach. Then, the Chapter 4 will address the use of a sectional approach for gasification (size dependent reaction kinetics) to account for solid particles in the fuel to be gasified, thus extending the concept presented in the previous Chapter to include suspension fuels. Finally, Chapter 5 will tackle the modeling accuracy with the help of well documented experiments on the REGA gasifier. Many test cases are considered, first with only ethylene glycol, then with different slurries.

Chapter 2

Computational Fluid Dynamics modeling of combustion

This chapter aims at presenting the basic concepts of Computational Fluid Dynamics (CFD) applied to combustion cases. The numerical models can be transposed to gasification applications. The chapter will introduce regular single phase flows, then chemistry, turbulence, and their interactions will be presented. Then, the basics of the multiphase treatment will be introduced.

2.1 Basic flows

2.1.1 Governing equations

Fluid dynamics rely on conservation principles governed by physical laws. The conservation of mass, momentum, and energy dictates the fluid flow, heat, and mass transfer. The mathematical form of these conservation principles, expressed with **P**artial **D**ifferential **E**quations (**PDE**), is denoted as the **N**avier-**S**tokes (**NS**) equations. They are sufficient to describe the flow behavior of multiple applications, including aerodynamics, industrial equipment, or weather simulations. CFD is the discipline devoted to numerically solve these equations. CFD is restricted to fluids, i.e. to liquid or gas. Also, the fluid must be a continuum, meaning that the flow properties are defined at every point in space in the system. The Navier-Stokes equations are expressed by:

$$\frac{\partial \rho}{\partial t} + \nabla \cdot (\rho \mathbf{v}) = 0, \tag{2.1}$$

$$\frac{\partial \rho \mathbf{v}}{\partial t} + \nabla \cdot (\rho \mathbf{v}\mathbf{v}) = \nabla \cdot \overline{\overline{\sigma}} + \mathbf{f}_V, \tag{2.2}$$

$$\frac{\partial}{\partial t}\left(\rho E\right) + \nabla \cdot \left(\rho E \mathbf{v}\right) = -\nabla \cdot \dot{\mathbf{q}} + \nabla \cdot \left(\overline{\overline{\sigma}} \cdot \mathbf{v}\right) + \mathbf{f}_V \mathbf{v} + \dot{q}_V. \tag{2.3}$$

More generally, the conservation equation for a transported intensive property Φ is written:

$$\frac{\partial}{\partial t}\left(\rho\Phi\right) + \nabla \cdot \left(\rho\Phi \mathbf{v}\right) = \nabla \cdot \left(\Gamma^{\Phi} \nabla \Phi\right) + \dot{Q}^{\Phi}. \tag{2.4}$$

Intensive means that properties are expressed on a per unit mass basis. The conserved variable is the associated extensive property $\rho\Phi$. To derive the previous equation, we first define an arbitrary **C**ontrol **V**olume **CV** denoted $\mathscr{V}$. Over the infinitesimal time dt, the variation of the integrated property $\rho\Phi$ is equal to the flux of Φ through the control volume surface $\mathscr{S}$ plus the source or sink within the CV. Expressed mathematically, the three terms of the aforementioned balance become:

$$\frac{d}{dt}\left(\int_{\mathscr{V}} \rho\Phi d\mathscr{V}\right) = -\int_{\mathscr{S}} \mathbf{j} \cdot d\boldsymbol{\mathscr{S}} + \int_{\mathscr{V}} \dot{Q}^{\Phi} d\mathscr{V}. \tag{2.5}$$

$d\boldsymbol{\mathscr{S}}$ is any differential area, which is normal outward-pointing to the surface $\mathscr{S}$. The Reynolds transport theorem can be applied to the term on the left, and as the CV is constant with respect to time, it results in the integral over $\mathscr{V}$ of the partial time derivative of the conserved quantity. The flux $\mathbf{j}$ through the boundary has two contributions, the convective flux moved by the bulk motion of the flow and the diffusive flux that arises from diffusion, which is driven by a gradient of the property of interest Φ. The former equation becomes:

$$\int_{\mathscr{V}} \frac{\partial}{\partial t}\left(\rho\Phi\right) d\mathscr{V} = -\int_{\mathscr{S}} \rho\Phi \mathbf{v} \cdot d\boldsymbol{\mathscr{S}} - \int_{\mathscr{S}} -\Gamma^{\Phi} \nabla\Phi \cdot d\boldsymbol{\mathscr{S}} + \int_{\mathscr{V}} \dot{Q}^{\Phi} d\mathscr{V}. \tag{2.6}$$

Applying Gauß theorem on the two surface terms and moving all terms to the left leads to

$$\int_{\mathscr{V}} \left(\frac{\partial}{\partial t}\left(\rho\Phi\right) + \nabla \cdot \left(\rho\Phi \mathbf{v}\right) - \nabla \cdot \left(\Gamma^{\Phi} \nabla\Phi\right) - \dot{Q}^{\Phi}\right) = 0. \tag{2.7}$$

The above formulation is defined for any arbitrary control volume, and thus this integrand has to be zero, leading to equation 2.4.

For combustion applications, the Navier-Stokes equations are extended. Combustion necessarily involves many chemical species. Therefore, species conservation equations are added to the NS set of equations, and new terms appear

in the momentum and energy equations. The set of equations usually used in combustion CFD modeling is concisely reported in Table 2.1 following the form of the generic equation 2.4. Having consistency in the formulation will facilitate the numerical task, because terms with the same operator will be treated similarly (time derivative, gradient, divergence...). The table 2.1 is reviewed by column from left to right.

- Temporal changes. As for NS equations, we solve for mass and momentum. Instead of the total energy E, the energy equation is expressed in term of internal energy e. They are linked with the kinetic energy by $E = e + \frac{1}{2}v^2$. Other equations can be used, such as sensible energies (energy-chemical energy $e - e_c$, $E - E_c$), enthalpy, sensible enthalpy or even the temperature. The different forms can be found in [108]. The internal energy equation is here displayed, as commonly used variable. The exact treatment of the energy equation and the temperature solution will be further detailed in part 2.2. The last quantities whose temporal change is followed are the species mass fractions. We denote by N_i the total number of chemical species, we will solve $N_i - 1$ species transport equations, the last mass fraction being calculated from the closure condition $Y_{N_i} = 1 - \sum_{N_i-1} Y_i$.

- Convective fluxes. Every quantity of interest has a convection term of similar form, $\nabla \cdot \left(\rho \Phi \mathbf{v}\right)$.

- Diffusive fluxes. Diffusive fluxes only appear in the energy and species mass fraction equations. Heat conduction follows Fourier's law, which states that the heat transfer is proportional to the negative gradient of temperature $\mathbf{q} = -\lambda \nabla T$. The species diffusive flux has several contributions, $\mathbf{j}_i = \mathbf{j}_i^c + \mathbf{j}_i^T + \mathbf{j}_i^p$. These three terms arise from different parameter gradients: gradient of concentration, temperature, and pressure. In an analogous way to Fourier's law, the Fick's law states that species moves from high to low concentration regions. The diffusion molar flux for binary mixtures is given by $\mathbf{j}_1^{*,c} = -cD_{12}\nabla X_1$. D_{12} is the binary coefficient that depends on the nature of species 1 and 2 and operating parameters like pressure and temperature. It can be expressed in term of mass fraction with little modification $\mathbf{j}_1^c = -\rho D_{12}\nabla Y_1$. For multicomponent mixtures, a diffusion coefficient D_{ik} is defined for each species pair, and the Fick's law becomes $\mathbf{j}_i^c = -\rho \frac{M_i}{M} \sum_{k=1}^{N_i} D_{ik} \left(\nabla Y_k + Y_k \frac{\nabla M}{M}\right)$, where M is the average molar weight. This form is barely used because the diffusive flux of species i is depending on all species gradients. The simplified form $\mathbf{j}_i^c = -\rho D_{im} \nabla Y_i$

is used, where D_{im} is the diffusivity of species i with respect to the remaining gas mixture. The pressure diffusion is usually neglected in combustion applications. Thermal diffusion, also called Soret effect or thermophoresis for aerosol mixtures, is written $\mathbf{j}_i^T = -D_i^T \frac{\nabla T}{T}$. In the energy equation, a diffusive heat flux arises from the latter species mass diffusion. As each species transports different enthalpies, species diffusion implies an energy flux given by $\mathbf{j}_q = \sum_{i=1}^{N_i} h_i \mathbf{j}_i$.

- Surface sources. Two terms for the surface sources appear in the momentum equation. They are obtained from the total stress tensor, $\overline{\overline{\sigma}}$, that is split into two components, such that $\overline{\overline{\sigma}} = -p\overline{\overline{\mathbf{I}}} + \overline{\overline{\tau}}$. We can identify the pressure p and the deviatoric or viscous stress tensor $\overline{\overline{\tau}}$. This separation allows isolating the pressure, which acts normal to the surface, and the viscous term. We study the cases of gas flows, which are by nature Newtonian fluids. In this case, the stress tensor is a linear function of the strain rate, $\overline{\overline{\tau}} = \mu \left[\nabla \mathbf{v} + (\nabla \mathbf{v})^{\mathsf{T}}\right] - \frac{2}{3}\mu (\nabla \cdot \mathbf{v}) \overline{\overline{\mathbf{I}}}$ (note: in the second term, the bulk viscosity has already been replaced by the molecular viscosity μ). Now, for the energy equation, the two terms that appear result from the surface forces of the momentum equation. The product of surface forces and displacement per unit time gives the net rate of work addition/extraction through its boundary. This leads for our two forces, after application of Gauß theorem, to $\nabla \cdot \left(-p\mathbf{v} + \overline{\overline{\tau}} \cdot \mathbf{v}\right)$. The final form of these two terms, as displayed in Table 2.1, is obtained from the derivation of the internal energy from the total energy; the temporal change of the kinetic energy appears, which can be substituted by $\mathbf{v}$ times the momentum equation.

- Volume sources. The only body force that is retained for the momentum equation is gravitation (no Coriolis or magnetic forces). Gravitation is not a negligible force in combustion applications: the temperature gradient from the flame front to the far field builds a gas density difference that causes the buoyancy effect. In zero-gravity environment, flame shapes are significantly different. For the energy equation, the volume sources have many contributions. The first is the work due to the gravitation force. The development is similar to the one seen for the surface sources, except that no Gauß theorem is necessary. The second source term is radiation. It is often be negligible in combustion applications, not in our gasification case. The reason for this is that thermal radiation grows with the fourth power of temperature. Because of the conditions in an EF gasifier, the radiation heat transfer can overcome the convective one. The last term of Table 2.1

is the chemical source term. It will determine for each species its total rate of consumption or creation. The chemical source term, $\dot{\omega}_i$, is expressed as mass per volume of species i created by second. Over dt, the mass of species i is determined by the summation over the single reactions that consumes or produces the species. In other words, $\dot{\omega}_i = M_i \sum_{r=i}^{N_r} \nu_{ir} S_r$. ν_{ir} is the stoichiometric coefficient of species i in the reaction r, that is positive when species i is produced, negative otherwise. S_r is the rate of reaction r expressed in $\mathrm{mol/m^3/s}$. It should be noted that in the present energy equation, the heat release rate does not explicitly appear. This is because this form of energy already includes chemical terms, $e = e_s + \sum_i^{N_i} Y_i h_{\mathrm{f},i}^{\circ}$, where $h_{\mathrm{f},i}^{\circ}$ is the enthalpy of formation of species i. When deriving the sensible energy conservation equation, the heat release rate, i.e. the heat associated to chemical reactions, appears and is given by $\dot{Q}_c = -\sum_i^{N_i} h_{\mathrm{f},i}^{\circ} \dot{\omega}_i$.

TABLE 2.1: Fluid dynamics conservation equations and description of their terms

Temporal changes	+ Convective fluxes	= Diffusive fluxes	+ Surface sources	+ Volume sources
• Mass $\frac{\partial \rho}{\partial t}$	• Convection $\nabla \cdot (\rho \mathbf{v})$	-	-	-
• Momentum $\frac{\partial \rho \mathbf{v}}{\partial t}$	• Convection $\nabla \cdot (\rho \mathbf{v}\mathbf{v})$	-	• Pressure gradient $-\nabla p$ • Viscous stress $\nabla \cdot \overline{\overline{\boldsymbol{\tau}}}$	• Gravitation $\rho \mathbf{g}$
• Internal energy $\frac{\partial \rho e}{\partial t}$	• Convection $\nabla \cdot (\rho e \mathbf{v})$	• Species diffusion $-\nabla \cdot \mathbf{j}_q$ • Heat conduction $-\nabla \cdot \mathbf{q}$	• Pressure work $-p \nabla \cdot \mathbf{v}$ • Dissipation $\overline{\overline{\boldsymbol{\tau}}} : \nabla \mathbf{v}$	• Gravitation $\rho \mathbf{g} \cdot \mathbf{v}$ • Radiation $\dot{q}_r$
• Mass of species i $\frac{\partial \rho Y_i}{\partial t}$	• Convection $\nabla \cdot (\rho Y_i \mathbf{v})$	• Species diffusion $-\nabla \cdot \mathbf{j}_i$	-	• Chemical reactions $\dot{\omega}_i$

2.1.2 Finite volume method

The previous part was dedicated to the transcription of the physical phenomena. This physical modeling is valid on a certain physical domain, typically the reactor internal domain. We have, therefore, a set of governing equations defined on a computational domain. The next step is the domain discretization and the equations discretization. As a result, we will obtain a set of algebraic

equations that we can solve numerically. This part will be dedicated to present the discretization process and numerical methods.

Many different discretization methods have been developed. The present work uses OpenFOAM, an open source simulation tool based on **F**inite **V**olume **M**ethods (**FVM**). Therefore, only this method will be presented. The first discretization task consists in the domain discretization. As its name suggests, FVM is based on discretizing the domain in a finite number of volumes. The volumes, denoted as cells, must not overlap each other but are bounded face to face. Together, the cells compose the physical domain directly. This ability to truly reproduce complex geometries makes FVM the most popular method nowadays. The cells can be of arbitrary polyhedral shapes. They are defined by a list of vertices and faces. Except at the boundaries, two neighboring cells share a common face. We usually make a distinction between structured and unstructured mesh. The first one has a regular connectivity and is the most effective to retrieve neighborhood relationships since it can be deduced from the cell indices. On the contrary, unstructured meshes are not regular but allow a better adaptation to complex geometries. More details about the mesh must be stored to fully describe the mesh.

The governing equations, as given in the previous section, can be integrated over the finite volumes. We denote a cell C_A of volume $\mathscr{V}_A$, of surface $\mathscr{S}_A$. The general conservation equation for cell C_A becomes:

$$\int_{\mathscr{V}_A} \frac{\partial \rho\Phi}{\partial t} d\mathscr{V} + \int_{\mathscr{V}_A} \nabla \cdot \left(\rho\Phi\mathbf{v}\right) d\mathscr{V} = \int_{\mathscr{V}_A} \nabla \cdot \left(\Gamma^{\Phi}\nabla\Phi\right) d\mathscr{V} + \int_{\mathscr{V}_A} \dot{Q}^{\Phi} d\mathscr{V}. \quad (2.8)$$

Or, after application of the Gauß theorem:

$$\int_{\mathscr{V}_A} \frac{\partial \rho\Phi}{\partial t} d\mathscr{V} + \oint_{\mathscr{S}_A} \left(\rho\Phi\mathbf{v}\right) \cdot d\boldsymbol{\mathscr{S}} = \oint_{\mathscr{S}_A} \left(\Gamma^{\Phi}\nabla\Phi\right) \cdot d\boldsymbol{\mathscr{S}} + \int_{\mathscr{V}_A} \dot{Q}^{\Phi} d\mathscr{V}. \quad (2.9)$$

The temporal derivative can further be rearranged into

$$\frac{\partial}{\partial t} \int_{\mathscr{V}_A} \rho\Phi d\mathscr{V}. \quad (2.10)$$

OpenFOAM is using a collocated grid, which means, all variables are computed and stored at the centroid of the cells. The centroid of the cell C_A, is the point A that respect $\int_{\mathscr{V}_A} \left(\mathbf{x}_A - \mathbf{x}\right) d\mathscr{V} = 0$. The time derivative can be rewritten:

$$\frac{\partial}{\partial t} \int_{\mathscr{V}_A} \rho\Phi d\mathscr{V} = \frac{\partial \left(\rho\Phi\right)_A}{\partial t} \mathscr{V}_A. \quad (2.11)$$

This approximation is second order accurate. It is also possible to use more than one integration points, for example 4 or 9, following the Gaussian quadrature. But this is mostly restricted to the finite element methods rather than FVM. The time derivative must also be integrated, but this will be performed after the spatial discretization. Similarly, the source term yields:

$$\int_{\mathscr{V}_A} \dot{Q}^{\Phi} d\mathscr{V} = \dot{Q}^{\Phi}_A \mathscr{V}_A. \tag{2.12}$$

The surface of the cell C_A is composed of a finite number of faces, denoted f, such that the surface of all faces $\bigcup_f S_f = \mathscr{S}_A$. Therefore, the surface integrals can be exactly rewritten in terms of the sum of the individual faces integrals. Again, a simple mean value integration (one integration point) at the faces centroids, F, can be used to evaluate the faces integrals. These two steps for the convective and diffusive fluxes are given below:

$$\oint_{\mathscr{S}_A} (\rho\Phi\mathbf{v}) \cdot d\boldsymbol{\mathscr{S}}_A = \sum_f \left[\int_{S_f} (\rho\Phi\mathbf{v}) \cdot d\mathbf{S}_f \right] \simeq \sum_f (\rho\Phi\mathbf{v})_F \cdot \mathbf{S}_f, \tag{2.13}$$

$$\oint_{\mathscr{S}_A} \left(\Gamma^{\Phi}\nabla\Phi\right) \cdot d\boldsymbol{\mathscr{S}}_A = \sum_f \left[\int_{S_f} \left(\Gamma^{\Phi}\nabla\Phi\right) \cdot d\mathbf{S}_f \right] \simeq \sum_f \left(\Gamma^{\Phi}\nabla\Phi\right)_F \cdot \mathbf{S}_f. \tag{2.14}$$

We have knowledge of the geometrical parameters of cell C_A and its adjoining cells, as well as the variables at the cells' centroids. Yet we need to evaluate the previous terms at the faces centers. It is then necessary to employ interpolation schemes. By taking an arbitrary face between the cell C_A and a neighboring cell C_B, a possibility is to linearly interpolate the variable. Thus, denoting F_{AB} the face centroid, and ψ the ratio of the distances, $\psi = \frac{\left\|\mathbf{x}_{F_{AB}} - \mathbf{x}_A\right\|}{\|\mathbf{x}_B - \mathbf{x}_A\|}$, then the variable Φ at the cell centroid is interpolated by:

$$\Phi_{F_{AB}} = \psi\Phi_A + (1-\psi)\Phi_B. \tag{2.15}$$

This scheme, also called central differencing, is second order in space accurate, but is unbounded. Another widely used, but simple, is upwinding. As the convection term is directed by the velocity field, we can take $\Phi_{F_{AB}} = \Phi_A$ if $\mathbf{v} \cdot \mathbf{AB} > 0$, Φ_B otherwise. This scheme is only first order accurate, very diffusive, but converges easily and does not produce oscillations. Higher order upwind schemes have been developed. For example, the second upwind scheme, also called linear upwind scheme, is using the variable of a third node upwind the

flow direction. Again, if we take the flow in the direction of A to B, the variable can be extrapolated with the neighbor cell of C_A opposite to C_B, written C_C:

$$\Phi_{F_{AB}} = \Phi_A + \frac{1}{2}(\Phi_A - \Phi_C) = \frac{3}{2}\Phi_A - \frac{1}{2}\Phi_C. \tag{2.16}$$

This scheme can also generate oscillating solution, a limiter function can be set to switch the scheme to first order upwind in cases of a strong gradient, and avoid dispersive errors. Many other higher order schemes have been or are developed, for example superbee, minmod or vanleer schemes.

The drawback of the rather straightforward aforementioned schemes is the assumption of rectilinear cell arrangement. The grid can be skew, which means that the line AB does not cross the face at its center. It has no impact on the first order upwind scheme, because it refers to a single point. But the second order upwind and the central differencing schemes must be expressed with gradients of Φ, which give respectively:

$$\Phi_{F_{AB}} = \Phi_A + \left(\mathbf{x}_{F_{AB}} - \mathbf{x}_A\right) \cdot \nabla\Phi_{F_{AB}} \tag{2.17}$$

and

$$\Phi_{F_{AB}} = \Phi_A + \left(\mathbf{x}_{F_{AB}} - \mathbf{x}_A\right) \cdot \left(2\nabla\Phi_A - \nabla\Phi_{F_{AB}}\right). \tag{2.18}$$

The gradient of Φ at the centroid can be calculated through:

$$\nabla\Phi_A = \frac{1}{\mathscr{V}_A}\sum_f \Phi_F \mathbf{S}_f. \tag{2.19}$$

The grid can be non-orthogonal, i.e. the outward directed vector $\mathbf{S}_{AB}$ and the vector straddling the face, $\mathbf{x}_B - \mathbf{x}_A$, are not collinear. It has an incidence on the diffusive term discretization. The dot product $\nabla\Phi_{S_{AB}} \cdot \mathbf{S}_{AB}$ cannot be directly expressed in term of Φ_A and Φ_B as it has a component perpendicular to AB. We usually decompose the gradient of Φ in an orthogonal and a non-orthogonal contribution.

The development of the spatial discretization led above gives a quick overview of the methods that have been developed. The accuracy of the simulation results not only depends on the scheme chosen, but before all on the mesh attributes, and the adaptation of the scheme with the nature of the physical problem. There are currently 55 numerical schemes for space discretization developed in OpenFOAM.

When the set of equation has been spatially discretized, it is possible to perform the time integration to account for the transient phenomena. The method employed is generally a time stepping procedure. We start with an initial time where the fields are known, and we solve the new fields one time step after another. It requires to store only one or two time steps, depending on the scheme, to solve a new one. Taking a constant time step Δt, the fields are initialized at $t^0 = 0$ s, and solved at $t^{n+1} = (n+1)\Delta t$ (n=positive integer) with help of the field at t^n, t^{n-1}, etc... Two tasks must be performed: first, the time derivative term must be discretized, secondly, the other terms must be expressed at a chosen time. If we reemploy the general conservation equation, and we perform a simple forward Euler time discretization, we have:

$$\frac{\rho^{n+1}\Phi^{n+1} - \rho^n\Phi^n}{\Delta t} + \Big[\nabla \cdot \big(\rho\Phi\mathbf{v}\big)\Big]^* = \Big[\nabla \cdot \Big(\Gamma^\Phi \nabla\Phi\Big)\Big]^* + \dot{Q}^{\Phi^*,*}. \tag{2.20}$$

With $* = n$, we obtain an explicit scheme. The variable of interest at the new time step Φ^{n+1} can be expressed with only known values. This method is however barely used in numerical calculation because it is conditionally stable, which means that it implies very small time steps. A fully explicit scheme is not implemented in OpenFOAM. Now, if $* = n+1$, we obtain the form called Euler implicit, which is the default one of OpenFOAM. Solving the equation requires more computational effort, since it is not possible to solve each cell value separately. On the contrary the whole set of variables is solved simultaneously, because each equation contains more than one unknown. To solve for the field Φ^{n+1}, we use a matrix formulation of the set of equations:

$$\overline{\overline{\mathbf{A}}}\boldsymbol{\Phi}^{n+1} = \mathbf{b}, \tag{2.21}$$

where $\boldsymbol{\Phi}$ denotes the variable Φ at every grid point. Then, with numerical methods, the variable field can be solved. However, in practice, the resolution of the variable (mass, momentum, energy, species mass fraction) will not be so straightforward. A first issue is that in the discretizations shown above, the field $\mathbf{v}$ was supposed to be known, while it has to be solved in the set of equations. The second problem is the strong coupling between pressure and velocity.

We consider, in a first time, only the mass and momentum conservation equations. The velocity field can be computed from the momentum equations, but the pressure field cannot be calculated from the continuity equation, an algorithm is necessary to solve correctly the fields. The basic idea is to reformulate the Navier-Stokes equations in a momentum and a pressure equation. By means

of simplicity, we can consider firstly that the flow is incompressible and that we have a steady density. Then the continuity equation becomes $\nabla \cdot \mathbf{v} = 0$.

The momentum equation

$$\frac{\partial \rho \mathbf{v}}{\partial t} + \nabla \cdot (\rho \mathbf{v}\mathbf{v}) = -\nabla p + \nabla \cdot \overline{\overline{\boldsymbol{\tau}}} + \rho \mathbf{g} \tag{2.22}$$

becomes after spatial discretization

$$\begin{aligned} V_A \frac{\partial \rho_A \mathbf{v}_A}{\partial t} + \sum_f (\rho \mathbf{v}\mathbf{v})_F \cdot d\mathbf{S}_f = -V_A (\nabla p)_A + \sum_f \mu \nabla \mathbf{v}_F \cdot \mathbf{S}_f \\ + \sum_f \mu (\nabla \mathbf{v})_F^{\mathsf{T}} \cdot \mathbf{S}_f + \rho_A V_A \mathbf{g}. \end{aligned} \tag{2.23}$$

The diagonal term of the shear stress vanishes under incompressibility conditions because the divergence of the velocity field is null. The terms expressed at the faces can be written at the point A and at the centroids of the neighboring cells to C_A, B_n, with schemes that have been presented above. Then, by performing Euler scheme time integration, and denoting $\star$ the updated field, n the old fields, we can rearrange with simplified notations as follows:

$$a_A^\star \mathbf{v}_A^\star + \sum_{B_n} a_{B_n}^\star \mathbf{v}_{B_n}^\star = -(\nabla p)_A^n + \mathbf{b}_A^n. \tag{2.24}$$

When put in a matrix formulation, $a_A^\star$ correspond to the diagonal terms, and $a_{B_n}^\star$ the off-diagonal terms. $\mathbf{b}_A^n$ regroups the right-hand side explicit source terms excluding the pressure gradient. This equation can be solved. We obtained an updated value of the velocity $\mathbf{v}^\star$ calculated with the old value of the pressure. This is the predictor step.

Then follows the corrector step. We can similarly derive the momentum equation at a corrected step $\star\star$ using the predicted and the old values:

$$a_A^{\star\star} \mathbf{v}_A^{\star\star} + \sum_{B_n} a_{B_n}^\star \mathbf{v}_{B_n}^\star = -(\nabla p)_A^\star + \mathbf{b}_A^n. \tag{2.25}$$

There are two unknowns is the last equations, the corrected velocity $a_A^{\star\star}$ and $(\nabla p)_A^\star$. We will derive a pressure equation to solve for the corrected pressure. We reduce the notation with $\mathbf{H} = \mathbf{b}_A^n - \sum_{B_n} a_{B_n}^\star \mathbf{v}_{B_n}^\star$, which leads to the simplified

form of the previous equation:

$$\mathbf{v}_A^{\star\star} = \frac{\mathbf{H}}{a_A^{\star\star}} - \frac{(\nabla p)_A^{\star}}{a_A^{\star\star}}. \tag{2.26}$$

Then, we use the fact that the corrected velocity must respect the continuity equation $\nabla \cdot \mathbf{v}^{\star\star} = 0$, in order to obtain the pressure equation (or Poisson equation):

$$\nabla \cdot \left[\frac{1}{a_A^{\star\star}} (\nabla p)_A^{\star} \right] = \nabla \cdot \left(\frac{\mathbf{H}}{a_A^{\star\star}} \right). \tag{2.27}$$

We can calculate the corrected pressure from this last equation and then solve the corrected velocity with equation 2.26.

Algorithms have been developed that consecutively solve velocity and pressure fields until a solution that satisfy both momentum and continuity equations is obtained. The most famous algorithm, called **SIMPLE** (**S**emi **I**mplicit **M**ethod for **P**ressure **L**inked **E**quations) was developed by Patankar and Spalding. The most used algorithm in OpenFOAM is called PIMPLE. It is based on the **PISO** algorithm, for **P**ressure **I**mplicit with **S**plitting **O**perators, that is itself a variant of the SIMPLE algorithm. The PIMPLE algorithm applied to our case will be presented in the following. First notable difference, the incompressibility condition will not be assumed. OpenFOAM solvers for reacting flows are basically conceived to handle compressibility to be as generic as possible. As a consequence, the set of equations is embedded by an equation of state making a link between density and pressure. Here, the ideal gas equation is used:

$$\rho = \frac{pM}{RT}. \tag{2.28}$$

Also, the bulk viscosity term of the momentum equation should be considered. A generic reactive solver including a PIMPLE algorithm to solve for velocity and pressure can be seen in Algorithm 1. OpenFOAM solvers are segregated, which mean that fields are solved one after the others. Apprehending the algorithm is necessary to understand in which order the variables are estimated, updated or corrected, and help performing further modifications of the solver. Two parameters can be set, nOuterCorr and nCorr. By setting nOuterCorr to 1 and nCorr to 0, we operate in SIMPLE mode. If both are equal to 1 we are in PISO mode. Starting from the statement that the overall convergence depends mainly on finding the correct pressure solution, PISO complete SIMPLE by solving a second pressure correction equation. PIMPLE mode is active when nOuterCorr

is larger than 1. It allows the use of very large time steps, but the number of PISO loops must be also very large. Time steps must generally meet strict conditions given by the **C**ourant–**F**riedrichs–**L**ewy (**CFL**), $CFL = \frac{u\Delta t}{\Delta x}$. It follows that solving explicitly a linear partial differential equation requires a CFL smaller than one. With implicit schemes, even if they are unconditionally stable, in practice, conditions on the time step are also needed. First, because non-linear PDE are not unconditionally stable and also for accuracy concerns, the error of the Euler scheme decreasing for example linearly with Δt. The PISO method is usually used with a maximum CFL of 0.5. For the PIMPLE algorithm, the CFL number can exceed this number in term of convergence, but for accuracy, a CFL number not larger than 10 is recommended.

Initial set of values $\{\rho; \mathbf{v}; Y_i; h_s; p\}^n$
while $t < t_{end}$ **do**
  Enter PIMPLE outer loop
  for *nOuterCorr* **do**
    while *convergence criteria not satisfied* **do**
      if *first PIMPLE loop* **then**
        Solve continuity equation as in Eqn. 2.1 $\{\rho^\star; \mathbf{v}^n; Y_i^n; h_s^n; p^n\}$
      end
      Solve for predicted velocity as in Eqn. 2.24 $\{\rho^\star; \mathbf{v}^\star; Y_i^n; h_s^n; p^n\}$
      Solve species equations as in Table 2.1 $\{\rho^\star; \mathbf{v}^\star; Y_i^\star; h_s^n; p^n\}$
      Solve energy equation as in Table 2.1 $\{\rho^\star; \mathbf{v}^\star; Y_i^\star; h_s{}^\star; p^n\}$
      Update density with Eqn. of state $\{\rho^{\star\star}; \mathbf{v}^\star; Y_i^\star; h_s^\star; p^n\}$
      Solve first pressure equation as in Eqn. 2.27 $\{\rho^{\star\star}; \mathbf{v}^\star; Y_i^\star; h_s^\star; p^\star\}$
      Correct velocity as in Eqn. 2.26 $\{\rho^{\star\star}; \mathbf{v}^{\star\star}; Y_i^\star; h_s^\star; p^\star\}$
      Enter PISO loop
      for *nCorr* **do**
        Update density with Eqn. of state $\{\rho^{\star\star}; \mathbf{v}^{\star\star}; Y_i^\star; h_s^\star; p^\star\}$
        Solve second pressure equation $\{\rho^{\star\star}; \mathbf{v}^{\star\star}; Y_i^\star; h_s^\star; p^{\star\star}\}$
        Correct velocity $\{\rho^{\star\star}; \mathbf{v}^{\star\star\star}; Y_i^\star; h_s^\star; p^{\star\star}\}$
        Set $\{\rho^{\star\star}; \mathbf{v}^{\star\star} = \mathbf{v}^{\star\star\star}; Y_i^\star; h_s^\star; p^\star = p^{\star\star}\}$
      end
      Set $\{\rho^n = \rho^{\star\star}; \mathbf{v}^n = \mathbf{v}^{\star\star\star}; Y_i^n = Y_i^\star; h_s^n = h_s^\star; p^n = p^{\star\star}\}$
    end
    Set $\left\{\rho^{n+1} = \rho^n; \mathbf{v}^{n+1} = \mathbf{v}^n; Y_i^{n+1} = Y_i^n; h_s^{n+1} = h_s^n; p^{n+1} = p^n\right\}$
  end
end
Stop

Algorithmus 1 : Reacting solver of a compressible flow with PIMPLE loop

The species and energy equations are solved in the PIMPLE outer loop, therefore only once in PISO mode with the predicted fields. The temperature field is calculated just after the energy equation is solved. If, for example, we solve the sensible enthalpy, then we can use the relation:

$$h_s = \int_{T^\circ}^{T} c_p dT, \tag{2.29}$$

where c_p is the heat capacity of the mixture, calculated by averaging the species heat capacity with their respective mass fractions. The heat capacity of species i is usually given with so-called NASA polynomials. The relation of the gas mixture sensible enthalpy can be expressed solely in function of the temperature:

$$h_s = \int_{T^\circ}^{T} \left[\sum_{i}^{N_i} \left(Y_i \sum_{j=1}^{5} a_{i,j} T^j \right) \right] dT. \tag{2.30}$$

Then by performing an iterative method, for example the Newton-Raphson's method, we can solve for the temperature.

2.2 Simple combustion applications

In entrained-flow gasification, the gas phase is a system akin to a gaseous combustion case. Fuel and oxidant undergo a sequence of elementary exothermic reactions forming a flame. With the previously presented set of equations, it is possible to solve simple combustion cases. For example gas phase laminar flames. In the following, the example of the calculation of a hydrogen flame is presented.

2.2.1 Test case presentation and setup

The experimental data for the present case are taken from [109]. The chosen case investigates laminar, axisymmetric hydrogen–air diffusion flames. An inner pipe where the fuel is injected is surrounded by an outer cylinder with air. Further operating conditions are summarized in Table 2.2. For the simulation, the solver rhoReactingBuoyantFoam of OpenFOAM-5.0 has been used as such, except for small modifications that will be detailed later. This solver follows the algorithm presented in the previous part. As the simulation can be achieved quickly, we prioritize accuracy over convergence. The simulation has

been run in PISO mode, with following parameters: $nOuterCorr = 1$, $nCorr = 3$, $CFL = 0.4$. We will solve for the mass conservation, the momentum conservation, the sensible enthalpy and the species mass fraction.

TABLE 2.2: Operating conditions of laminar flame from [109]

	Fuel inlet	Air inlet
Composition	50/50 $\%_V$ H_2/N_2	21/79 $\%_V$ O_2/N_2
Diameter	9 mm	90 mm
Velocity	50 cm/s	50 cm/s
Temperature	20 °C	20 °C

The present case shows an axis of symmetry, we can reduce the simulation to a 2D case by creating a wedge mesh composed of one layer of cell. A 2D-structured mesh representing 5° of the real geometry amounting for 61,200 cells (180*340) has been used. All the cells are hexahedrons, except for the cells along the axis, which are triangular prisms. All the cells are orthogonal between them. The cross section of the mesh can be seen in Figure 2.1a. In this figure, the initial temperature field is also shown. The temperature is set at the ambient temperature, except at the fuel inlet where a temperature of 2,000 K has been set in order to ignite the fuel.

2.2.2 Finite Rate chemistry

Methods have been detailed in the previous section to solve for the continuity and momentum conservation. As a multicomponent reacting case, a central point is to solve for the individual species transport and reactivity. The global reaction governing the flame can be written:

$$H_2 + \frac{1}{2} O_2 \longrightarrow H_2O. \tag{2.31}$$

An Arrhenius-like constant reaction rate is used:

$$k_r = A_r T^b \exp\left(-\frac{E_a}{RT}\right), \tag{2.32}$$

with, according to Marinov et al. [110], $A_r = 1.8 \cdot 10^{-13}$ mol/cm^3/s, $b = 0$, $E_a = 17,614$ J/mol, and the partial orders with respect to the reactants follows

their stoichiometric coefficient. Then the reaction rate can be written:

$$S_r = k_r \left[\mathrm{H_2}\right] \left[\mathrm{O_2}\right]^{1/2}. \tag{2.33}$$

The species transport equation gives for example for water:

$$\frac{\partial \rho Y_{\mathrm{H_2O}}}{\partial t} + \nabla \cdot \left(\rho Y_{\mathrm{H_2O}} \mathbf{v}\right) = \nabla \cdot \rho D_{\mathrm{H_2O},m} \nabla Y_{\mathrm{H_2O}} + M_{\mathrm{H_2O}} k \left[\mathrm{H_2}\right] \left[\mathrm{O_2}\right]^{1/2}. \tag{2.34}$$

Nevertheless, the use of global reactions may not be sufficient in many cases, because of its applicability in a very narrow range of operating conditions. It is preferable to work with a reaction mechanism, a catalog of elementary reactions that involve many intermediates of short lifetimes. An elementary reaction should describe exactly what occurs on a molecular level. A general description of reactions also includes the backward reactions. Therefore, we end up for the general source term of species i:

$$\omega_i = M_i \sum_{r=1}^{N_r} \left[\left(\nu_{ir}'' - \nu_{ir}'\right) \left(k_{fr} \prod_{\varsigma=1}^{N_i} \left[\varsigma\right]^{\nu_{\varsigma r}'} - k_{br} \prod_{\varsigma=1}^{N_i} \left[\varsigma\right]^{\nu_{\varsigma r}''} \right) \right]. \tag{2.35}$$

By looking only at the time derivatives and the chemical source term, we face a problem of non-linear **O**rdinary **D**ifferential **E**quations (**ODE**):

$$\rho \frac{d\mathbf{Y}}{dt} = \boldsymbol{\omega}(\mathbf{Y}). \tag{2.36}$$

The computational cost increases with the number of species and reactions that we consider. But computational costs also arise from the calculation of the chemical source term itself. ω_i is non-linear with regards to T and p, especially, because of the exponential dependency of the Arrhenius function. This makes the set of equation very stiff, with characteristic chemical time scales that can range from 10^{-10} s to 1 s [107]. Many methods, denoted **B**ackward **D**ifferentiation **F**ormula (**BDF**), have been developed to solve stiff ODE system. The first of these BDF is the Euler implicit scheme:

$$\mathbf{Y}^{n+1} - \mathbf{Y}^{n} = \frac{\Delta t}{\rho} \boldsymbol{\omega}(\mathbf{Y}^{n+1}). \tag{2.37}$$

Applying Newton-Raphson at the function **G** that must converge to zero with the iteration index (l), leads to:

$$\mathbf{Y}^{n+1}_{(l+1)} = \mathbf{Y}^{n+1}_{(l)} + \frac{\mathbf{G}_{(l)}}{\left(\frac{d\mathbf{G}}{d\mathbf{Y}^{n+1}}\right)_{(l)}} = \mathbf{Y}^{n+1}_{(l)} + \frac{\mathbf{Y}^{n+1}_{(l)} - \mathbf{Y}^{n} - \frac{\Delta t}{\rho}\boldsymbol{\omega}(\mathbf{Y}^{n+1}_{(l)})}{\bar{\bar{\mathbf{I}}} - \Delta t\, \bar{\bar{\mathbf{J}}}_{(l)}}. \tag{2.38}$$

The term $\bar{\bar{\mathbf{J}}}$ appearing in the previous equation is the Jacobian matrix, defined by:

$$\bar{\bar{\mathbf{J}}} = \frac{d\left(\boldsymbol{\omega}/\rho\right)}{d\mathbf{Y}}. \tag{2.39}$$

Thereafter, $\bar{\bar{\mathbf{J}}}$ is a N_ixN_i matrix, whose element at position i, j is given by $J_{i,j} = \frac{\partial\left(\omega_i/\rho\right)}{\partial Y_j}$. Equation 2.38 can be rearranged into

$$\left(\bar{\bar{\mathbf{I}}} - \Delta t\, \bar{\bar{\mathbf{J}}}_{(l)}\right) \mathbf{Y}^{n+1}_{(l+1)} = -\Delta t\, \bar{\bar{\mathbf{J}}}_{(l)} \mathbf{Y}^{n+1}_{(l)} + \mathbf{Y}^{n} + \frac{\Delta t}{\rho}\boldsymbol{\omega}(\mathbf{Y}^{n+1}_{(l)}). \tag{2.40}$$

The previous equation can be solved after just a couple of iterations. However, solving chemistry is often the bottleneck of combustion simulations. Especially, the Jacobian calculation may be very time-consuming, as the matrix size grows quadratically with the number of species. Even if the matrix is sparse, the computation cost can be high, and thus the matrix is often only estimated at the first iteration, or at best, analytically solved. In combustion applications, species transport equation may represent easily 95 % of the total computation time. The eigenvalues of the Jacobian can deliver information on the system of equations stiffness. The stiffness can be characterized by the ratio of the negative real parts of the eigenvalues. The system is stiff if this ratio differs by several orders of magnitude. The positive eigenvalues indicate unstable nodes that also need to be reproduced accurately. For all simulations that have been performed in this work, the chemical source term has been solved with an Euler implicit scheme, and the Jacobian calculated by numerical approximation. Euler implicit is A-stable, which means that its region of absolute stability includes all complex eigenvalues with a negative real part.

The experimental data of our test case [109] are given along the axis of symmetry, as well as radial data at several positions above the burner. For first validation, the test case is run with global chemistry with the native solver of OpenFOAM. The convergence is very fast and can be run on a single core. The

temperature field is displayed in Figure 2.1b on the left side. However, for this first simulation, the flame is too stretched. For example, along the axis, the temperature peak is at 75 mm above the burner against 50 mm in the experiment, which represents an error of 50 %. The deviation lies in the species diffusion modeling. OpenFOAM can store transport data of individual species. For example, the viscosity can be given with Sutherland's correlation. In practice, the viscosity is calculated in each cell by mass averaging the contribution of each species. This gives a pretty accurate local value of the gas viscosity. However, the original OpenFOAM release is using the kinematic viscosity for the mass diffusivity. They are in reality not identical, the Schmidt number is defined by the ratio of both quantities:

$$\mathrm{Sc} = \frac{\nu}{D} = \frac{\mu}{\rho D}. \tag{2.41}$$

For gas mixtures, a Schmidt number of 0.7 is often taken. The flame temperature is also too high. Similarly, the thermal diffusivity a is by default calculated with the kinematic viscosity. The Prandtl is defined by:

$$\mathrm{Pr} = \frac{\nu}{a} = \frac{c_p \mu}{\lambda}. \tag{2.42}$$

This led to an underestimated heat conductivity as given by Fourier's law. A Prandtl number of 0.7 can also be chosen. Right side of Figure 2.1b shows the results of the simulation with corrected Schmidt and Prandtl numbers. The mass diffusivity and thermal diffusivity are increased, making the flame shorter by favoring the reactant mixture and reducing the maximum temperature by diffusing the heat.

Many hydrogen mechanisms can be found in the literature. For the current test case, we will use the mechanism that will further be used for ethylene glycol oxidation. Only a few species and reactions of this mechanism have to be considered here, specifically 9 species and 23 reactions. Besides the major species, H_2, O_2, N_2, and H_2O, 5 radicals are involved, O, H, OH, H_2O_2, and HO_2. It is, nevertheless, an important part of the mechanism. We will also make sure that the solver can solve the chemical source terms correctly. The numerical method must be robust enough to handle the stiffness of the problem.

CFD contour of the combustion product, H_2O is shown in Figure 2.1c for global chemistry and detailed one: differences can barely be observed. In this particular case, using a detailed mechanism has little impacts on the simulation. The flame is mainly controlled by the laminar transport of the reactants, H_2 and O_2. Comparison between quantitative results of global and detailed mechanism

are not explicitly done in the following, as very little difference can be observed.

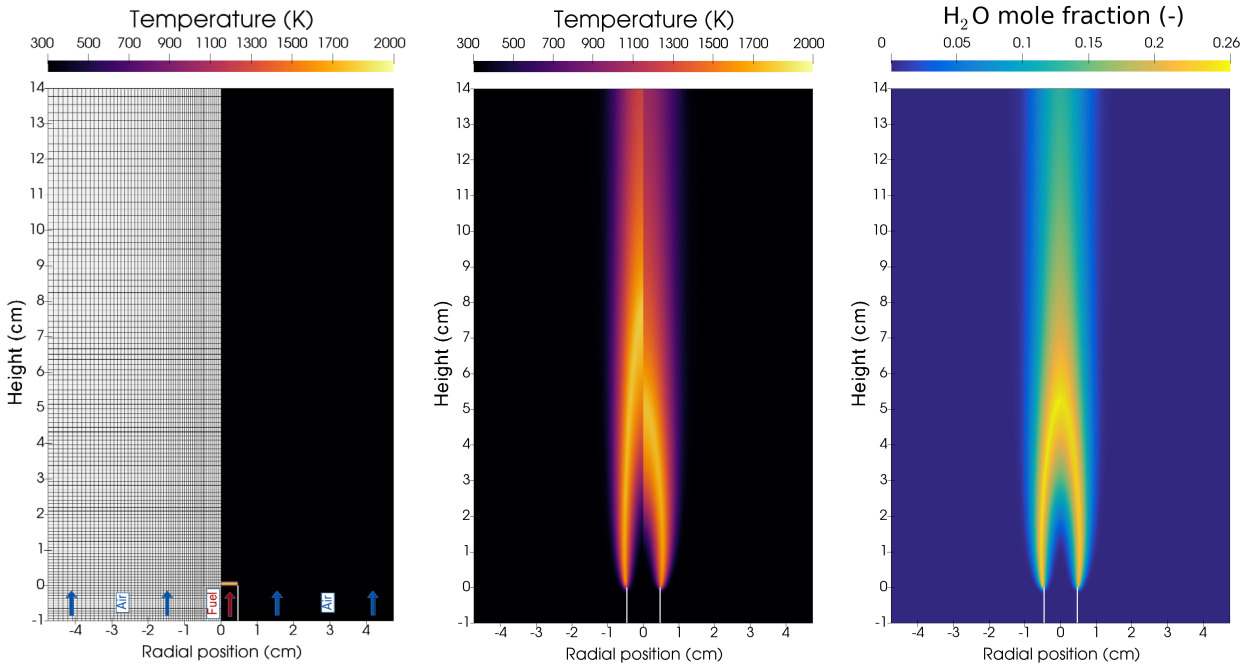

A) Left side: mesh coarsened by a factor 4; Right side: Initial temperature field with the ignition zone

B) Left side: Temperature field for Sc=Pr=1; Right side: Temperature field for Sc=Pr=0.7

C) Left side: Water mass fraction with global chemistry; Right side: Water mass fraction with detailed chemistry

FIGURE 2.1: CFD plots of a hydrogen laminar flame at initial conditions (part 2.1a) and at steady state (parts 2.1b and 2.1c)

The quantitative results for the detailed chemistry simulation can be seen in Figure 2.2; along the axis in Figure 2.2a, and along the radius at 20 mm above the burner in Figure 2.2b. The results agree globally very well. The product of the reaction, H_2O, and also O_2 are very well predicted. The temperature is slightly overestimated, but its profile is matching the one of the experimental data. The overestimation may be due to the choice of the Prandtl number or to particular species diffusion. We can see on the plot, from 5 to 55 mm some deviations between H_2 and N_2. In the experiments, N_2 increases faster to the profit of H_2 than in the simulation. This is very likely due to the fact that particular diffusion has not been modeled. Indeed, H_2 can diffuse to the flame much faster than N_2. This phenomenon is accredited by the fact that the difference in N_2 and H_2 concentrations begin very early in the experiments, in the zone where the temperature is still at room temperature and no reactions occur. OpenFOAM calculates a single diffusion coefficient in every cell. Better results would be expected by calculating a diffusion coefficient between each pair, or at least one

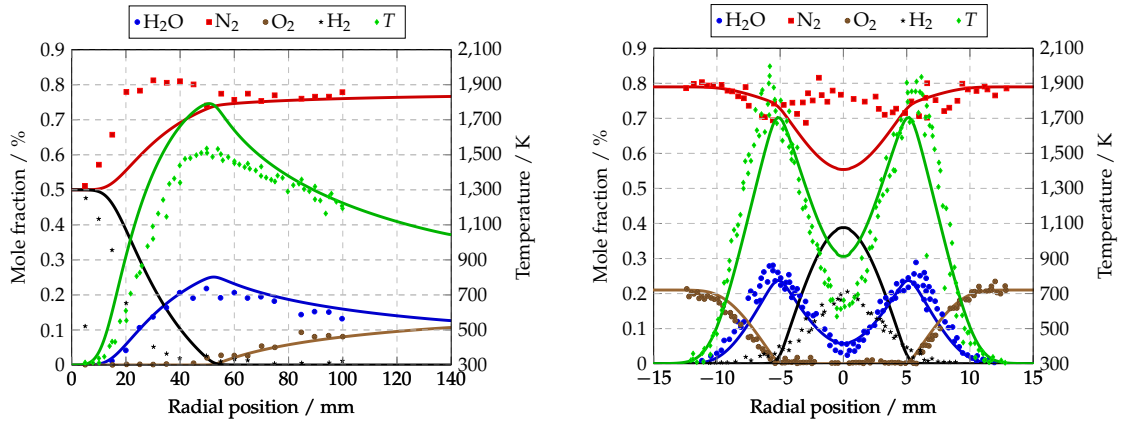

A) Results along the axis of symmetry

B) Results along the radius 20 mm above the burner

FIGURE 2.2: Experimental [109] and simulation results of a hydrogen laminar flame. Temperature and major species – H_2O, N_2, O_2, H_2 – are displayed.

coefficient for each species with the gas mixture. Another source of discrepancy can be the absence of the thermophoresis modeling.

The present case is mainly controlled by diffusion. As we will consider higher Reynolds number applications, the diffusion terms will become small in comparison to the turbulent transport terms. The next section will deal with turbulence modeling.

2.3 Turbulence

2.3.1 Overview

Hitherto, no mention about the flow regime was made. The previous laminar example showed a single and stable flow structure. Osborne Reynolds, in his experiment of 1883 [111], studied the transition criterion after which the motion becomes *sinuous* to reemploy Reynolds wording. The turbulent regime is characterized by chaotic flow motions, with multiscale fluctuating vortices.

A well accepted theory to describe turbulence is the concept of an energy cascade. Turbulence consists of 3D eddies of different sizes. An eddy is a localized flow structure. The larger eddies tend to break down and form smaller eddies, which can in their turn transfer their energy to smaller eddies and so on. A lower limit size has been introduced by Kolmogorov [112]. It is stated that the

smallest eddies are of the scale where the molecular viscosity dissipates the turbulent energy as heat. In other words, a scale at which the viscosity can damp out any velocity gradient. This scale is defined by:

$$\eta = \left(\frac{\nu^3}{\varepsilon}\right)^{\frac{1}{4}}. \tag{2.43}$$

And the associated time scale is given by:

$$t_\eta = \left(\frac{\nu}{\varepsilon}\right)^{\frac{1}{2}}. \tag{2.44}$$

In the latter equations, epsilon is the average rate of dissipation. It can be noted that the Reynolds number which express the ratio of inertial to viscous forces is equal to one at the Kolmogorov scale. Also, since no intermediate eddy scales predominate, it may be assumed that the energy transfer rate is constant at all scales.

The Navier-Stokes equations formerly presented are still valid for turbulent flows. The equations are based on conservation laws that are exact, they contain turbulence. However, if one wants to fully resolve any turbulent flow, the size of the grid should be chosen according to all involved spatial and time scales, which means from the smallest eddy to the largest one, also called integral scale. This type of simulation is called **D**irect **N**umerical **S**imulations (**DNS**) and the computational effort can be extremely prohibitive. The number of mesh points necessary grows with Re at the power of 2.5 and so does the number of time steps. Therefore, DNS simulations are restricted to limited Re numbers and to reduced geometries and simulation times. If no engineering applications are currently possible, DNS are parts of many academic researches. Their computational costs are compensated by a mass of data that can be extracted, much more detailed than experiments could deliver. They are used to validate or elaborate turbulence models with a priori or a posteriori methods. They also find applications in combustion applications to investigate the interaction between turbulence and chemistry, an issue addressed in the next section.

It appears necessary to reduce the computational effort when solving turbulent flows. While DNS computes the whole turbulence spectra, other methods have been developed that model the whole spectrum or parts of it. Two main

methods are popular, Reynolds-Averaged Navier-Stokes and Large Eddy Simulation. A multitude of hybrids is also studied, such as VLES, LNS, DES, PITM, PAN and so on. It is not intended to deepen the subject of turbulence modeling here. The following will be restricted to the overview of LES and RANS approaches and to the explanation of the choice made for the current work, while pointing out its limitations.

Large Eddy Simulations are based on a spatial statistical filtering. LES compute the structures that are larger than the filter width, and model the smaller turbulent scales. The convolution space filtering is given with Pope's notation [113]:

$$\langle \Phi(\mathbf{x}, t) \rangle = \int_{-\infty}^{+\infty} \Phi(\mathbf{x} - \boldsymbol{\varsigma}, t)\, G(\boldsymbol{\varsigma})\, d\boldsymbol{\varsigma}, \tag{2.45}$$

where G is the filtering kernel that can be of various types, box filter, Gaussian filter, or spectral filter for example. This approach is less computationally expensive than DNS, but is still very demanding and requires massively parallel machines. Only recent increases of computational capabilities tend to enable a switch from RANS to LES calculations for industrial cases.

The second approach, RANS, was the first approach developed, and its very low computational effort makes it also the most used. If the Reynolds averaging can be applied to several quantities (space averaging, ensemble averaging), it usually refers to time averaging. Let's Φ denote a random variable of time and space, Reynolds suggested [114] that this variable could be decomposed into a mean component and a fluctuating term:

$$\Phi = \overline{\Phi} + \Phi'. \tag{2.46}$$

The time-averaged of Φ is given by:

$$\overline{\Phi}(\mathbf{x}) = \lim_{\tau \to \infty} \frac{1}{\tau} \int_{t}^{t+\tau} \Phi(\mathbf{x}, t)\, dt. \tag{2.47}$$

In practice, the time period is not infinite, simply larger than the fluctuations time scales, and it is possible to follow the slow mean variations of Φ. The rules that satisfies the Reynolds operator for various operations can be derived ($\overline{\Phi_1 + \Phi_2}$, $\overline{\Phi_1 \Phi_2}$, $\overline{\nabla \Phi}$, ...). Then, as explicitly given by its name, the Reynolds averaging applied to the Navier-Stokes equations gives the Reynolds-Averaged

Navier-Stokes equations. For an incompressible flow, the continuity and momentum equations become

$$\nabla \cdot \left(\rho \overline{\mathbf{v}}\right) = 0, \tag{2.48}$$

$$\frac{\partial \rho \overline{\mathbf{v}}}{\partial t} + \nabla \cdot \left(\rho \overline{\mathbf{v}}\, \overline{\mathbf{v}}\right) = -\nabla \overline{p} + \nabla \cdot \left(\overline{\overline{\boldsymbol{\tau}}}\left(\overline{\mathbf{v}}\right) - \rho \overline{\mathbf{v}'\mathbf{v}'}\right) + \rho \mathbf{g}. \tag{2.49}$$

The time derivative is let as such here, but should not appear in RANS equations. Letting the derivative term may allow solving the variation of the mean components and is called unsteady RANS. A new and problematical term appears, $\rho\overline{v'v'}$, called Reynolds stress tensor and denoted $\overline{\overline{\boldsymbol{\tau}}}_t$. This symmetric tensor brings 6 new unknowns, and therefore new equations expressed with the mean velocity $\overline{\mathbf{v}}$ are needed to close the system. It is denoted as turbulence modeling and is discussed in the next section. The laminar stress tensor keeps a similar form as before, but expressed with the mean velocity. For highly turbulent cases, this term is negligible in comparison to the turbulent stress tensor.

For a compressible flow, because of the density's possible fluctuations, simplifications applicable for incompressible flow can not be done. In particular $\overline{\rho\Phi} = \overline{\rho}\,\overline{\Phi} + \overline{\rho'\Phi'}$. In this case, the Favre averaging is more appropriate. We decompose Φ into $\Phi = \widetilde{\Phi} + \Phi''$, where $\widetilde{\Phi} = \dfrac{\overline{\rho\Phi}}{\overline{\rho}}$, so that $\overline{\rho\Phi} = \overline{\rho}\widetilde{\Phi} + \cancel{\overline{\rho\Phi''}} = \overline{\rho}\widetilde{\Phi}$. The use of a density weighted velocity simplifies greatly the notations of the NS equations for compressible flows, which reads:

$$\frac{\partial \overline{\rho}}{\partial t} + \nabla \cdot \left(\overline{\rho}\widetilde{\mathbf{v}}\right) = 0, \tag{2.50}$$

$$\frac{\partial \overline{\rho}\widetilde{\mathbf{v}}}{\partial t} + \nabla \cdot \left(\overline{\rho}\widetilde{\mathbf{v}}\widetilde{\mathbf{v}}\right) = -\nabla \overline{p} + \nabla \cdot \left(\overline{\overline{\boldsymbol{\tau}}}\left(\widetilde{\mathbf{v}}\right) - \overline{\rho v'' v''}\right) + \overline{\rho}\mathbf{g}. \tag{2.51}$$

In this case, the turbulent stress tensor is given by $\overline{\overline{\boldsymbol{\tau}}}_t = \overline{\rho v'' v''}$.

2.3.2 Closure models

The modeling of the Reynolds stress tensor was first proposed by Boussinesq in 1877. The Boussinesq hypothesis states that the Reynolds stress can be written in analogy with the molecular motion due to molecular viscosity:

$$\overline{\overline{\boldsymbol{\tau}}}_t = \mu_t \left[\nabla \mathbf{v} + \left(\nabla \mathbf{v}\right)^{\mathsf{T}}\right] - \frac{2}{3}\left[\rho k_t + \mu_t \left(\nabla \cdot \mathbf{v}\right)\right] \overline{\overline{\mathbf{I}}}. \tag{2.52}$$

This formula can be applied for both incompressible and compressible flows,

with corresponding terms (mean velocity/density weighted velocity). Again, if the flow is incompressible, the divergence of the velocity is null and the last term is dropped. Two new terms have been used: μ_t, the turbulent viscosity and k_t, the turbulent kinetic energy. Several models have been established to calculate the turbulent viscosity. The most popular models are the two-equation models, which mean that 2 supplementary transport equations are solved. The model used for this work is the so-called **S**hear **S**tress **T**ransport (**SST**) $k-\omega$ model, which is derived from the BSL $k-\omega$ model of Menter, which itself is a combination of two models, the $k-\varepsilon$ model of Jones and Launder, and the $k-\omega$ model of Wilcox. In the $k-\varepsilon$ model, we solve for the turbulent kinetic energy and for ε, the rate of dissipation, while in the $k-\omega$ model, we are solving for k_t and ω, the rate at which turbulence kinetic energy is converted into internal thermal energy per unit volume and time. μ_t is related to the other transported variables by:

$$\mu_t = \rho \frac{k_t}{\omega} \tag{2.53}$$

and

$$\mu_t = 0.09\rho \frac{k_t^2}{\varepsilon}. \tag{2.54}$$

The $k-\varepsilon$ model performs well for free-shear flows but fails regarding flow in the vicinity of solid walls. On the contrary, the $k-\omega$ model can be integrated all the way to the wall but is very sensitive in free streams. The SST $k-\omega$ model combines strength of both methods, and has shown good robustness and performances. The model has been used as such from OpenFOAM, and thus we will not go into a more detailed description of these models.

2.3.3 Limitations of RANS approach

Large Eddy simulations are more expensive than RANS, but they also allow to capture more physical phenomena of a flow. It is necessary to verify that the choice of RANS calculations is adapted to the foreseen objectives.

Only LES can capture transient turbulent structures; RANS only gives the main time-averaged flow structure. Consequently, some important flow patterns may be lost and impact the results. The gas also interacts with the liquid, and solving the swirling would modify the droplets trajectories. In other words, averaging the gas phase flow also averages the liquid one. RANS also can not reproduce unsteady flame behaviors, such as ignition, quenching or instabilities. An important combustion instability is thermoacoustics. Thermoacoustics arise

from the interactions between pressure and heat release oscillations produced by the flame. LES is able to reproduce these instabilities, at the condition that numerical diffusion is kept small, which means high order schemes and small time steps. However, some elements favor RANS for the present case:

- No particular thermoacoustic issues have been reported with the REGA reactor, neither in experiments [97], nor in LES [101].
- Only steady states are investigated in this work. The published results were taken after letting the reactor run for a long time, simulation must by consequence also reach this steady state. In fact, the time scale associated to the flame is very small in comparison to the time the reactor needs to reach steady state. The time-accelerating procedures of steady state simulations is an asset for this purpose
- The reactor is perfectly symmetric, reducing the computational domain to a 2D-axissymetric case curtails drastically the number of cells and thus the computational effort. But LES only performs 3D calculations. Not taking advantage of this geometry simplicity would have a large penalty.
- In the view of achieving reactor design, scale up, or parameter studies, we need fast simulations. A single Large Eddy Simulation of REGA would take months to complete, even with high computing resources. The choice of RANS simulations in this work enables to perform several cases, to test different operating conditions, or to perform parameter sensitivity analysis.

For these reasons, RANS-based simulations have been privileged to model the entrained-flow gasification. As it will be exposed in Chapter 3, a volume-averaging of the governing equations will be performed, rather than a time-averaging. Nevertheless, it results in similar form, and the closure models can be used as such.

2.4 Chemistry turbulence interaction

2.4.1 Combustion model desideratum

The turbulence analysis presented in the previous section only concerned the Navier-Stokes equations reduced to the continuity and momentum equations.

The turbulence modeling also applies to the energy equations and the species transport equations. In fact, turbulence and chemical reactions are closely connected in a turbulent flame. The turbulence can enhance chemical reactions, as it can improve the mixing of fuel and oxidizer, or it can disturb the flame and conduct to local extinctions. The chemical reactions also modify the turbulence. The strong heat release may accelerate streamlines and generate additional eddies or on the contrary decrease turbulence by increasing the gas viscosity. This interaction can be seen by applying Reynolds averaging to a single species:

$$\frac{\partial \rho \overline{Y}_i}{\partial t} + \nabla \cdot \left(\rho \overline{Y}_i \overline{\mathbf{v}} \right) = \nabla \cdot \left(\frac{\mu_t}{\mathrm{Sc}_t} \nabla \overline{Y}_i \right) + \overline{\dot{\omega}}_i. \tag{2.55}$$

In the previous equation, a closure has already been applied on the first term of the right side. We reuse the turbulent viscosity term from the Boussinesq hypothesis divided by a turbulent Schmidt number. This expression takes a similar form than the laminar diffusivity, which has been supposed negligible in the previous equation. The second term on the right side of this equation is the averaged chemical source term. Averaging this highly non-linear term is a difficult mathematical task; additional modeling is needed.

2.4.2 Combustion models

As for the turbulence modeling, the purpose of this section is not to give an exhaustive review of combustion modeling, but to show which elements motivate or discredit a model applied to our current application. Models of various complexities have been developed. Basic models can rely on two opposite hypotheses. One the one hand, the chemistry can be considered very fast, therefore, the combustion process is totally controlled by the turbulent mixing time. The first model of this type is the Eddy Break-Up model, developed by Spalding. It was further extended by Magnussen et al. with the **E**ddy **D**issipation **M**odel (**EBM**). For this model, the reaction is simply global from fuel and oxidizer into products and the chemical source term can be written:

$$\overline{\dot{\omega}}_i = A_{\mathrm{E}} \frac{\rho \nu_i' M_i}{\tau_t} \min \left(\frac{\overline{Y}_F}{\nu_F' M_F}, \frac{\overline{Y}_O}{\nu_O' M_O}, B_{\mathrm{E}} \frac{\overline{Y}_P}{\nu_P' M_P} \right), \tag{2.56}$$

where $\tau_t = \dfrac{k_t}{\varepsilon}$ is the turbulent mixing time. On the other hand, the combustion process may also be exclusively controlled by the chemistry. We return to

the **F**inite **R**ate **C**hemistry (**FRC**) model of section 2.2.2, but instead of the instantaneous species mass fraction, we use the averaged one. Both hypotheses are usually too restrictive, therefore, EDM and FRC are often used together. We compute, for each cell, both source terms, and then we take the smaller one, i.e. the limiting one. This method is robust and can be applied to a wide range of applications. However, it only takes into account either the chemistry or the turbulence, not the **T**urbulence **C**ombustion **I**nteraction (**TCI**).

Another paradigm is to account for the TCI with **P**robability **D**ensity **F**unctions (**PDF**). The so-called assumed PDF approach helps calculating the local mean chemical production rates by assuming the fluctuations with a distribution function. The chemical production rate is a function of the concentration of species i (that is further linked to species mass fraction) and temperature. We define the associated sample space variables $\breve{Y}_1$,$\breve{Y}_2$, ...,$\breve{Y}_{N_i}$,$\breve{T}$ and the joint PDF P. The first moment of the PDF also corresponds to the mean value:

$$\overline{\dot{\omega}}_i = \int \dot{\omega}_i \left(\breve{Y}_1, ..., \breve{Y}_{N_i}, \breve{T}\right) P \left(\breve{Y}_1, ..., \breve{Y}_{N_i}, \breve{T}\right) d\breve{Y}_1 ... d\breve{Y}_{N_i} d\breve{T}. \tag{2.57}$$

The previous equation can be integrated by presuming the shape of the PDF P. For example, Gerlinger [115] chose a Gaussian distribution for temperature and a multivariate β-PDF model for the species concentrations. This approach is a simplified view (mathematically and computationally) of the evolution or transported PDF of Pope [116]. The approach can be applied solely with the mass fractions, giving the composition joint PDF equation, or velocity can also be taken into account. This last case gives the velocity-composition joint PDF equation:

$$\begin{aligned} \rho\left(\breve{Y}\right)\frac{\partial P}{\partial t} + \rho\left(\breve{Y}\right)\mathbf{v}\nabla\cdot(P) + \left(\rho\left(\breve{Y}\right)\mathbf{g} - \nabla\overline{p}\right)\cdot\nabla_v P \\ + \sum_{i=1}^{n}\frac{\partial}{\partial Y_i}\left[\rho\left(\breve{Y}\right)\omega_i\left(\breve{Y}\right)P\right] \\ = \nabla_v\cdot\left[\langle -\nabla\cdot\overline{\overline{\boldsymbol{\tau}}} + \nabla p' | \breve{\mathbf{v}}, \breve{Y}\rangle P\right] \\ - \sum_{i=1}^{n}\frac{\partial}{\partial Y_i}\left[\langle \nabla\cdot\overline{\overline{\mathbf{J}}}_i | \breve{\mathbf{v}}, \breve{Y}\rangle P\right]. \end{aligned} \tag{2.58}$$

In the last equation, the chemical source terms are closed, and the TCI is captured in a direct manner, with minimal approximations. However, terms on the left are unclosed and need modeling. Another issue is the impossibility to solve this transport equation on our FV mesh due to the high dimensionality of

the PDF. The solution employed is generally with a Monte-Carlo method, and the particle evolution follows a lagrangian approach.

The method used for this work is the **Pa**rtially **S**tirred **R**eactor (**PaSR**) model available in OpenFOAM. This model is close to the Eddy dissipation concept, which suggests that reaction takes place where the dissipation of the turbulence energy is high. Concretely, the CFD cells are divided in two zones, one referring to the fine structure, and the other to the surrounding fluid. A difference between both models being that EDC is using global parameters that require the a priori knowledge of system scales. In the PaSR model, the mean chemical source term of species i is given by:

$$\overline{\dot{\omega}}_i = \gamma^* \dot{\omega}_i \left(\overline{Y} \right), \tag{2.59}$$

where

$$\gamma^* = \frac{\tau_c}{\tau_c + C_{mix}\tau_t}. \tag{2.60}$$

The turbulent mixing time τ_t is the same as in the EDM, and the chemical time scale τ_c is taken as the largest of the individual time scales, which can be estimated by

$$\tau_{c,i} = \frac{Y_i}{\left| \frac{dY_i}{dt} \right|}. \tag{2.61}$$

2.5 Multiphase flow approaches

So far, the numerical modeling only concerned combustion of a single gas phase. Many combustion applications involve a second phase, liquid or solid, such as in diesel or coal combustion. A variety of approaches have been developed. In particular, spray is an important branch of multiphase flow modeling. An objective of this work is to model a slurry spray. To begin with, we may only consider a liquid injection. The phenomena involved (spray primary and secondary atomization, polydispersity, SMD) have been presented in the introduction. The purpose of this section is to review some of the existing models, while Chapter 3 will be dedicated at presenting in more details the model employed.

As the main phase is treated in an Eulerian fashion, the CFD modeling of two-phase flows can be quickly divided into two distinct approaches: the so-called **E**ulerian–**L**agrangian (**EL**) method if the second phase is considered in a Lagrangian manner, the **E**ulerian–**E**ulerian (**EE**) method otherwise.

2.5.1 Lagrangian methods

The first of the EL method is the Lagrangian particle tracking method, also referred to as **D**iscrete **P**article **S**imulation (**DPS**). In this framework, numerical points are used to track physical droplets. It is the most widely used method due to inherent advantages. It is an intuitive representation as discrete points represent individual droplets, it is easy to implement and to solve, and it can be used for a variety of applications. Under the Lagrangian framework, the motion of a random particle (or droplet here) is given by ODEs after Newton's second law:

$$\frac{dm_l \mathbf{v}_l}{dt} = \sum \mathbf{F}, \tag{2.62}$$

$$\frac{d\mathbf{x}_l}{dt} = \mathbf{v}_l. \tag{2.63}$$

The subscript l refers to the liquid phase, or here to a liquid droplet. The mass is often considered constant and thus the acceleration vector can be easily integrated knowing the forces involved, which are often primarily composed of drag force and gravitation.

However, this method has some drawbacks. First, it relies on the point particle assumption, which means that particles do not take up space of the surrounding fluid. Second, in many cases, the correspondence one numerical point for one physical droplet is not respected. We define parcels, which encompass several physical particles in an attempt to reduce the computational cost. Also, this approach has a narrow range of applicability. It is valid for dilute flows. In this sense, it is well adapted to the far-field region of the spray. But problems arise for the bulk flow at the near-field primary atomization region. This region is either omitted or consists of very large parcels. If one wants to fully describe the spray in a consistent manner, it is necessary to couple the LE approach with an EE model. A last hindrance of Lagrangian approach is the scalability. Parallelization of the domain requires complex partitioning methods.

2.5.2 Eulerian methods

Lagrangian methods fail conceptually to describe two-phase flows with separated regions, thus the need to investigate Eulerian approaches. Interest for Eulerian description of multiphase flows is growing, and numerous works intend to tackle the mathematical modeling difficulties of this approach. Eulerian methods can be classified into a degree of accuracy, from the mixture models, to

the two-fluid models without interface and finally to the two-fluid models with interface.

In the simplest models, the mixture models, only one set of NS equations are solved for a so-called mixture phase. It requires therefore homogeneous conditions and strong coupling between the phases, which is not the case for a spray. At the opposite level of details, the two-fluid models with interface presuppose two immiscible fluids. The fluids interface is tracked which offers a high-fidelity representation of gas and liquid interaction, both for stratified flows and free moving droplets. However, taking into account the number of droplets to consider or the size of the droplet in comparison to the reactor size, computation would be unrealizable and this level of detail is also, in our case, not required. The two-phase models without interface interpret both phases as fully interpenetrating continua, coupled by an interaction term. This last formulation is employed in this work; further details will be given in the next chapter. A two-fluid model, despite being more complicated than a mixture model, is able to predict more accurately phase changes and phase interactions. It is particularly suited when there is non-equilibrium between phases. This is clearly the case here, as the liquid enters with a velocity two orders of magnitude smaller than the gas one, and we do have an important temperature difference between the droplet and the surrounding gas.

Chapter 3

Eulerian-Eulerian approach for liquid spray modeling

The mathematical basis for two-phase flows both treated as continua were conducted by Ishii [117] and Drew [118]. Many two-fluid models have been developed, for example the seven-equation model of Baer and Nunziato [119] or of Saurel and Abgrall [120], or the five-equation model of Allaire [121]. The model of interest here follows Ishii's model, which is expressed by *two sets of conservation equations governing the balance of mass, momentum and energy in each phase*. Both phases also interact with each others. This is expressed by three interaction terms in these balance equations. In addition, as the gas phase is multicomponent and reacting, species transport equations will be derived in the context of two-phase flows. The liquid phase will be first assumed as a single component phase, made of ethylene glycol.

In OpenFOAM, a first solver (named bubbleFoam) was developed by Henrik Rusche [122] for the simulation of dispersed two-phase flows. It was then generalized resulting in the solver reactingTwoPhaseEulerFoam used for this work. This solver is presented as a *solver for a system of 2 compressible fluid phases with a common pressure, but otherwise separate properties*. This solver has been modified for the purpose of this work to include an appropriate evaporation modeling. The changes are listed in section 3.2.1. The objective of this chapter is to present the conservation equations, the solution procedure, the closure and also the interactions between the phases, namely the mass, momentum, energy and species phase transfer.

3.1 Governing equations

The governing equations for two-phase flows can be derived from a control volume as conducted in section 2.1.1 for a single phase. We extend the consideration by constituting the control volume with several phases p, separated by an interface $\mathscr{S}_{I,p_ip_j}$. The control volume and the control surface respect $\bigcup_p \mathscr{V}_p = \mathscr{V}$ and $\bigcup_p \mathscr{S}_p = \mathscr{S}$. The overall balance equation for a random variable Φ within the control volume gives:

$$\begin{aligned}\sum_p \frac{d}{dt}\left(\int_{\mathscr{V}_p(t)} \rho\Phi d\mathscr{V}\right) = &-\sum_p \int_{\mathscr{S}_p(t)} \mathbf{j}\cdot d\boldsymbol{\mathscr{S}} + \sum_p \int_{\mathscr{V}_p(t)} \dot{Q}^{\Phi} d\mathscr{V} \\ &+ \frac{1}{2}\sum_{p_i}\sum_{p_j}\left(1-\delta_{ij}\right)\int_{\mathscr{S}_{I,p_ip_j}(t)} \dot{Q}_I^{\Phi} d\mathscr{S}_{I,p_ip_j}.\end{aligned} \tag{3.1}$$

As compared to equation 2.5, the transport of Φ is here given by the contribution of all phases p. A new term also arises, which corresponds to the coupling interfacial source term, δ_{ij} being the Kronecker delta. Contrary to the single phase analysis, the individual phase volume inside the CV is considered time-dependent, $\mathscr{V}_p = \mathscr{V}_p(t)$. Especially, the interface element has a displacement of velocity $\mathbf{v}_{I,p_ip_j}$ and the Reynolds transport theorem has to be accounted in its full formulation. It gives, for example, for the time derivative term:

$$\begin{aligned}\sum_p \frac{d}{dt}\left(\int_{\mathscr{V}_p(t)} \rho\Phi d\mathscr{V}\right) = &\sum_p \int_{\mathscr{V}_p(t)} \frac{\partial\rho\Phi}{\partial t} d\mathscr{V} \\ &+ \frac{1}{2}\sum_{p_i}\sum_{p_j}\left(1-\delta_{ij}\right)\int_{\mathscr{S}_{I,p_ip_j}(t)} \rho\Phi\mathbf{v}_{I,p_ip_j}\cdot d\boldsymbol{\mathscr{S}}_{I,p_ip_j}.\end{aligned} \tag{3.2}$$

Applying Gauß theorem on the flux through $\mathscr{S}$ and further manipulations of equation 3.1 read:

$$\begin{aligned}&\sum_p \int_{\mathscr{V}_p(t)} \left[\frac{\partial\rho\Phi}{\partial t} + \nabla\cdot\mathbf{j} - \dot{Q}^{\Phi}\right] d\mathscr{V} \\ &+ \frac{1}{2}\sum_{p_i}\sum_{p_j}\left(1-\delta_{ij}\right)\int_{\mathscr{S}_{I,p_ip_j}(t)} \left[\rho\Phi\mathbf{v}_{I,p_ip_j}\cdot d\boldsymbol{\mathscr{S}}_{I,p_ip_j} - \mathbf{j}\cdot d\boldsymbol{\mathscr{S}}_{I,p_ip_j} - \dot{Q}_I^{\Phi} d\mathscr{S}_{I,p_ip_j}\right] = 0.\end{aligned} \tag{3.3}$$

The formulation above is defined for any arbitrary phase volumes and phase interfaces, and thus the integrands have to be zero, leading to the exact form of

equation 2.4 found for one phase flow:

$$\frac{\partial}{\partial t}\left(\rho\Phi\right) + \nabla\cdot\left(\rho\Phi\mathbf{v}\right) = \nabla\cdot\left(\Gamma^{\Phi}\nabla\Phi\right) + \dot{Q}^{\Phi}. \tag{3.4}$$

But equation 3.4 is only valid locally for the phase p. In multiphase flows, there has to be at least another transport equation and the second term of equation 3.3 imposes a constraint in order to close the system. The integrand of the second term accounts for the sharp interface on Φ. It gives the so-called local instantaneous interfacial jump conditions. Derivation of the local instantaneous conservation equations and the interfacial jump relations found the basis of computational multi-fluid dynamics with surface tracking. Now, for practical purposes, we need to resort to averaging procedures, akin to the time-averaging techniques applied for turbulence. The method employed is based on the conditional volume-averaging [123]. It turns the local governing equations into volume-averaged ones and the sharp interface into a continuous interface representation. We define a phase indicator function, $\mathbb{H}_p\left(\mathbf{x},t\right)$, a function whose value is one in the phase domain p and 0 elsewhere. Taking an arbitrary quantity Φ, we denote $\widehat{\Phi}$ the volume-averaged quantity. The contribution of phase p to Φ in the volume $\mathscr{V}$ (i.e. the conditioning and subsequent volume averaging) is given by:

$$\widehat{\mathbb{H}_p\Phi} = \frac{1}{\mathscr{V}}\int_{\mathscr{V}} \mathbb{H}_p\Phi\left(\mathbf{x},t\right)d\mathbf{x}. \tag{3.5}$$

It is equivalent to integrate Φ on the phase volume $\mathscr{V}_p$:

$$\widehat{\mathbb{H}_p\Phi} = \frac{1}{\mathscr{V}}\int_{\mathscr{V}_p} \Phi\left(\mathbf{x},t\right)d\mathbf{x}, \tag{3.6}$$

$$\widehat{\mathbb{H}_p\Phi} = \frac{\mathscr{V}_p}{\mathscr{V}}\frac{1}{\mathscr{V}_p}\int_{\mathscr{V}_p} \Phi\left(\mathbf{x},t\right)d\mathbf{x}, \tag{3.7}$$

$$\widehat{\mathbb{H}_p\Phi} = \alpha_p\widehat{\Phi}_p. \tag{3.8}$$

The development results in two important new terms, $\alpha_p = \frac{\mathscr{V}_p}{\mathscr{V}}$, the volume fraction of phase p and $\widehat{\Phi}_p$ the phasic or intrinsic average. This phasic average represents the average quantities relating to one particular phase only. The next steps leading to the volume averaged conservation equations follow a similar procedure than the one used for the time-averaging of the NS equations. Rules for various operations of the conditional volume averaging are derived and then, these rules are applied to the governing equations. These steps are

fully described in [124]. For example, the local instantaneous continuity equation reads:

$$\frac{\partial \rho}{\partial t} + \nabla \cdot \left(\rho \mathbf{v}\right) = 0. \tag{3.9}$$

We condition the continuity equation and we take the volume averaging:

$$\widehat{\mathbb{H}_p \frac{\partial \rho}{\partial t}} + \widehat{\mathbb{H}_p \nabla \cdot \left(\rho \mathbf{v}\right)} = 0, \tag{3.10}$$

which can be developed into

$$\frac{\partial \widehat{\mathbb{H}_p \rho}}{\partial t} + \nabla \cdot \left(\widehat{\mathbb{H}_p \rho \mathbf{v}}\right) = \rho \widehat{\frac{\partial \mathbb{H}_p}{\partial t}} + \widehat{\rho \mathbf{v} \cdot \nabla \left(\mathbb{H}_p\right)}, \tag{3.11}$$

or with simplified notations:

$$\frac{\partial \alpha_p \widehat{\rho}_p}{\partial t} + \nabla \cdot \left(\alpha_p \widehat{\left(\rho \mathbf{v}\right)}_p\right) = \widehat{\Gamma}_p. \tag{3.12}$$

The term on the right side is non-zero only at the interface, and denotes the surface averaged rate of mass introduction or removal of phase p. Further details about this term can be found in Hill's work for example [125]. Looking at the equation 3.12, we retrieve the formulation of Ishii, with governing equations for each of the phase and interaction terms. It should also be noted that $\sum_p \widehat{\Gamma}_p = 0$. In a similar manner as the account of compressibility on continuity equation, the term $\widehat{\left(\rho \mathbf{v}\right)}_p$ could be expanded and unfathomable new terms would emerge. A Favre-like (density weighted) averaging is also performed with $\widetilde{\mathbf{v}}_p = \dfrac{\widehat{\left(\rho \mathbf{v}\right)}_p}{\widehat{\rho}_p}$. Similar instantaneous equations can be derived for momentum, energy and species transport equations. The final equations are:

$$\frac{\partial \alpha_p \widehat{\rho}_p}{\partial t} + \nabla \cdot \left(\alpha_p \widehat{\rho}_p \widetilde{\mathbf{v}}_p\right) = \widehat{\Gamma}_p, \tag{3.13}$$

$$\begin{aligned} \frac{\partial \alpha_p \widehat{\rho}_p \widetilde{\mathbf{v}}_p}{\partial t} + \nabla \cdot \left(\alpha_p \widehat{\rho}_p \widetilde{\mathbf{v}}_p \widetilde{\mathbf{v}}_p\right) &= -\nabla \left(\alpha_p \widehat{p}_p\right) \\ &+ \nabla \cdot \left[\alpha_p \overline{\overline{\boldsymbol{\tau}}} \left(\widetilde{\mathbf{v}_p}\right) - \alpha_p \widehat{\rho}_p \widetilde{\left(\mathbf{v}_p'' \mathbf{v}_p''\right)}_p\right] + \alpha_p \widehat{\rho}_p \mathbf{g} + \widehat{\mathbf{M}}_p, \end{aligned} \tag{3.14}$$

$$\begin{aligned}
&\frac{\partial \alpha_p \widehat{\rho}_p \widetilde{h}_{sp}}{\partial t} + \nabla \cdot \left(\alpha_p \widehat{\rho}_p \widetilde{h}_{sp} \widetilde{\mathbf{v}}_p \right) + \frac{\partial \alpha_p \widehat{\rho}_p \widetilde{k}_p}{\partial t} + \nabla \cdot \left(\alpha_p \widehat{\rho}_p \widetilde{k}_p \widetilde{\mathbf{v}}_p \right) = \\
&\qquad - \nabla \cdot \left[\alpha_p \left(\widehat{\mathbf{j}}_{q_p} + \widehat{\mathbf{q}}_p + \widehat{\rho}_p \widetilde{\left(k_p'' \mathbf{v}_p'' \right)}_p + \widehat{\rho}_p \widetilde{\left(h_{s_p}'' \mathbf{v}_p'' \right)}_p \right) \right] \\
&\qquad \frac{\partial \alpha_p \widehat{p}_p}{\partial t} + \alpha_p \widehat{\overline{\overline{\boldsymbol{\tau}}} : \nabla \mathbf{v}}_p + \alpha_p \widehat{\rho}_p \mathbf{g} \cdot \widetilde{\mathbf{v}}_p + \alpha_p \widehat{\dot{q}}_{r_p} + \alpha_p \widehat{\dot{Q}_c}_p + \widehat{E}_p,
\end{aligned} \tag{3.15}$$

$$\begin{aligned}
&\frac{\partial \alpha_p \widehat{\rho}_p \widetilde{Y}_{p,i}}{\partial t} + \nabla \cdot \left(\alpha_p \widehat{\rho}_p \widetilde{Y}_{p,i} \widetilde{\mathbf{v}}_p \right) = \\
&\qquad \nabla \cdot \left[\alpha_p \widehat{\rho}_p \left(D_{im} \nabla \widetilde{Y}_{p,i} - \widetilde{\left(Y_{p,i}'' \mathbf{v}_p'' \right)}_p \right) \right] + \alpha_p \widehat{\dot{\omega}}_i + \widehat{\Gamma}_{p,i}.
\end{aligned} \tag{3.16}$$

Here, the sensible enthalpy has been used for the energy equation.

The equations that have been derived exhibit new terms of fluctuating quantity, e.g $-\alpha_p \widehat{\rho}_p \widetilde{\left(\mathbf{v}_p'' \mathbf{v}_p'' \right)}_p$. This last term emphasizes the velocity fluctuations that arise from the volume averaging procedure on the convective term:

$$\begin{aligned}
\nabla \cdot \left[\alpha_p \widehat{\left(\rho \mathbf{v} \mathbf{v} \right)}_p \right] &= \nabla \cdot \left[\alpha_p \widehat{\rho}_p \frac{\widehat{\left(\rho \mathbf{v} \mathbf{v} \right)}_p}{\widehat{\rho}_p} \right] = \nabla \cdot \left[\alpha_p \widehat{\rho}_p \widetilde{\left(\mathbf{v} \mathbf{v} \right)}_p \right] \\
&= \nabla \cdot \left[\alpha_p \widehat{\rho}_p \overbrace{\left(\left(\widetilde{\mathbf{v}}_p + \mathbf{v}_p'' \right) \left(\widetilde{\mathbf{v}}_p + \mathbf{v}_p'' \right) \right)}_p \right] \\
&= \nabla \cdot \left[\alpha_p \widehat{\rho}_p \left(\widetilde{\left(\widetilde{\mathbf{v}}_p \widetilde{\mathbf{v}}_p \right)}_p + 2 \widetilde{\left(\widetilde{\mathbf{v}}_p \mathbf{v}_p'' \right)}_p + \widetilde{\left(\mathbf{v}_p'' \mathbf{v}_p'' \right)}_p \right) \right] \\
&= \nabla \cdot \left[\alpha_p \widehat{\rho}_p \left(\widetilde{\mathbf{v}}_p \widetilde{\mathbf{v}}_p + 2 \widetilde{\mathbf{v}}_p \cancel{\widetilde{\left(\mathbf{v}_p'' \right)}_p} + \widetilde{\left(\mathbf{v}_p'' \mathbf{v}_p'' \right)}_p \right) \right] \\
&= \nabla \cdot \left[\alpha_p \widehat{\rho}_p \left(\widetilde{\mathbf{v}}_p \widetilde{\mathbf{v}}_p + \widetilde{\left(\mathbf{v}_p'' \mathbf{v}_p'' \right)}_p \right) \right].
\end{aligned} \tag{3.17}$$

One could argue that the equations are still instantaneous, and that it must be followed by an additional step of time-averaging to model the turbulent flows. This has been adopted by some authors in the past [126, 127]. This results in extra terms that also require modeling. Some models neglect the fluctuating term from the volume averaging while others superimpose separate models. However, the double averaging method has been abandoned in

more recent works. It was shown than a single averaging step is sufficient [128, 129]. The two-phase unsteadiness and turbulence are bounded, and an averaging of one will inevitably capture the second effect. OpenFOAM, and the work of Rusche, is based on the afore presented development, called conditional volume-averaging, where a single averaging is performed. The spatial and temporal intermittencies are enclosed solely in the Reynolds tensor $\overline{\overline{\boldsymbol{\tau}}}_{tp} = -\widehat{\rho}_p \widetilde{\left(\mathbf{v}_p'' \mathbf{v}_p''\right)}_p$, expressed according to the Boussinesq approximation:

$$\overline{\overline{\boldsymbol{\tau}}}_{tp}\left(\widetilde{\mathbf{v}}_p\right) = \mu_{tp}\left[\nabla\widetilde{\mathbf{v}}_p + \left(\nabla\widetilde{\mathbf{v}}_p\right)^{\mathsf{T}}\right] - \frac{2}{3}\left[\widehat{\rho}_p k_{tp} + \mu_{tp}\left(\nabla\cdot\widetilde{\mathbf{v}}_p\right)\right]\overline{\overline{\mathbf{I}}}. \tag{3.18}$$

The closures of the other fluctuating terms are quickly described in the following. Concerning the species equation, the closure follows the one used for equation 2.55, $-\widehat{\rho}_p \widetilde{\left(Y_{p,i}'' \mathbf{v}_p''\right)}_p = \dfrac{\mu_{tp}}{\mathrm{Sc}_{tp}} \nabla \widetilde{Y}_{p,i}$. The term $-\widehat{\rho}_p \widetilde{\left(h_{sp}'' \mathbf{v}_p''\right)}$ of the energy equation is written $a_{tp}\nabla\widetilde{h}_{sp}$, where a_{tp} is the turbulent thermal diffusivity of phase p. OpenFOAM omits many terms of the energy equation. First, the fluctuating term of kinetic energy is neglected $-\widehat{\rho}_p \widetilde{\left(k_p'' \mathbf{v}_p''\right)}$. The heat flux due to species diffusion is not implemented, but the works due to gravitation and radiation are available. The last term of the energy equation $\alpha_p \widehat{\overline{\overline{\boldsymbol{\tau}}} : \nabla \mathbf{v}_p}$ can be developed into several contributions, in which many are negligible. This term is not taken into account in the native solver. For the species and energy equations, OpenFOAM groups laminar and turbulent contributions, which simplifies the writing:

$$-\nabla\cdot\left[\alpha_p\left(\widehat{\mathbf{q}}_p + \widehat{\rho}_p \widetilde{\left(h_{sp}'' \mathbf{v}_p''\right)}_p\right)\right] = \nabla\cdot\left[\alpha_p\left(a_p + a_{tp}\right)\nabla\widetilde{h}_{sp}\right], \tag{3.19}$$

and

$$\nabla\cdot\left[\alpha_p\widehat{\rho}_p\left(D_{im}\nabla\widetilde{Y}_{p,i} - \widetilde{\left(Y_{p,i}'' \mathbf{v}_p''\right)}_p\right)\right] = \nabla\cdot\left[\alpha_p\left(\frac{\mu_p + \mu_{tp}}{\mathrm{Sc}_{tp}}\right)\nabla\widetilde{Y}_{p,i}\right]. \tag{3.20}$$

The last term of the 4 governing equations (equations 3.13 to 3.16) have not been explicitly detailed at this point. $\widehat{\Gamma}_p$, $\widehat{\mathbf{M}}_p$, $\widehat{E}_p$ and $\widehat{\Gamma}_{p,i}$ are the interface mass, momentum, energy and species mass transfer. Mathematical expressions can be derived from the conditional volume-averaging. But they are hardly exploitable. The description of each of these terms will be done in the next section. Before,

the system would not be closed if the phase volume fractions were not solved. They have to be computed. As only two phases are considered, the calculation of one phase volume fraction is sufficient, because of the relation $\alpha_{p2} = 1 - \alpha_{p1}$. The missing equation is derived from the phase continuity equation. Even if the solver is presented as handling compressible flow (and a correction is brought into the final equation), the equation of the volume fraction is obtained by assuming a constant phase density. By omitting the transfer term, it follows:

$$\frac{\partial \alpha_{p1}}{\partial t} + \nabla \cdot \left(\alpha_{p1} \mathbf{v}_{p1} \right) = 0. \tag{3.21}$$

Solving directly this last equation would be the direct way to advance the phase fraction, such as in [125, 126]. However, this equation shows two issues, it is written in a non-conservative way and it is not obviously bounded. The lower limit, 0, can be guaranteed, but not the upper limit 1. It should be noted that a small deviation in the volume fraction calculation can lead to very large continuity errors because of the important density ratio between the phases. To tackle this issue, many approaches have been investigated, a review can be found in the work of Rusche [122]. The method implemented is based on the approach of Weller [130]. We denote $\mathbf{v}_m = \alpha_{p1}\mathbf{v}_{p1} + \alpha_{p2}\mathbf{v}_{p2}$ the volumetric mixture velocity and $\mathbf{v}_r = \mathbf{v}_{p1} - \mathbf{v}_{p2}$ the relative velocity. Equation 3.21 can be rearranged into:

$$\frac{\partial \alpha_{p1}}{\partial t} + \nabla \cdot \left(\alpha_{p1} \mathbf{v}_m \right) + \nabla \cdot \left(\alpha_{p1} \left(1 - \alpha_{p1} \right) \mathbf{v}_r \right) = 0. \tag{3.22}$$

This formulation is advantageous in terms of boundedness, since $\nabla \cdot \mathbf{v}_m = 0$ for the second term and the third term becomes zero if α_{p1} approaches zero or one [124]. Still, this equation is a non-linear function of α_{p1} and must be treated adequately. The flux corrected transport introduced by Boris [131] and extended by Zalesak [132] is a technique to guarantee boundedness. Its application in OpenFOAM is called Multidimensional Universal Limiter for Explicit Solution [133]. Concretely, the solver employs a high and a low order scheme to compute a corrected flux. It also offers the possibility to set global extrema, zero and one in our case.

The continuity equation will also be used for a second purpose. Two-phase flows also have to deal with the pressure-velocity coupling. In single phase flows, the momentum equation was discretized and reinserted into the continuity equation to form the pressure equation. However, two-phase flows have two continuity equations. Deriving two pressure equations is a possibility, but

here as described in the introduction of the chapter, a common pressure field is assumed. Basically, we are looking at the continuity of the mixture. It is ensured by the volumetric mixture flux obtained by adding the continuity equation of both phases, it follows $\nabla \cdot \mathbf{v}_m = \left(\alpha_{p1}\mathbf{v}_{p1} + \alpha_{p2}\mathbf{v}_{p2}\right) = 0$. The following steps are similar to that for a single phase. Here also, the reader is referred to the treatise of Rusche [122].

3.2 Interphase transfers

The solver used is particularly robust and versatile. It can deal with two phases of various natures, with a high density ratio, for both segregated and dispersed flows. However, it is not specifically designed for liquid sprays in a continuous gas phase. The former solver dealt with gas bubbles in a continuous liquid phase. The governing equations and the main algorithm may be used as such, but the coupling between the phases requires particular treatment. Many two-phase flows problems only exchange momentum, many models have been developed to describe these interactions. In our case, the liquid mass transfer to the gas phase, from evaporation, is the decisive factor. Evaporation will also induce subsequent momentum, energy and species transfer.

This section will begin by presenting how the evaporation has been modeled, starting from the mass evaporation rate and then the other transfer sources. Continuity fulfillment will be verified, as well as an assessment against a traditional Lagrangian approach. In the next part, the momentum interphase transfer will be described.

3.2.1 Evaporation modeling

The overall objective is to define the transfer terms as they appear in equation 3.13 to 3.16. At first, we restrict ourselves to the mass transfer. So far, one random phase has been tantamount to another one. We cease to see phases as interchangeable entities and we adjust our notation, the liquid phase will be defined with l subscript and the gaseous phase with g. The global mass conservation dictates that the mass lost by a phase equals the mass gained by the other phase. As the only mass transfer to be accounted for is the liquid evaporation, we have $\widehat{\Gamma}_g = -\widehat{\Gamma}_l \geq 0$. This is of great advantage, because finding an expression for the averaged interphase mass transfer of one of the two phases is sufficient, and deriving an expression for the dispersed phase is much more

convenient. Now, the liquid phase is considered as composed of dispersed elements. In the volume $\mathscr{V}$, the liquid occupies the phase volume $\mathscr{V}_l$. We define N_l and n_l respectively the number of liquid elements (droplets) and the number density of liquid elements $n_l = \frac{N_l}{\mathscr{V}}$. As $\widehat{\Gamma}_l$ is the total mass transfer rate per volume, by denoting $\dot{m}_l$ the averaged mass evaporating rate of one element, it follows $\widehat{\Gamma}_l = -n_l \dot{m}_l = -\frac{N_l}{\mathscr{V}} \frac{\mathscr{V}_l}{\mathscr{V}_l} \dot{m}_l = -\frac{\alpha_l}{\mathscr{V}_l / N_l} \dot{m}_l$. The denominator $\mathscr{V}_l / N_l$ is the average element volume and can be rewritten V_l.

Therefore, we can simply reduce the problem to the modeling of a liquid droplet vaporization. For simplicity, we can assume the droplet as isolated and spherically symmetric. Vaporization is a surface process, the droplet surface is surrounded by a symmetric gas film. The droplet receives heat from the gas; the droplet vaporizes and the vapor, denoted v, convects and diffuses to the far field. Concurrently, the droplet looses heat from the latent heat of evaporation of the species involved, here ethylene glycol. Several models can be employed, classified by Sirignano [134], the infinite liquid conductivity model is a sufficient approach here. It assumes that a transient liquid temperature, but uniform inside the droplet. A simpler approach, with uniform and constant temperature, yields the d^2-law [135]. More sophisticated, the temperature diffusion inside the droplet is solved in the spherically symmetric transient droplet heating model. The mass rate of evaporation mainly depends on the gas properties, as shown by the widely used Spalding's evaporation rate $\dot{m}_l$ [136]:

$$\dot{m}_l = 2\pi R_l \, \mathrm{Sh} \, D_{vg} \, \rho_g \ln(1 + B_M), \tag{3.23}$$

where Sh is the Sherwood number, a dimensionless number which represents the ratio of convective to diffusive mass transport. R_l, D_{vg} and ρ_g are respectively the droplet radius, the vapor diffusivity in the mixture and the density of the gaseous mixture. $B_M = \frac{Y_{v,surf} - Y_{v,\infty}}{1 - Y_{v,surf}}$ is the mass Spalding number. This number is calculated from:

$$Y_{v,surf} = \frac{M_v X_{v,surf}}{M_v X_{v,surf} + (1 - X_{v,surf}) M_\infty}, \tag{3.24}$$

where

$$X_{v,surf} = X_l \frac{p_{v,sat}(T_l)}{p_\infty} \overset{\text{here}}{=} \frac{p_{v,sat}(T_l)}{p^\circ}. \tag{3.25}$$

The vapor pressure, $p_{v,sat}$ is derived from the Clausius–Clapeyron relation. For ethylene glycol [137], the semi-empirical Antoine extended equation reads:

$$p_{v,sat(T_l)} = \exp\left(84.09 - \frac{10411}{T_l} - 8.1976 \ln T_l + 1.6536 \cdot 10^{-18} T_l^6\right), \quad p \text{ in Pa}, T_l \in [260.15; 720] \text{ K}. \tag{3.26}$$

The Sherwood number has to be expressed by an empirical correlation. The most common Frössling correlation [138] is used:

$$\mathrm{Sh} = 2 + 0.552\ \mathrm{Re}^{1/2}\mathrm{Sc}^{1/3}. \tag{3.27}$$

The thermophysical parameters of the gas film have to be evaluated. This is done by choosing a reference temperature. The literature suggests adopting the 1/3-rule [139, 140]:

$$T_{ref} = T_{surf} + 1/3\left(T_\infty - T_{surf}\right). \tag{3.28}$$

With this evaporation model, we can now derive the transfer terms for two of the governing equations, the continuity equation (equation 3.13) and the species transport equation (equation 3.16). The transfer terms for the continuity equation can be rewritten from the expression of the mass evaporating rate and the volume of one liquid droplet:

$$\widehat{\Gamma}_g = -\widehat{\Gamma}_l = \frac{\alpha_l}{V_l}\dot{m}_l = \frac{3}{2}\frac{\alpha_l}{R_l^2}\,\mathrm{Sh}\,D_{vg}\,\rho_g \ln(1 + B_M). \tag{3.29}$$

The solution for the species mass transfer rate is straightforward for a single liquid component. For the liquid phase, no transport equation has to be solved since $Y_{EtGly,l} = 1$. For the gas phase, we have

$$\widehat{\Gamma}_{ig} = \begin{cases} 0 \text{ if } i \neq \text{Ethylene glycol}, \\ \widehat{\Gamma}_g \text{ otherwise.} \end{cases} \tag{3.30}$$

We will define the heat exchange in a very similar way. A dispersed particle receives heat according to $h_c A_l \Delta T$, with h_c the heat transfer coefficient and A_l the surface of the particle. One contribution of the energy transfer between the

two phases can then be written:

$$\widehat{E}_{l,h} = -\widehat{E}_{g,h} = \frac{\alpha_l}{V_l} h_c A_l (T_g - T_l). \tag{3.31}$$

The coefficient h_c is determined via the Nusselt number Nu for a droplet

$$h_c = \frac{\mathrm{Nu}\lambda_g}{2R_l}, \tag{3.32}$$

and thus

$$\widehat{E}_{l,h} = \frac{3}{2}\frac{\alpha_l}{R_l^2}\mathrm{Nu}\ \lambda_g (T_g - T_l). \tag{3.33}$$

λ_g is the thermal conductivity of the gas and the corresponding Ranz-Marshall correlation [141] for Nu, depending on the Reynolds and the Prandtl number Pr, is used:

$$\mathrm{Nu} = 2 + 0.6\ \mathrm{Re}^{1/2}\mathrm{Pr}^{1/3}. \tag{3.34}$$

The vaporization induces several new energy and momentum transfers, namely momentum transfer due to mass transfer, kinetic energy transfer due to mass transfer and heat of vaporization:

$$\widehat{\mathbf{M}}_{g,v} = -\widehat{\mathbf{M}}_{l,v} = \frac{\alpha_l}{V_l}\dot{m}_l \hat{\mathbf{v}}_l, \tag{3.35}$$

$$\widehat{E}_{g,k} = -\widehat{E}_{l,k} = \frac{\alpha_l}{V_l}\dot{m}_l k_l, \tag{3.36}$$

$$\widehat{E}_{g,v} = -\widehat{E}_{l,v} = \frac{\alpha_l}{V_l}\dot{m}_l L_{vap}. \tag{3.37}$$

3.2.2 Momentum transfer

A term of the momentum transfers has been mentioned above. However, the main contributions arise from forces exerting between phases. The development follows the one conducted for evaporation. We look only at the forces acting on one preferential phase, the liquid phase. A difference, however, is that the balance is done on instantaneous forces and the averaging to obtain the averaged interphase momentum transfer will result in additional terms, most notably the turbulent drag term.

$$\widehat{\mathbf{M}}_{l,F} = \frac{\alpha_l}{V_l}\sum \widehat{\mathbf{F}}_l \tag{3.38}$$

The instantaneous forces $\mathbf{F}_l$ acting on suspended particles may have several contributions, such as the drag force, the lift force, the virtual mass force or the basset force. The drag force arises from a relative (slip) velocity between particle and an underlying flow. It is a resisting force that is directed opposite to the relative motion. The perpendicular shear-induced force to drag acting on a body is called lift force. The virtual mass force corresponds to the inertia of the continuous phase coming from the acceleration of particles. The Basset force also arises from the acceleration of particles, but is commonly neglected in most practical calculations. Because the dispersed phase density is, in our case, several orders of magnitude larger than the one of the continuous phase, the virtual mass effect can also be neglected. The lift force is usually insignificant compared to the drag force, especially for small particles. It can become significant when phases separate, which is not the case here.

Thus, only the drag force is retained for the instantaneous forces acting on the liquid droplets. This force is commonly written:

$$\mathbf{F}_{l,d} = \frac{1}{2}\rho_g C_d A_l v_r \mathbf{v}_r, \tag{3.39}$$

where $\mathbf{v}_r = \mathbf{v}_g - \mathbf{v}_l$ is the relative velocity and C_d is the drag coefficient. The common drag model of Schiller and Naumann [142] is chosen:

$$C_d = \frac{24}{\mathrm{Re}}\left(1 + 0.15\,\mathrm{Re}^{0.687}\right). \tag{3.40}$$

The instantaneous drag force is expressed in function of the instantaneous velocities. We simplify the formulation of the drag force into:

$$\mathbf{F}_{l,d} = A_d\left(\mathbf{v}_g - \mathbf{v}_l\right). \tag{3.41}$$

To obtain the averaged interphase momentum transfer, we need an expression of the averaged force $\widehat{\mathbf{F}}_{l,d}$. Droplets' motion is imposed by the continuous gas phase velocities, which includes the turbulent eddies. The turbulence of the gas phase has a direct effect on the dispersed phase, as it tends to transport the particles from regions of high concentration to regions of lower concentration. This phenomenon is captured when we average the force [143]

$$\widehat{\mathbf{F}}_{l,d} = \widehat{A_d}\left(\hat{\mathbf{v}}_g - \hat{\mathbf{v}}_l\right) + \widehat{A_d\left(\mathbf{v}_g'' - \mathbf{v}_l''\right)}. \tag{3.42}$$

The left term on the right-hand side is the mean drag force, while the right

term is referred as the turbulent dispersion force. This last term is modeled. In the present work, the Burns model [144] is used. With C_{td} a model constant, it reads:

$$\widehat{\mathbf{F}}_{l,d} = \widehat{A_d}\left(\widehat{\mathbf{v}}_g - \widehat{\mathbf{v}}_l\right) + A_d C_{td}\frac{\mu_{t,g}}{\rho_g \mathrm{Pr}_t}\left(\frac{\nabla \alpha_g}{\alpha_g} - \frac{\nabla \alpha_l}{\alpha_l}\right). \tag{3.43}$$

3.2.3 Validation case

A validation case is presented in this section. Several objectives are foreseen. First, we will verify that the solver ensures mass continuity with respect to each phase. Many criteria could provoke discrepancies, that it is at the mass transfer terms, the volume fraction calculation or the pressure-velocity coupling. As the density ratio is particularly important, a small deviation may result in the fuel in the gas phase being greatly over- or underestimated. The simulation will also be compared with a Lagrangian based approach. OpenFOAM already provides solvers performing Discrete Particle Simulation. By confronting the Eulerian based solver to a native one, we will be able to test the validity of the developed evaporation model, and also of the momentum treatment. The test case is not meant to address a physical treatment of a spray, but to reduce the complexity to allow a better comparison between the two approaches.

Liquid droplets of ethylene glycol are injected downstream from a circular inlet with a radius of 3.3 mm into a cylinder. Top and sides consist of walls, while the bottom is left open. Droplets are taken monodisperse with a diameter of 70 μm. Only the liquid is injected; the gas is homogeneous at the initial conditions with a temperature of 1,200 °C and consists only of nitrogen. Chemistry is not included. We inject the droplets at 300 K for a duration of 2 ms with a mass flow rate of 10^{-4} kg/s. The mass injected during this time span is written $m_l^{\mathcal{I}}$.

3 simulations are performed, an Eulerian-Eulerian simulation on a 2D grid, one on a 3D grid and an Eulerian-Lagrangian simulation on the same 3D grid. The simulations are denoted EE 2D, EE 3D and EL 3D. Sketches of the meshes can be seen in Figure 3.1. Structured grids are used. The discretization along the cylinder is the same. Along the radius, the 2D grid discretization is close to the 3D grid, but not totally equivalent since the 3D grid is not axisymmetric. The Lagrangian simulation could not be performed on the 2D grid because of parcels crossing the wedges.

The Lagrangian solver used gives an output at each time step of the mass of liquid present in the domain, $m_l\,(t)$, and the total mass evaporated. A derivation of this last data gives the mass evaporation rate, $\dot{m}_l$. Concerning the EE solver,

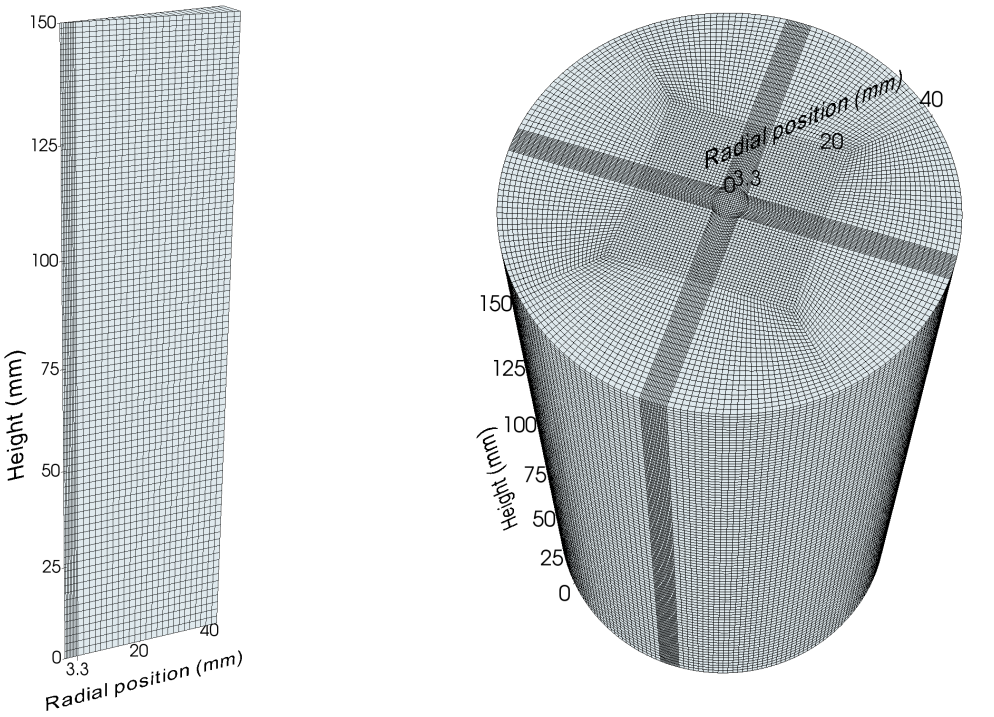

A) 2D grid: 3,400 cells

B) 3D grid: 1,142,400 cells

FIGURE 3.1: CFD grids used for the Eulerian-Eulerian validation case

the mass of liquid is not directly available. However, the phase volume fraction and the densities are known in every cell. It is possible to extract the mass of liquid by summing the contributions over all cells:

$$m_p(t) = \sum_A \alpha_{p,A} \rho_{p,A} V_A, \quad p = l \text{ or } g. \tag{3.44}$$

Similarly, the total evaporation rate can be derived by summing $\dot{m}_{l,A}$ over the domain. These two outputs of the liquid phase are displayed in Figure 3.2a for the three simulations. The total mass of liquid in the domain increases for the duration of the liquid injection. In the absence of evaporation, the blue curves would reach 1 at 2 ms and then stay constant. In the present plot, they are slightly below due to a beginning of evaporation. The evaporation rate is displayed in red. No evaporation takes place initially. It starts when some of the liquid has reached a sufficient temperature. This phase of liquid injection, liquid's heat up and beginning of evaporation is exactly retrieved with all simulations. It comforts our modeling of heat exchange and evaporation. The evaporation

rate reaches a maximum when all the liquid has reached the boiling temperature, and decreases further as the quantity of liquid decreases. All three simulations are very close to each other, particularly between the two EE simulations. Most of the discrepancies can be attributed to the grids not being one to one equivalent. The Eulerian-Eulerian offers a natural transition from 3D to a 2D transcription.

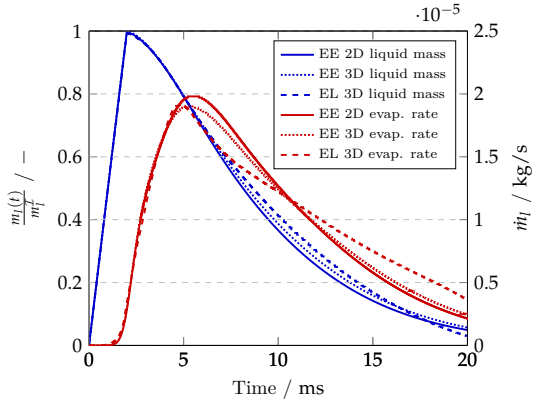

A) Results of the liquid evolution for EE 2D, EE 3D and EL 3D are compared. Blue curves indicate the normalized mass of liquid in the domain. This mass increases for the duration of liquid injection (2 ms), then it decreases accordingly with the mass evaporation rates (red curves).

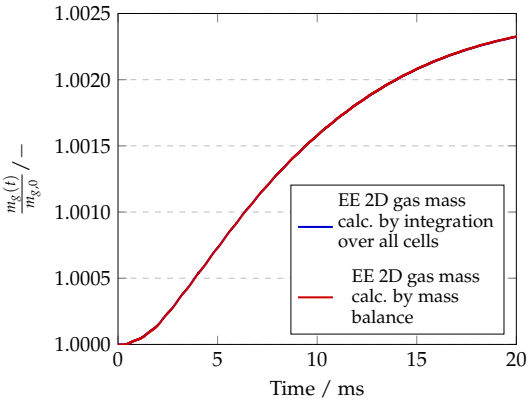

B) Verification of the gas phase continuity for EE 2D. The total mass of gas contained in the domain obtained by integration over the volume (equation 3.39, blue curve) overlaps perfectly the mass calculated by mass balance (equation 3.40, red curve) during the whole simulation.

FIGURE 3.2: Liquid (left) and gas (right) evolution of the Eulerian-Eulerian validation test case

The purpose of the Figure 3.2b is to verify that the liquid evaporation drives the right changes on the gas phase, only EE 2D is considered. To this end, two elements are compared. First, the mass of the gas phase can be computed using equation 3.44 at each time step. It corresponds to the mass being effectively present in the domain at a time t. Additionally, we can calculate the expected gas mass evolution taking into account the evaporation and the gas entering/leaving the domain. This mass balance is given by the equation 3.45. The second term of the integral is the gas flux at the outlet. The mass of the gas phase can be calculated at every single time step starting from the initial mass. As Figure 3.2b demonstrates, the conservation is respected over the whole simulation time.

$$m_g\left(t+\Delta t\right) = m_g\left(t\right) + \int_t^{t+\Delta t} \left(\dot{m}_l - \sum_{f\in\mathcal{O}} \alpha_{g,F}\rho_{g,F}\mathbf{v}_{g,F}\cdot\mathbf{S}_f \right) dt \tag{3.45}$$

The last figure for this validation case is shown in Figure 3.3. Two results are given, the mass fraction of ethylene glycol and the gas temperature field along the center axis. This is meant to show that the results not only agree on a domain level, but also spatially. The results are given at two distinct times; the spatial evolution is very similar. It requires both, the right evaporation model the right and momentum treatment. The momentum treatment comprises the resolution of Newton's law for EL and the resolution of momentum/pressure equations for EE with corresponding gravitation and drag force.

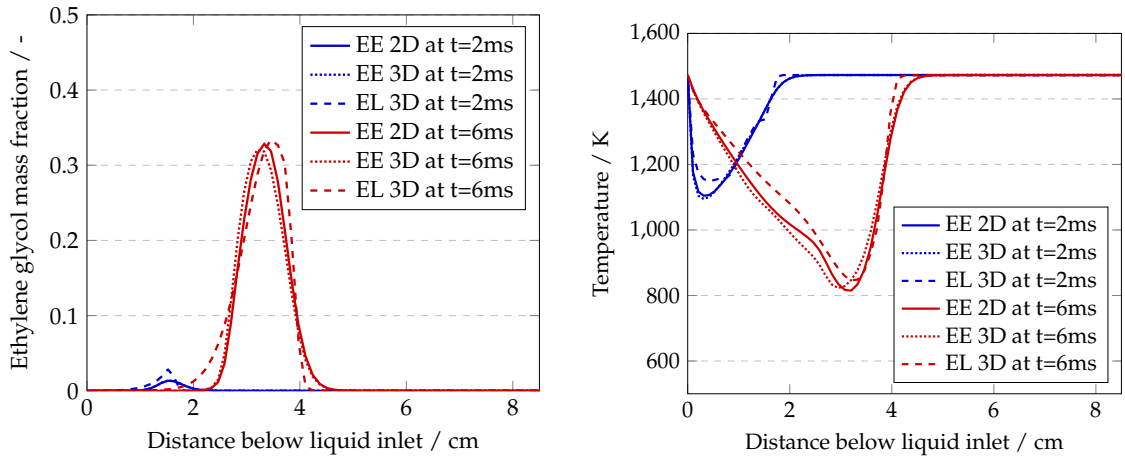

A) Ethylene glycol mass fraction vs. distance

B) Temperature vs. distance

FIGURE 3.3: Comparison along the axis between the three simulations, EE 2D, EE 3D, and EL 3D, of the validation test case at two distinct times, 2 ms and 6 ms. At 2 ms, the curves of EE 2D and EE 3D for both results (temperature and EG mass fraction) overlap almost perfectly.

Chapter 4

The sectional approach for char gasification

This chapter is dedicated to the development of a model that will allow the description of the char conversion in an entrained-flow gasifier. The traditional approach that consists in treating particles individually with numerical points is abandoned. Instead, virtual species are created, following the so-called sectional approach. Transport equations on these species allow capturing the solid conversion. A reliable model is obtained by creating adequate pseudo-species that respect the particle size distribution, composition and evolution. It also includes a complete mechanism with the establishment of reactions, the determination of reaction rates and also thermodynamic data. Finally, the Eulerian-Eulerian model presented in the previous Chapter is extended to account for the solid transfer from the liquid phase to the gas phase. The following section is in part taken from Fradet et al. [145].

4.1 Concept of the sectional approach

The concept of the sectional approach, or discrete approach, consists of dividing the mass range of interest into a certain number of classes, N_c. These classes are also denoted as BIN classes or BINs. The geometric constraint of Gelbard et al. [146] requires a scaling factor superior or equal to 2 between two successive classes. As commonly used [147–150], a scaling factor of 2 has been chosen in this work.

Originally developed for aerosol description, this method has been applied to soot modeling by Pope and Howard [147] and has later been widely reused [151–153]. This model has more recently found application in the CFD field [148, 149, 154–156]. Computationally less expensive than very detailed

soot modeling [157, 158], the sectional approach provides a good accuracy. Di Domenico [154] used for the first time the sectional approach for the CFD simulation of soot formation in gas turbine combustors. This approach was nevertheless restricted to the description of the Polycyclic Aromatic Hydrocarbons (PAHs), or soot precursors. A simpler two-equation model was employed for the soot particle dynamics. Blacha et al. [148] expanded the sectional approach for PAHs and soot species. The field of application was the simulation of laminar flames, and a good prediction of soot volume fractions for a variety of fuels were achieved. Thanks to the increase of computational capabilities during recent years, the state of the art includes large eddy simulations of sooting turbulent jet flames with a sectional approach [156] for both PAH (3 classes) and soot (24 classes).

In the present work, an attempt to apply the sectional approach in the case of char gasification is made for the first time. The objective is to develop a modeling concept of slurry fuel gasification and its implementation in CFD simulations of the entrained-flow gasifiers, including REGA.

4.2 Model construction

4.2.1 Particle size distribution

In the following, the analysis of the char obtained from straw pyrolysis that has been conducted by Fleck et al. [159] will be used as a support for the presentation of the modeling. However, the reasoning that is conducted can be achieved with any source of biomass based char. The resulting model parameters for the straw char are summed up in Appendix B, along with the char obtained from wood pyrolysis.

In Fleck et al. [159], the median value of the volume size distribution has been determined to be $D_{50} = 22.3\ \mu$m. This number divides the particles population in two equal parts with respect to the volume. Data have been delivered by KIT [160], which show the solid particle size distributions. The data showed that the particle size distributions follow a log-normal distribution. The volume distribution function $n_3(D_s)$ can be expressed [161] as:

$$n_3(D_s) = \frac{1}{\sqrt{2\pi} D_s \ln \sigma_g} \exp\left[-\frac{1}{2} \left(\frac{\ln(D_s/D_{50})}{\ln \sigma_g} \right)^2 \right]. \tag{4.1}$$

σ_g, the geometric standard deviation, is defined as the ratio D_{84} over D_{50}. Similarly to D_{50}, D_{84} is the diameter for which the cumulative volume of the particles with diameter smaller than D_{84} accounts for 84 % of the total volume. One data set [160] shows a median number of $D_{50} = 22.33$ μm, in agreement with the value in Fleck et al. [159]. D_{84} has been determined with this data set to have a value of 40 μm. The corresponding curve for n_3, as a function of the diameter, is shown in Figure 4.1a, as well as the cumulative function N_3.

4.2.2 Discretization

In the sectional approach, each BIN class is defined through a lower and an upper molar weight, with a ratio or scaling factor of 2 between both values. Therefore, the variable of interest is the molar weight. By assuming the particle density independent of its size, the mass distribution function is the same as the volume distribution function. Since the functions have been normalized, the mass distribution function $\mathcal{M}$, according to the molar weight variable μ_x, can be written as:

$$\mathcal{M}(\mu_x) = \frac{dN_3}{d\mu_x} = \frac{dN_3}{dD_s}\frac{dD_s}{d\mu_x} = n_3\frac{dD_s}{d\mu_x}, \tag{4.2}$$

$$\mathcal{M}(\mu_x) = \frac{1}{\sqrt{2\pi}\ln\sigma_g 3\mu_x}\exp\left[-\frac{1}{2}\left(\frac{\frac{1}{3}\ln\left(\frac{6\mu_x}{\rho N_A \pi}\right)-\ln(D_{50})}{\ln\sigma_g}\right)^2\right]. \tag{4.3}$$

The corresponding curves for the mass distribution function and the cumulative function are displayed in Figure 4.1c.

Discrete classes must be created, based on this continuous mass distribution. That means bounds must be chosen, to limit the number of classes. The lower limit of the first class is defined as the point where $N_3 = 0.01$. Thus, the first class consists of the particles whose molar weight is in the interval $[1.11 \cdot 10^{14} - 2.22 \cdot 10^{14}]$ g/mol, the second class $[2.22 \cdot 10^{14} - 4.44 \cdot 10^{14}]$ g/mol, and so on. The total number of classes, N_c, is defined as the smallest integer that reaches $N_3\left(M^{min}_{\mathrm{BIN}1} \cdot 2^{N_c}\right) > 0.99$. It gives the 12^{th} and last class defined within the bounds $M^{min}_{\mathrm{BIN}12} = 2.27 \cdot 10^{17}$ g/mol and $M^{max}_{\mathrm{BIN}12} = 4.54 \cdot 10^{17}$ g/mol. The mass fraction contained in each of the classes follows:

$$Y_c = \int_{M^{min}_{\mathrm{BIN}_c}}^{M^{max}_{\mathrm{BIN}_c}} \mathcal{M}(\mu_x)d\mu_x. \tag{4.4}$$

These values are then normalized to enclose all the mass; they are displayed in Figure 4.1b.

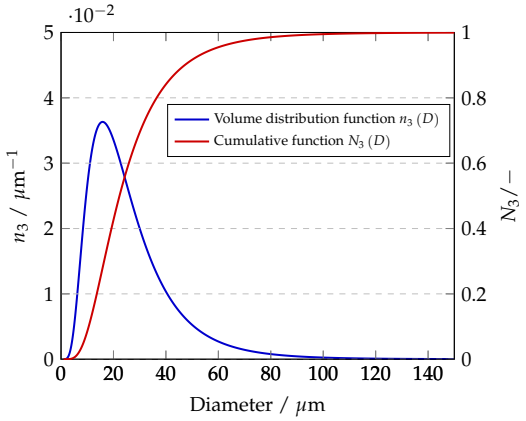

A) Volume distribution function as well as the cumulative function versus the particle diameter

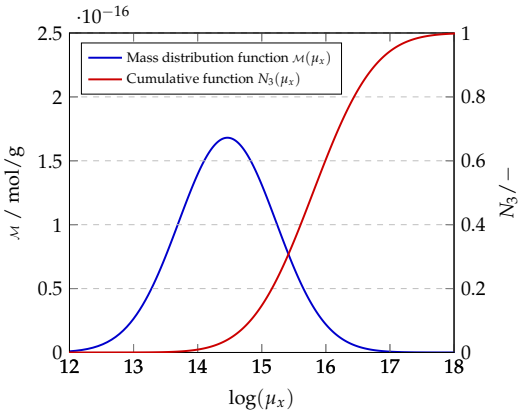

C) Mass distribution function and cumulative function versus the logarithm of molar weight

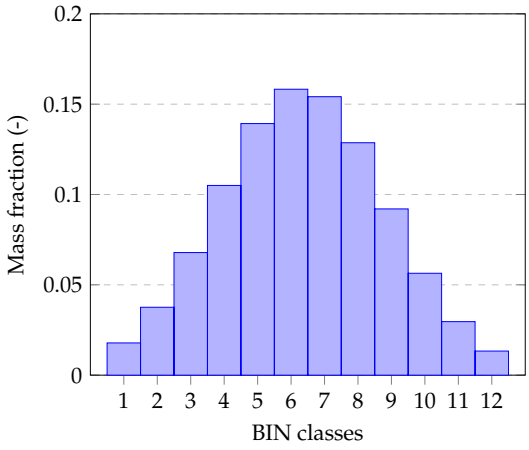

B) Mass fraction that accounts each of the 12 BIN-classes

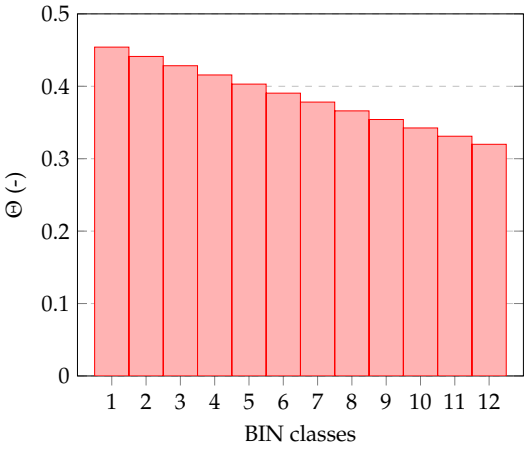

D) Ratio representative of the intra-class distribution

FIGURE 4.1: Successive steps of the classes creation. The volume distribution is derived from experimental analysis, then a variable change is performed. Finally discrete classes are obtained with information on their relative weight and the intra-class distribution.

In the sectional approach for the soot modeling, one assumption must be made concerning the intra-class distribution. There exist several possibilities. For example, the number distribution as a function of the molar weight, defined as $\mathcal{N}(\mu_x) = \frac{\mathcal{M}(\mu_x)}{\mu_x}$, can be considered constant within a class, then $\mathcal{M}(\mu_x) = const. \cdot \mu_x$. Or the mass distribution is constant and $\mathcal{N}(\mu_x) = \frac{const.}{\mu_x}$. In the current case, these distributions are perfectly known through equation 4.3. This is a real asset for the accuracy of the modeling because it allows the determination of the

mean molar weight of each class:

$$M_c^{mean} = \frac{\int_{M_{\mathrm{BIN}_c}^{min}}^{M_{\mathrm{BIN}_c}^{max}} \mathcal{M}(\mu_x) d\mu_x}{\int_{M_{\mathrm{BIN}_c}^{min}}^{M_{\mathrm{BIN}_c}^{max}} \mathcal{N}(\mu_x) d\mu_x}. \tag{4.5}$$

The ratio $\Theta = \frac{M_{\mathrm{BIN}_c}^{mean} - M_{\mathrm{BIN}_c}^{min}}{M_{\mathrm{BIN}_c}^{max} - M_{\mathrm{BIN}_c}^{min}}$ is representative of the c^{th} intra-class distribution. This ratio is represented for each class in Figure 4.1d. A value of 0.5 corresponds to a constant number distribution within a class, while a value of $1/ln(2) - 1 \simeq 0.44$ corresponds to a constant mass distribution. As it can be seen, the first classes are close to the case of a constant mass distribution. Then, the ratio drops below 0.4. This indicates that the number density of particles decreases quickly within each class.

The successive steps presented so far have allowed describing the experimental straw char particles distribution with a sectional approach based on the knowledge of D_{50} and D_{84} only, no further assumptions needed.

4.3 Reactions

4.3.1 Equations

A two-step scheme, from char to secondary char to ash (see Figure 4.2) has been chosen to represent the evolution of the char inside the reactor. This is in agreement with the model used at the KIT facility [58], where early CFD simulations of slurry-fed entrained flow gasifier at 40 bar were performed in order to identify the conversion paths of typical droplets. This was further detailed by Kolb et al. [46].

After the evaporation of the liquid, the char particles enter the gas phase and lose mass, because of their thermal degradation. This step, also denoted secondary pyrolysis because it corresponds to the pyrolysis of char originating from the pyrolysis of biomass, is fast and endothermic. This mass loss will be defined as the volatile part of the char. It also includes the moisture of the char. The second part of the scheme concerns the gasification of the secondary char. Carbon dioxide, as well as steam, will react through heterogeneous reactions with char [162] to form carbon monoxide and hydrogen. The non-reacting part of the particles, ash, is obtained once the gasification is complete. The objective

of this section is to choose appropriate species definitions for the secondary char and ash, as well as to find the stoichiometric coefficients and kinetic rates for the reactions linking these species.

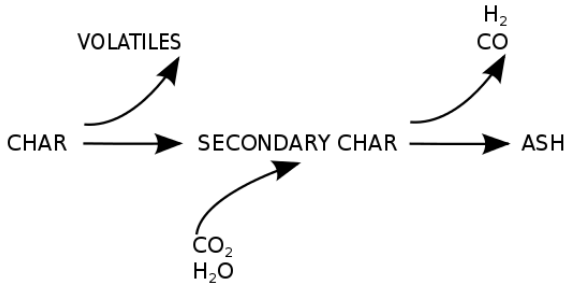

FIGURE 4.2: Global char reaction scheme

Ultimate analysis and proximate analysis of the char have been reported in [159] and are listed in the table of Appendix B (Table B.1). The proximate analysis provides the average composition of the primary char, in terms of fixed carbon, volatiles, moisture, and ash. As mentioned earlier, moisture is considered as part of the volatiles in the model. It is assumed that each particle of straw char has originally the same composition given by the proximate analysis. It means that two other groups of BIN classes can be created in relation to the first group, such that:

$$M^{min/max}_{\mathrm{BIN}_c^{2^{nd}char}} = M^{min/max}_{\mathrm{BIN}_c^{1^{st}char}} \cdot \left(Y_{C_{fix}} + Y_{ash}\right) \tag{4.6}$$

and

$$M^{min/max}_{\mathrm{BIN}_c^{ash}} = M^{min/max}_{\mathrm{BIN}_c^{1^{st}char}} \cdot Y_{ash}. \tag{4.7}$$

Experiments have been conducted at KIT [163] to determine the reaction kinetics of the secondary pyrolysis and of the gasification of the secondary char with CO_2. With regard to the secondary pyrolysis, char originating from the fast pyrolysis of barkless soft wood has been injected into a drop-tube reactor, called VERA. This feedstock was injected with varying temperature into the reactor, ranging from 1,073 to 1,873 K and the residence time was kept constant at 200 ms. The elemental composition of the secondary char obtained shows a completion of the secondary pyrolysis reaction at 1,473 K and above. Beyond this temperature, the char is composed almost totally of pure carbon and ash. Since the temperature of the REGA reactor is above 1,473 K, the secondary char composition is chosen to be pure carbon and ash, as reported in Table B.1. The proximate analysis (ash free) can also be seen. Now, with the

knowledge of the proximate analysis of the straw char and the chemical composition of both the straw char and the secondary char, the calculation of the volatile composition through mass and elemental balances can be achieved. The results obtained are reported in Table B.1 in terms of mass and mole percentage. The knowledge of the volatiles average composition offers the possibility to define a set of representative species. The following species have been chosen: Vol $= \{CO; 2\ CH_4; 4\ H_2O; 7\ H_2\}$. This set of species is later used in the reaction mechanism of char pyrolysis presented below.

4.3.2 Associated kinetic rates

In summary, in the paragraphs above, discrete classes for the primary char, the secondary char, and ash have been created and the volatiles content has been characterized. Now, the next step consists in determining the reactions linking the species and the corresponding stoichiometric coefficients. The reaction for a particle that belongs to the c^{th} class of the primary char group can be written as:

$$\mathrm{BIN}_c^{1^{st}char} \longrightarrow \nu_1 \mathrm{BIN}_c^{2^{nd}char} + \nu_2 \mathrm{Vol}. \tag{4.8}$$

The assumption that each particle of one class from the primary char gives one particle of the corresponding class of the secondary char allows one to set $c_1 = 1$, and the mass balance of the secondary pyrolysis reaction leads:

$$\nu_2 = \frac{M^{mean}_{\mathrm{BIN}_c^{1^{st}char}} - M^{mean}_{\mathrm{BIN}_c^{2^{nd}char}}}{M_{\mathrm{Vol}}}. \tag{4.9}$$

Unfortunately, the experiments that have been carried out [163] do not offer kinetic rates for the secondary pyrolysis of primary char; only equilibrium data have been obtained. The information available is that the reaction is completed in less than 200 ms. For a first order kinetic rate, and assuming an Arrhenius-like reaction law, the half-life of reaction is given by:

$$t_{1/2}^{Pyr} = \frac{2}{A_r^{Pyr} \exp\left(-\dfrac{E_a}{RT}\right)}. \tag{4.10}$$

The reference kinetic parameters are derived for the 6^{th} class, as it is the preponderant class. The pre-exponential factor A_r and the activation energy E_a are taken so that the half-life of the pyrolysis reaction of this class is equal to

20 ms at 1,200 °C. An activation energy of 50,000 J/mol is chosen, resulting in $A_{r,6}^{Pyr} = 5,202.5\ \mathrm{s}^{-1}$. With this pair, the half-life increases to 106 ms at 900 °C and decreases to 7.5 ms at 1,500 °C. The motivation to choose this value for E_a is that the reaction becomes too slow to occur below 900 °C and in the meantime, for higher temperature, the reaction rate does not increase too quickly to account for the physical limitations of a devolatilization process.

For the kinetic parameters of the other classes, two effects are accounted for. On the one hand, for a constant reaction rate, the time needed to convert one particle is proportional to its mass. It means, the half-life is increased by a factor of about 2 between two successive classes. On the other hand, we should also consider the increase in the surface in contact with the hot surrounding gas. Assuming spherical particles, the surface ratio of two particles having a mass ratio of 2 (or volume ratio, considering a constant density) is 1.59, leading to an equivalent decrease in the reaction half-life. Now, taking both effects into consideration, the half-life of the class $c+1$ is obtained after:

$$t_{1/2,c+1}^{Pyr} = \frac{M_{\mathrm{BIN}_{c+1}^{1^{st}char}}}{M_{\mathrm{BIN}_{c}^{1^{st}char}}} \frac{S_{\mathrm{BIN}_{c}^{1^{st}char}}}{S_{\mathrm{BIN}_{c+1}^{1^{st}char}}} t_{1/2,c}^{Pyr} \simeq \frac{2}{1.58} t_{1/2,c}^{Pyr} = 1.27 t_{1/2,c}^{Pyr}. \tag{4.11}$$

As first order reactions are considered, this is simply traduced by a change in the pre-exponential factor (see equation 4.10). More generally, the pyrolysis rate parameter of the c^{th} has been calculated from the reference class as:

$$A_{r,c}^{Pyr} = \left(\frac{M_{\mathrm{BIN}_{c}^{1^{st}char}}}{M_{\mathrm{BIN}_{6}^{1^{st}char}}} \right)^{-1/3} A_{r,6}^{Pyr}. \tag{4.12}$$

This results in a half-life comprised between 6 ms for the smallest BIN up to 80 ms for the 12^{th} class at 1,200 °C.

Similarly to the approach used in equation 4.8, the gasification reactions are written as:

$$\mathrm{BIN}_{c}^{2^{nd}char} + \nu_3 \mathrm{CO_2} \longrightarrow \mathrm{BIN}_{c}^{ash} + 2 \cdot \nu_3 \mathrm{CO}, \tag{4.13}$$

$$\mathrm{BIN}_{c}^{2^{nd}char} + \nu_3 \mathrm{H_2O} \longrightarrow \mathrm{BIN}_{c}^{ash} + \nu_3 \mathrm{CO} + \nu_3 \mathrm{H_2}, \tag{4.14}$$

where

$$\nu_3 = \frac{M_{\mathrm{BIN}_{c}^{2^{nd}char}}^{mean} - M_{\mathrm{BIN}_{c}^{ash}}^{mean}}{M_{\mathrm{C}}}. \tag{4.15}$$

Studies on the reactivity of coal char gasification have been extensively documented [87, 164]. However, the literature concerning the gasification of biomass-based char is sparse in comparison. However, Di Blasi [165] gave a review on the state-of-the-art of the gasification of lignocellulosic char including kinetic rates for reactions with carbon dioxide and steam. Most of the studies are based on **T**hermo **G**ravimetric **A**nalysis (**TGA**) or **p**ressurized **TGA** (**pTGA**). A great number of reaction rates are proposed, because of the variety of the feedstock. However, all experiments show that the gasification does not occur below 1,000 K. The activation energies are high, in the range 180-250 kJ/mol. A pTGA and a **F**ree-**F**all **F**ixed-**B**ed (**FFFB**) experiment with carbon dioxide are reported by Schneider et al. [163]. This experiment is particularly useful for the case considered here, because the sample utilized is the secondary char obtained from the experiment in the VERA reactor at 1,873 K. They obtained the following reaction rate:

$$S_r^{pTGA} = A_r^{pTGA} \exp\left(\frac{-E_a^G}{RT}\right) = 5.24 \cdot 10^8 \exp\left(\frac{-236,000}{RT}\right). \tag{4.16}$$

The pre-exponential factor was not explicitly given but was deduced from the Figure 5 of Schneider et al. [163]. The reaction rate of the pTGA analysis is expressed in the form [166]

$$S_r^{pTGA} = \frac{d\chi}{dt}, \tag{4.17}$$

where $\chi = \frac{m_{C_0} - m_C(t)}{m_{C_0}}$ is the carbon conversion degree. This reaction rate can also be expressed through the mass loss rate

$$-\frac{dm_C}{dt} = m_{C_0} A_r^{pTGA} \exp\left(\frac{-E_a^G}{RT}\right). \tag{4.18}$$

However, this particular experiment was performed at 40 bar in the presence of 80 $\%_{vol}$ carbon dioxide and, therefore, could be used directly for the modeling of a high-pressure gasifier. However, in the case of REGA, at atmospheric pressure, the pressure of carbon dioxide and steam is much lower. The literature [165] shows a dependency on the pressure of the oxidant. A value of 0.6 for the order is chosen, according to the experiments of Müller et al [166].

The rate of the gasification reaction is the rate at which all of the carbon of a particle is converted. This can be linked with the rate obtained from the pTGA

via a first order reaction rate:

$$S_r^G = -\frac{d\left[\mathrm{BIN}_i^{2^{nd}char}\right]}{dt} = A_{r,p}^G \exp\left(\frac{-E_a^G}{RT}\right)\left[\mathrm{BIN}_i^{2^{nd}char}\right] p_{ox}^{0.6}. \tag{4.19}$$

In the previous equation, the value of the activation energy has been kept identical to the measured value by the pTGA [163], $E_a^G = -236$ kJ/mol. However, the pre-exponential factor has been modified to take into account the partial pressure of oxidant as it can be found in the gasifier REGA under atmospheric pressure, $A_{r,p}^G = A_r^{pTGA} / (40 \cdot 0.8)^{0.6} = 6.55 \cdot 10^7$ $1/(\mathrm{s} \cdot \mathrm{bar}^{0.6})$. The current application of this reaction rate is expressed with the species concentration. We express S_r^G as a function of the oxidant concentration $[ox]^{0.6}$ rather than of the oxidant partial pressure $p_{ox}^{0.6}$. Therefore, a second change on the pre-exponential factor is made: $A_r^G = A_{r,p}^G \cdot (RT)^{0.6}$. Considering, the numerous modification of the initial experimental reaction rate, only an estimation of this parameter is assumed at this stage.

To sum up, the gasification reaction rate is given by an Arrhenius equation, with an activation energy $E_a^G = -236$ kJ/mol, a partial order of one for the solid concentration, of 0.6 for the oxidant concentration, and a pre-exponential factor of $A_r^G \simeq 10^8 - 10^9$ $1/\mathrm{s}/(\mathrm{mol}/\mathrm{m}^3)^{0.6}$. The sensitivity on this last parameter will be studied in the next chapter.

The reasoning conducted so far has yielded to the description of the char inside slurry droplets and then to the successive steps that each char particle undergoes in the gas phase by means of reaction paths and kinetic rates.

In addition, a few modifications for the case with ethylene glycol containing char particles must be made in the source code of the CFD solver. One transport equation is added for each BIN class created, so $3 \cdot N_c$ for the gas phase according to the three groups of classes: the primary char, the secondary char, and ash. N_c species are also added for the liquid phase concerning the primary char injected with EG. The initial mass fractions for each of the species in the liquid phase are also given as input according to the values of Figure 4.1b. The evaporation is slightly modified to account for the presence of the solid in the liquid. As first mentioned by Lee et al. [167], the liquid evaporation is dependent on the liquid in contact with the surface of the droplet and can be linked with the ethylene glycol volume fraction $\varepsilon_{\mathrm{EG}}^{slurry}$ inside the slurry droplet:

$$\dot{m}_{\mathrm{EG}}^{slurry} = \varepsilon_{\mathrm{EG}}^{slurry} \dot{m}_{\mathrm{EG}}^{pure}. \tag{4.20}$$

The rate of transfer of the primary char from the liquid to the gas phase is deduced from the fact that once a droplet is totally vaporized, all the solid should be part of the gas phase. It has therefore been assumed that the mass transfer of solid from the liquid to the gas phase is proportional to the total mass transfer:

$$\dot{m}_{\mathrm{BIN}_c^{1^{st}char}} = Y_c \cdot Y_{slurry}^{solid} \cdot \dot{m}_{tot}^{slurry} = Y_c \cdot Y_{solid}^{slurry} \cdot \frac{\dot{m}_{\mathrm{EG}}^{slurry}}{Y_{\mathrm{EG}}^{slurry}}, \tag{4.21}$$

where Y_c is the already determined mass fraction of solid in the class c (see Figure 4.1b). Y_{solid}^{slurry} and Y_{EG}^{slurry} are respectively the mass fraction of solid and of ethylene glycol in the slurry droplet. In the end, only few modifications of the two-phase Eulerian CFD-solver are needed to implement the sectional method for char gasification. Most of the work concerns the preprocessing process, creation of pseudo-species, and development of a mechanism with them. Then, the pseudo-species are simply tracked by classical transport equations. What needs to be modified concerns the mass-transfer treatment that is presented above in equations 4.20 and 4.21. For this reason, the current sectional approach for the char gasification could also be coupled to a traditional Lagrangian solver to model a slurry entrained-flow gasification or even solely in the case of solid fuel gasification for example.

4.4 Thermodynamic properties of bio-char

This section aims at establishing thermodynamic properties for the three types of solids derived previously. This includes the determination of the heat capacity, the enthalpy and the entropy; quantities that are dependent on species state and composition. For consistency with the gaseous thermodynamic properties, the results will be expressed in the form of NASA polynomials [168]. These polynomials take the form:

$$\frac{C_p}{R} = a_1 + a_2 T + a_3 T^2 + a_4 T^3 + a_5 T^4, \tag{4.22}$$

$$\frac{H}{RT} = a_1 + \frac{a_2}{2} T + \frac{a_3}{3} T^2 + \frac{a_4}{4} T^3 + \frac{a_5}{5} T^4 + \frac{a_6}{T}, \tag{4.23}$$

$$\frac{S}{R} = a_1 \ln(T) + a_2 T + \frac{a_3}{2} T^2 + \frac{a_4}{3} T^3 + \frac{a_5}{4} T^4 + a_7, \tag{4.24}$$

where $a_1, ..., a_7$ are the numerical coefficients that will be supplied in the thermodynamic file. These functions are therefore only functions of temperature.

To cover more accurately a wide temperature range, two sets of parameters are determined, one for the low temperature range, one for the high temperature range.

4.4.1 Heat capacity

Many correlations have been developed for the specific heat capacity of coal. It was found that the heat capacity usually decreases with carbon content and increases with the moisture and volatile matter content [169]. The correlations are written in order to account for the content in carbon, moisture, and ash, as well as the volatile matter composition. We can cite for example the models of Merrick [170], Kirov [171], van Krevelen [172] or Postrzednik [173]. Because of the similarities between biogenic originating chars and coals, it is assumed that the models can be transposed in our case. The correlation of Merrick is used here. It is based on Einstein's quantum theory specific heat description for solids [174]. The correlation is written:

$$c_p = \frac{R}{M}\left[g_1\left(\frac{380}{T}\right) + 2g_2\left(\frac{1,800}{T}\right)\right], \tag{4.25}$$

where M is the solid average molar mass and the functions g_j follow:

$$g_j\left(\frac{\theta_j}{T}\right) = \frac{\exp\left(\frac{\theta_j}{T}\right)}{\left[\frac{\exp\left(\frac{\theta_j}{T}\right) - 1}{\frac{\theta_j}{T}}\right]^2}. \tag{4.26}$$

In the last equation, θ_j are the Einstein's characteristic temperatures taken equal to 380 K and 1,800 K in the case of coal, according to Merick [170]. Because of how the sectional approach was build, the composition of the primary char is invariant. And thus M is a constant and taking the straw char composition from Fleck et al. [159], it follows:

$$M = \left(\sum_i \frac{Y_i}{M_i}\right)^{-1} = 8.55 \text{ g/mol}, \ i \text{ in C, H, O, N, S.} \tag{4.27}$$

From this correlation, we can determine 2 sets of 5 coefficient $b_1, ..., b_5$, which give the specific heat capacity (i.e. heat capacities per mass). The final coefficients a_i are then obtained for each c^{th} BIN class by simply multiplying b_i by the class molar weight and dividing by the perfect gas constant, $a_{i,\mathrm{BIN}_c^{1^{st}char}} = \frac{M_{\mathrm{BIN}_c^{1^{st}char}}}{R} b_i$.

For the secondary char, its heat capacity is considered close to pure carbon in graphite form, whose correlation was taken from Butland and Maddison [175] with a valid temperature range from 200 K to 3,500 K.

Now, concerning ash, we can derive a correlation with high fidelity, as the detailed composition is given in [159]. Ash is composed by CaO, SiO_2, and K_2O. Correlations for these species taken separately can be found in [176] for CaO and K_2O and in [177] for SiO_2. Then, the specific heat for ash is found by summing each contribution, $c_{p,\mathrm{Ash}} = \sum_i Y_i c_{p,i}$.

These three correlations of the specific heat capacity are displayed in Figure 4.3, as well as the corresponding coefficients $b_1, ..., b_5$.

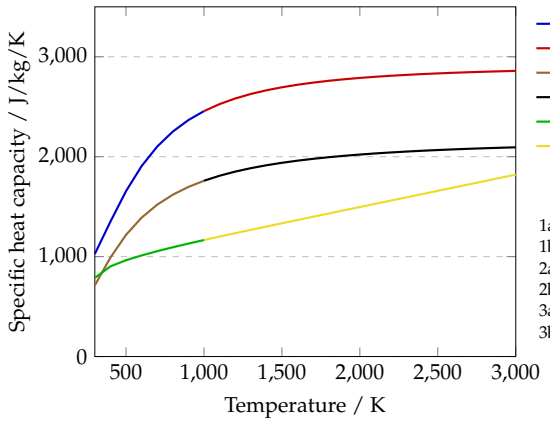

	b_1 $[c_p]$	b_2 $[c_p]/\mathrm{K}$	b_3 $[c_p]/\mathrm{K}^2$	b_4 $[c_p]/\mathrm{K}^3$	b_5 $[c_p]/\mathrm{K}^4$
1a	165.3	1.721	$6.381 \cdot 10^{-3}$	$-9.700 \cdot 10^{-6}$	$3.889 \cdot 10^{-09}$
1b	738.9	3.114	$-1.853 \cdot 10^{-3}$	$5.126 \cdot 10^{-7}$	$-5.419 \cdot 10^{-11}$
2a	−525.8	5.210	$-3.791 \cdot 10^{-3}$	$4.786 \cdot 10^{-7}$	$3.872 \cdot 10^{-10}$
2b	656.6	1.914	$-1.062 \cdot 10^{-3}$	$2.797 \cdot 10^{-7}$	$-2.845 \cdot 10^{-11}$
3a	−132.6	5.385	$-1.020 \cdot 10^{-2}$	$9.182 \cdot 10^{-6}$	$-3.074 \cdot 10^{-09}$
3b	781.9	0.4391	$-7.338 \cdot 10^{-5}$	$2.037 \cdot 10^{-8}$	$-2.074 \cdot 10^{-12}$

FIGURE 4.3: Specific heat capacity of primary char, secondary char and ash. Correlations are extracted for the low temperature range, from 300 to 1,000 K, and for the high temperature range, from 1,000 to 3,000 K. Deduced coefficients $b_1, ..., b_5$ are listed on the right side.

4.4.2 Enthalpy and entropy

The information of the higher heating value given by Fleck et al. [159] will allow the derivation of the formation enthalpy of the primary char. An HHV of 27.3 MJ was measured. It corresponds to the heat released during the combustion of 1 kg

of primary char:

$$1\,\text{kg}\,\text{CHAR}_s + m_{\text{O}_2}\text{O}_{2,g} \longrightarrow m_{\text{CO}_2}\text{CO}_{2,g} + m_{\text{H}_2\text{O}}\text{H}_2\text{O}_l + m_{\text{NO}_2}\text{NO}_{2,g} + m_{\text{SO}_3}\text{SO}_{3,g}. \tag{4.28}$$

By convention, reactants and products of the previous equation are taken in their standard states. Therefore, HHV also corresponds to the opposite of the standard enthalpy of reaction, $\Delta_\text{r}h^\circ = -\text{HHV}$. Now applying the Hess's law on this heat of reaction allows to express it in terms of reactants and products formation enthalpy:

$$\Delta_\text{r}h^\circ = \sum_{product\ i} m_i h^\circ_{\text{f},i} - \sum_{reactant\ i} m_i h^\circ_{\text{f},i}. \tag{4.29}$$

As the standard formation enthalpy of O_2 is null and as by proportionality we can write for example $m_{\text{CO}_2}/M_{\text{CO}_2} = m_\text{C}/M_\text{C}$, equation 4.29 becomes:

$$\Delta_\text{r}h^\circ = \frac{m_\text{C}}{M_\text{C}}H^\circ_{\text{f,CO}_2} + \frac{m_\text{H}}{M_{\text{H}_2}}H^\circ_{\text{f,H}_2\text{O}} + \frac{m_\text{N}}{M_\text{N}}H^\circ_{\text{f,NO}_2} + \frac{m_\text{S}}{M_\text{S}}H^\circ_{\text{f,SO}_3} - \text{kg}\ h^\circ_{\text{f,CHAR}}, \tag{4.30}$$

where m_i, the mass of element i in 1 kg of primary char, is directly obtained from the char proximate analysis. This development yields the standard specific formation enthalpy of the primary char $h^\circ_{\text{f,CHAR}} = -6.361$ MJ/kg. The remaining step is the determination of the coefficient a_6. To this extend, we re-employ the coefficient $b_1, ..., b_5$ and we define a new coefficient b_6 such that:

$$\frac{h}{T} = b_1 + \frac{b_2}{2}T + \frac{b_3}{3}T^2 + \frac{b_4}{4}T^3 + \frac{b_5}{5}T^4 + \frac{b_6}{T}. \tag{4.31}$$

By evaluating the equation 4.31 at the standard conditions, we can isolate b_6. The results are $b_6 = -6.525 \cdot 10^6$ J/kg for the low temperature range and $b_6 = -6.704 \cdot 10^6$ J/kg for the high temperature range. As derived for the heat capacity, the coefficient a_6 is finally calculated for each BIN class by dividing by R and multiplying by the corresponding molar weight.

The reasoning can be shortened in the case of secondary char. Assuming similar properties to graphite, the secondary char formation enthalpy is null, leading for the low and for the high temperatures $b_6 = -4.24 \cdot 10^4$ J/kg and $b_6 = -2.72 \cdot 10^5$ J/kg.

Finally, the standard formation enthalpy of ash is obtained from Hess's law considering that 1 kg of ash is made of CaO, SiO_2 and K_2O in the proportion

given by Fleck et al. [159]:

$$h^{\circ}_{\mathrm{f,ASH}} = \frac{m_{\mathrm{CaO}}}{M_{\mathrm{CaO}}} H^{\circ}_{\mathrm{f,CaO}} + \frac{m_{\mathrm{SiO_2}}}{M_{\mathrm{SiO_2}}} H^{\circ}_{\mathrm{f,SiO_2}} + \frac{m_{\mathrm{K_2O}}}{M_{\mathrm{K_2O}}} H^{\circ}_{\mathrm{f,K_2O}}. \tag{4.32}$$

Then a similar calculation is performed to derive the coefficient b_6. It yields $b_6 = -7.35 \cdot 10^5$ J/kg for $T \in [300 - 1,000]$ K and $b_6 = -8.61 \cdot 10^5$ J/kg for $T \in [1,000 - 3,000]$ K.

Determination of the coefficients related to entropy can be derived in few steps based on the development made with enthalpy. For the primary char, determination of its standard entropy following the methodology used with equation 4.29 is challenging because the standard entropy of reaction also depends on the Gibbs free energy $T\Delta s^{\circ} = -\Delta_{\mathrm{r}} h^{\circ} - \Delta g^{\circ}$, which is unknown. It can however be approximated, stating that the standard entropy mainly depends on the physical state and atoms arrangement. For example, diamond has a standard entropy of 2.4 J/mol$_{\mathrm{C}}$/K, graphite of 5.7 J/mol$_{\mathrm{C}}$/K, while a gaseous species like CO_2 presents a standard entropy of 213.8 J/mol/K. The standard entropy of char is about 10 J/mol$_{\mathrm{C}}$/K according to Eisermann et al. [178]. This value is assumed to be valid for both straw char and wood char. For the secondary char, graphite standard entropy is used and for ash, Hess's law is applied in a similar way as for equation 4.32. Then b_7 is found from the equation

$$s^{\circ} = b_1 \ln\left(T^{\circ}\right) + b_2 T^{\circ} + \frac{b_3}{2} T^{\circ 2} + \frac{b_4}{3} T^{\circ 3} + \frac{b_5}{4} T^{\circ 4} + b_7. \tag{4.33}$$

Standard specific entropies, as well as coefficient b_7 for low and high temperature range, are summed up in Table 4.1. Coefficient a_7 is deduced in the same way as were the coefficients a_1 to a_6.

TABLE 4.1: Standard entropies and coefficient b_7 for low and high temperature range for primary char, secondary char, and ash in the case of straw char

	Primary char	Secondary char	Ash
Standard entropy / J/kg/K	833.3	475.0	760.3
b_7 / J/kg/K, T in [300-1,000] K	-546.3	$1,914$	-160.4
b_7 / J/kg/K, T in [1,000-3,000] K	$-4,309$	$-3,839$	$-3,826$

Chapter 5

Simulation results on the REGA gasifier

5.1 REGA experiments and their numerical representation

Chapter 5 will be dedicated to present simulations and their results of entrained-flow gasification with support of experimental data sets from the gasifier REGA. In total 5 documented data sets are used, two ethylene glycol cases, and three slurry cases. The next section will present in more details these experiments. It will be followed by the presentation of the corresponding numerical setup, as chosen in this work.

5.1.1 Experimental setup

Experiments were carried out in the atmospheric pilot scale entrained-flow gasifier REGA (Research Entrained flow GAsifier). The main features of the reactor have been described in the introduction (section 1.3.1). All documented data sets are summed up in Table 5.1. The first published results are from Fleck et al. [159] in 2015, with the data sets glycol and GSKS10. However, these data sets are not completely consistent. As reported in Fleck et al. [97] in 2018, the global mass balancing of the reactor shows additional quantities of air as compared to the gasification medium solely. It leads to a supplementary amount denoted infiltration air, as indicated for the data set REGA-glycol-T1 for example. For this last data set alone, nitrogen purge has also been reported. Infiltration air is not negligible, as it changes the oxygen/fuel content by about 10 %. These data being undetermined for the experimental sets of 2015, simulation does not agree very well. They are still reported in Table 5.1 because GSKS10 provides a data set

with straw as char, and so, the influence of the type of char can be investigated with comparison to REGA-slurry1-T2, which utilizes wood char. REGA-glycol-T2 is another pure ethylene glycol data set. Glycol and REGA-glycol-T2 are very similar with GSKS10 and REGA-slurry1-T2 in terms of gas and fuel mass flow rates, which facilitates the analysis of the addition of char in the fuel. A last data set, recently available [102], is given with 30 % of wood char.

A simplification is made concerning the infiltration air. It is, in the simulations, simply added to the inlet gas flow rate. Finally, KIT has employed several nozzles to adapt with the various level of gas flow rates. The nozzles have either a parallel or an angled gas outlet, more details are given in the next section.

TABLE 5.1: Experimental data sets of REGA and their operating conditions

	REGA--glycol-T1 [97]	Glycol [159]	GSKS10 [159]	REGA--glycol-T2 [100]	REGA--slurry1-T2 [100]	REGA--slurry2-T2 [102]
Fuel	EG	EG	EG & Straw	EG	EG & Wood	EG & Wood
MFR of fuel $[\mathrm{kg/h}]$	12.56	12.4	12.5	12.42	12.45	12.76
Char content $[\%_{mass}]$	0	0	10	0	10	30
MFR of oxygen $[\mathrm{kg/h}]$	9.67	7.41	7.65	7.56	8.00	8.46
Gasification medium	9.22	7.41	7.65	8.42	7.84	8.33
Infiltration air	0.45	-	-	0.14	0.16	0.13
MFR of nitrogen $[\mathrm{kg/h}]$	9.06	2.86	2.93	3.34	3.34	2.59
Gasification medium	6.94	2.86	2.93	2.89	2.81	2.09
Infiltration air	1.48	-	-	0.45	0.53	0.50
Nitrogen purge	0.64	-	-	0	0	0
Gas-To-Fuel ratio $[-]$	1.49	0.83	0.85	0.88	0.91	0.87
Nozzle	Angled	Parallel	Parallel	Parallel	Parallel	Parallel

5.1.2 Numerical setup

The numerical modeling used for the simulations has been presented throughout the thesis. They are summed up here, as well as additional parameters. To maintain consistency between simulations and reduce the sources of results variations, it was tried to keep as many as possible parameters constant (residuals, matrix inversion solvers, mesh, numerical schemes, and so on).

The main framework is the open source toolbox dedicated to continuum mechanics problems OpenFOAM [179]. The version 5.0 has been used, with a solver derived from the native solver reactingTwoPhaseEulerFoam. The theoretical development is based on an Eulerian-Eulerian approach without interface tracking as presented in Chapter 3.

For the gas phase:

- The Reynolds-averaged equations as given in section 3.1 are solved and the SST $k - \omega$ turbulence model is used (see section 2.3.2).
- The PISO algorithm (Algorithm 1) has been utilized for all simulations, with a courant number of 0.4.
- A reduced and optimized mechanism [180] of the full ethylene glycol mechanism [98] is employed.
- Finite Rate Chemistry (section 2.2.2) is used, with PaSR (section 2.4.2) CTI model.
- The P1 radiation model [181] is used to account for radiation.

For the liquid phase and transfers:

- No turbulence model is used for the dispersed phase.
- The phase is non-reacting, single-component for ethylene glycol cases, multi-component for the slurry cases. Only ethylene glycol evaporates, but solid also undergoes a phase change that is proportional to liquid evaporation (equation 4.21).
- The liquid mass transfer is based on the Spalding evaporation rate (equation 3.23) with Frössling correlation (equation 3.27).
- The heat transfer is given by Ranz-Marshall correlation (equation 3.34).
- The momentum transfer has two dependencies, the drag force and the turbulent drag force, given by the Schiller-Naumann correlation and the Burns turbulent dispersion model.

For the solid phase, if appropriate:

- Two types of solids are considered, char from straw biomass and wood. Most of the data used (ultimate and proximate analysis) are listed in [159]. Other data concern the solid size distribution [160] and the reaction rates [163].

- The current model is based on a sectional approach, which divides the solid log-normal distribution into 12 classes. In total, 48 additional transport equations are solved, 12 respectively for the primary char in the liquid phase, the primary char in the gas phase, the secondary char and the remaining ash. For additional details, the reader is referred to section 4.2.
- Mechanism with kinetic rates and thermodynamic data are derived for both solids as explained in sections 4.3 and 4.4.
- The input parameters for both solids are given in Appendix B.

Simulations are performed for the total length of the reactor, the total height difference from the liquid injection point being equal to 3.25 m. Only two meshes are used, according to the two types of nozzles used, as shown in Table 5.1. Both are 2D-asymmetric structured grids with a 5° wedge. Close-ups on the nozzles discretization region are shown in Figure 5.1. The real geometries of the nozzles are also superimposed for comparison. In total, the grid with an angled gas outlet counts 18,038 cells, with an average non-orthogonality (=angle between the center-to-center vectors and the face normal vectors) of 4.0°, and the second grid counts 23,888 cells and an average non-orthogonality of 4.1°.

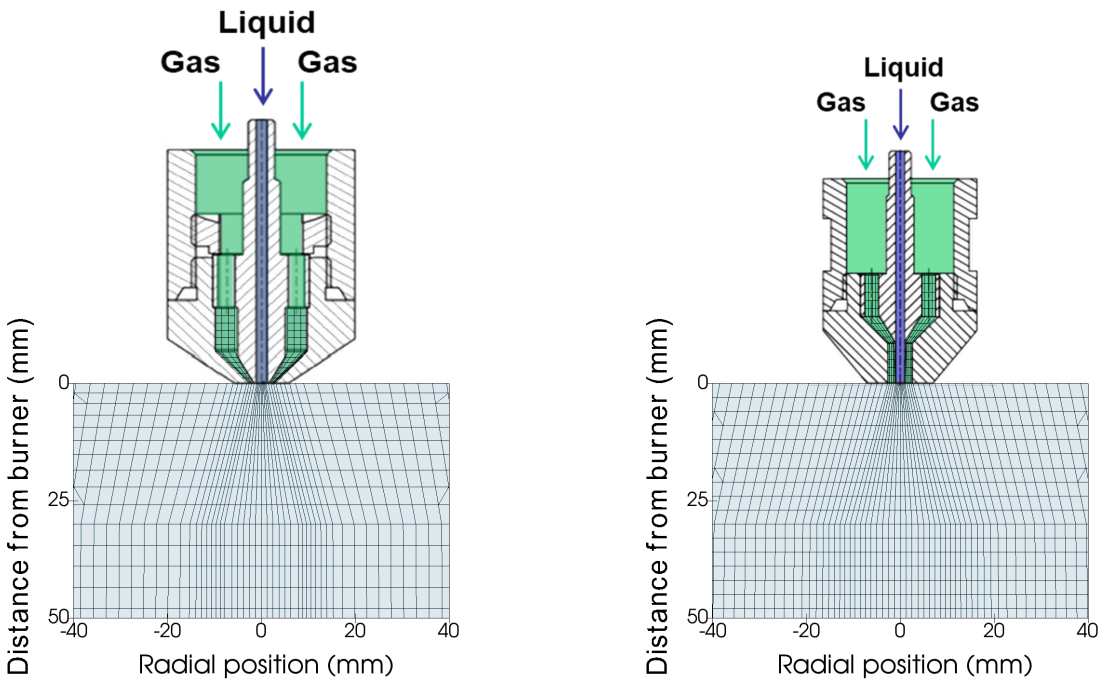

A) Nozzle with angled gas outlet

B) Nozzle with parallel gas outlet

FIGURE 5.1: Zoom on the nozzles region; meshes and nozzles geometry are overlapped

5.2 Gasification of ethylene glycol

5.2.1 REGA-glycol-T1

REGA-glycol-T1 [97] is the most documented of the REGA data sets. Hence, we will examine in more details this data set's simulation results. CFD fields will help us to have a better insight of the gasifier sub-processes. First, attention will be given to the liquid phase (to the spray behavior and to the evaporation properties for example). Then, some of the gas phase data will be analyzed. Finally, a quantitative analysis will be given, by comparing the simulation results with the experimental one (species concentration, temperature).

Simulation fields and results related to the liquid phase are shown in Figure 5.2. A close-up at the spray region is done for better visualization. Figure 5.2a presents the liquid volume fraction, given in a log-scale. The liquid volume fraction α_l equals 1 at the central liquid inlet. Its value then drops quickly along the axis because of the spray angle and the increase of velocity. Indeed, in first approximation (no evaporation, density change), a constant volumetric flow rate in the axis direction (written z) can be assumed. And thus, between two sections we have $\dot{V}_{\mathcal{S}2} = \dot{V}_{\mathcal{S}1}$, leading to $\alpha_{l,\mathcal{S}2} = \dfrac{S_{l,\mathcal{S}1} v^z_{l,\mathcal{S}1}}{S_{l,\mathcal{S}2} v^z_{l,\mathcal{S}2}} \alpha_{l,\mathcal{S}1}$. For example, the liquid inlet radius equals 1 mm and the liquid section occupies 10 mm at 10 cm below the injection point, which means for the area a difference of 2 orders of magnitude. The liquid is injected at 1 m/s, and gains also around 2 orders of magnitude from the gas velocity. Therefore, simply from the liquid dispersion, its volume fraction decreases of several orders of magnitude and a log-scale is necessary for proper representation plotting. What reduces further the liquid volume fraction is the liquid evaporation, whose field is represented in Figure 5.2b. The eccentric injected liquid is evaporating faster than the liquid at the center. This has to be correlated to the gas temperature field, as will be later seen. Ethylene glycol is found to be evaporating slowly in comparison to other fuels, such as ethanol, diesel fuel or light heating oil, as was already reported in [46]. Evaporation of ethylene glycol does not start on the first 3-4 centimeters and is complete at around 30 cm.

Using CFD contour fields to measure evaporation is not completely intuitive, because an intensive parameter, i.e. the volume fraction of liquid, is used to apprehend an extensive quantity, the quantity of liquid remaining [182]. It is possible, from the CFD results, to integrate the quantity of liquid along a section. For example, the liquid mass flow rate over the section $\mathcal{S}$ is retrieved according

to:

$$\dot{m}_{\mathcal{S}} = \sum_{A \in \mathcal{S}} \left. \frac{V v_l^z \rho_l}{\Delta z} \right|_A , \tag{5.1}$$

where V_A is the volume of a cell belonging to the section $\mathcal{S}$, the liquid velocity in axial direction $v_{l,A}^z$ and the liquid density $\rho_{l,A}$ are taken at the cell centroid and Δz_A is the cell space discretization in the axial direction, which is actually constant along a section. This estimation over a section can be repeated for the total length of the reactor, which results in the blue curve of Figure 5.2c. In a similar way the liquid volumetric flow rate (red curve) can be calculated, simply by omitting $\rho_{l,A}$ in equation 5.1. It is possible to verify the integrity of the injected liquid from this figure. 12.56 kg/h of ethylene glycol are injected in the data set REGA-glycol-T1, which results for a 5° wedge $\frac{12.56}{3600}\frac{5}{360} = 4.85 \cdot 10^{-5}$ kg/s. The liquid is injected at 42.5 °C, which results in a density of 1097.7 kg/m^3 according to [183]:

$$\rho_l\left(T_l\right) = \frac{1.315 \cdot 62.068}{0.25125^{\left[1+\left(1-T_l/720\right)^{0.21868}\right]}}, \rho_l \text{ in kg/m}^3, T_l \in [260.15; 720] \text{ K}. \tag{5.2}$$

With this density, the volumetric flow rate at the injection should consequently give $4.42 \cdot 10^{-8}$ m^3/s, which complies with the simulation results. While the liquid mass flow rate is constant before the beginning of evaporation, the liquid volumetric flow rate increases. This is due to the liquid dilatation resulting from an increase in the liquid temperature. The evaporation really begins at 4/5 centimeters. The evaporation rate is at its maximum between 10 cm to 25 cm, and decreases slowly afterward. 99 % of the liquid have been evaporated at around 40 cm.

Simulation fields related to the gas phase are shown in Figure 5.3. Only, the axial gas velocity profile is displayed on the full reactor length (3.3 m). The other figures are restricted to the zone delimited by the red rectangle (0.7 m). The reactor shows two separate zones. The first 70 cm shows very high gas velocity, above 100 m/s, with important outer recirculation and below where the flow is similar to a plug flow, with an acceleration at the reactor outlet from geometrical shrinking.

The temperature field can be seen in Figure 5.3b. An attached and stabilized flame at the burner can be observed, though it was concluded that ethylene glycol evaporation begins after a couple of centimeters. The plot of ethylene glycol mole fraction in the gas phase, Figure 5.3c, also indicates clearly that the

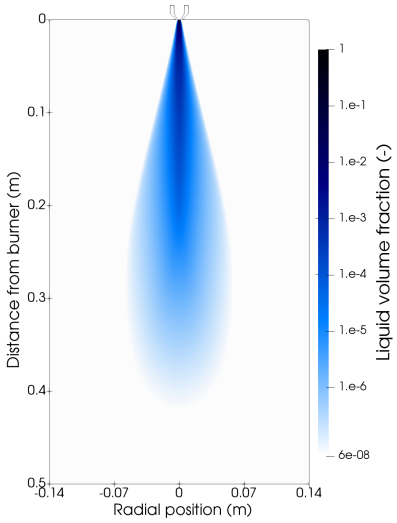

A) CFD contour of the liquid volume fraction

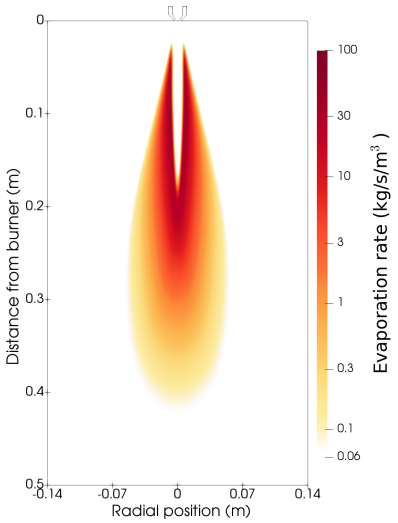

B) CFD contour of the evaporation rate

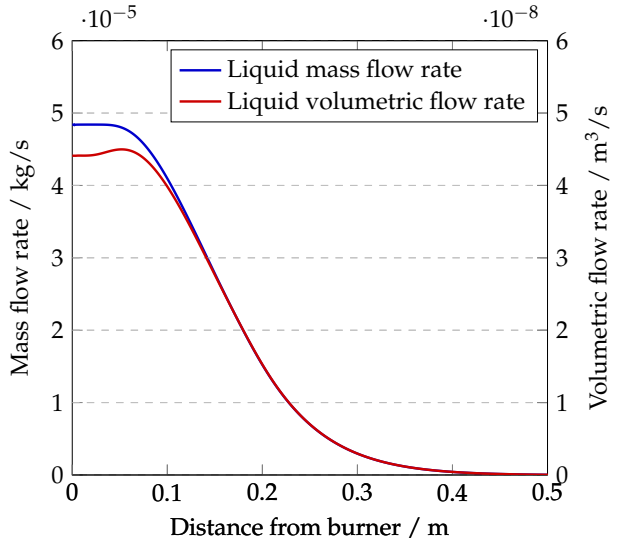

C) Liquid mass and volumetric flow rate along the axis

FIGURE 5.2: Results regarding the liquid phase for the data set REGA-glycol-T1

fuel can only be oxidized lately. The flame, thus, originates from syngas combustion. This can be seen with the production/consumption rate of hydrogen in Figure 5.3d and the hydrogen mole fraction in Figure 5.3e. Syngas is both produced and consumed in the gasifier. Hydrogen (it also applies to carbon monoxide) reacts with oxygen in the first 7-8 centimeters, which brings important heat release and provides heat for the evaporation and the further gas phase conversion. Temperatures above 2,000 K are observed. In absence or in limited amounts of oxygen, syngas is in turn produced. Then the recirculation zone

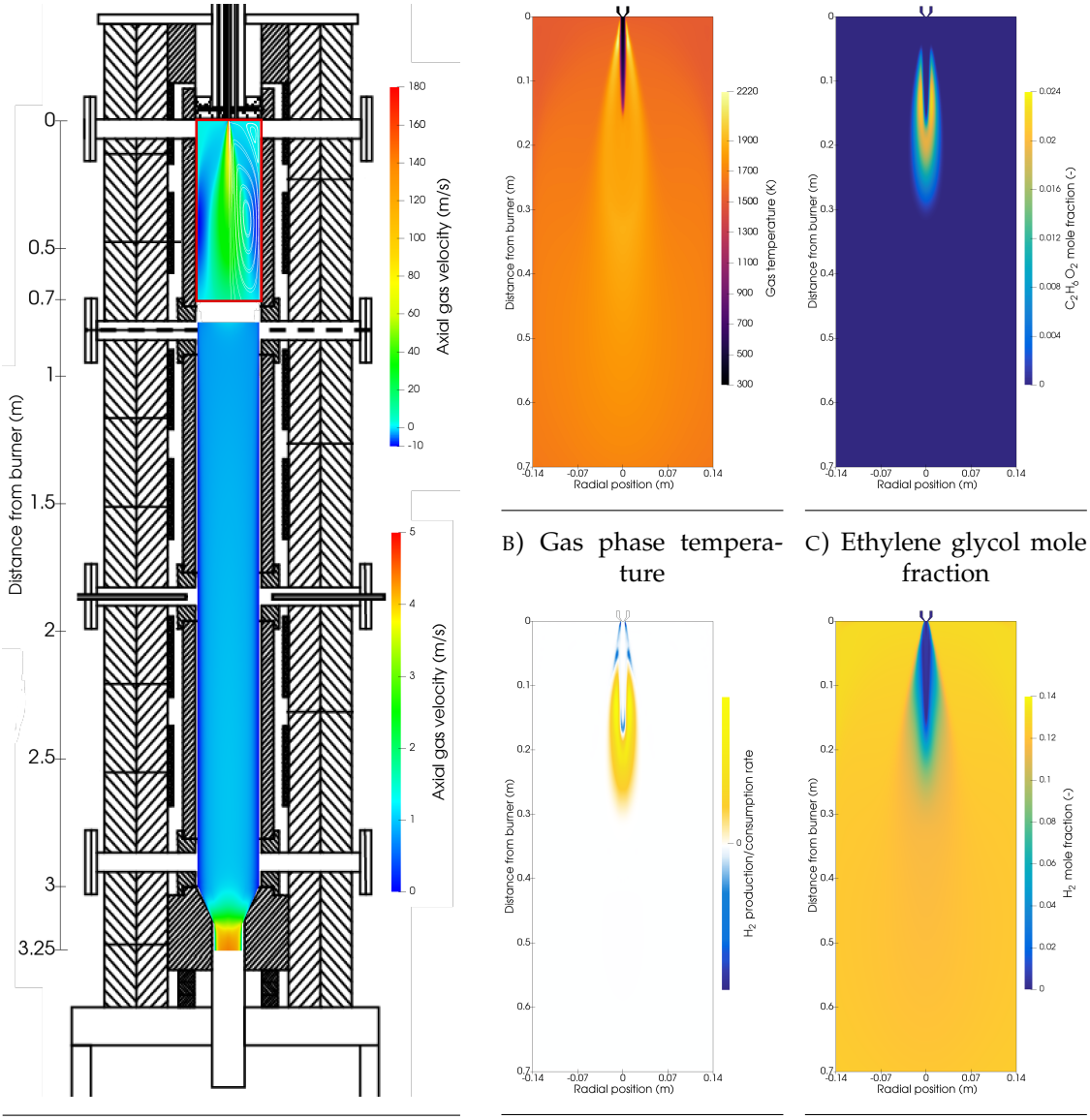

A) Axial velocity and streamlines in grey

B) Gas phase temperature

C) Ethylene glycol mole fraction

D) Hydrogen reaction rate

E) Hydrogen mole fraction

FIGURE 5.3: Gas phase CFD contours of the data set REGA-glycol-T1

plays a major role to bring the hot syngas to the burner vicinity. Such a phenomenon was also observed by Eckel et al. [101].

Other major species are shown in Figure 5.4. Beside hydrogen, the gasification main products are carbon monoxide (Figure 5.4a), water (Figure 5.4b), and carbon dioxide (Figure 5.4c). It is possible to identify several regions on these contours. For example, carbon dioxide is mainly product at the injection zone, where syngas reacts with oxygen. On the contrary, carbon monoxide's maximum concentration is located at the center axis around 30 cm below the nozzle. The gasification medium is also represented, in Figure 5.4d and 5.4e. We can see

that nitrogen is simply diluted, while the oxygen mole fraction reaches quickly zero as it get converted in radicals. Finally, the methane mole fraction is shown in Figure 5.4f. The region of methane production can clearly be identified in this figure. Other minor species fields, radicals, as well as reaction rates of the data sets REGA-glycol-T1 can be seen in Appendix C.1.

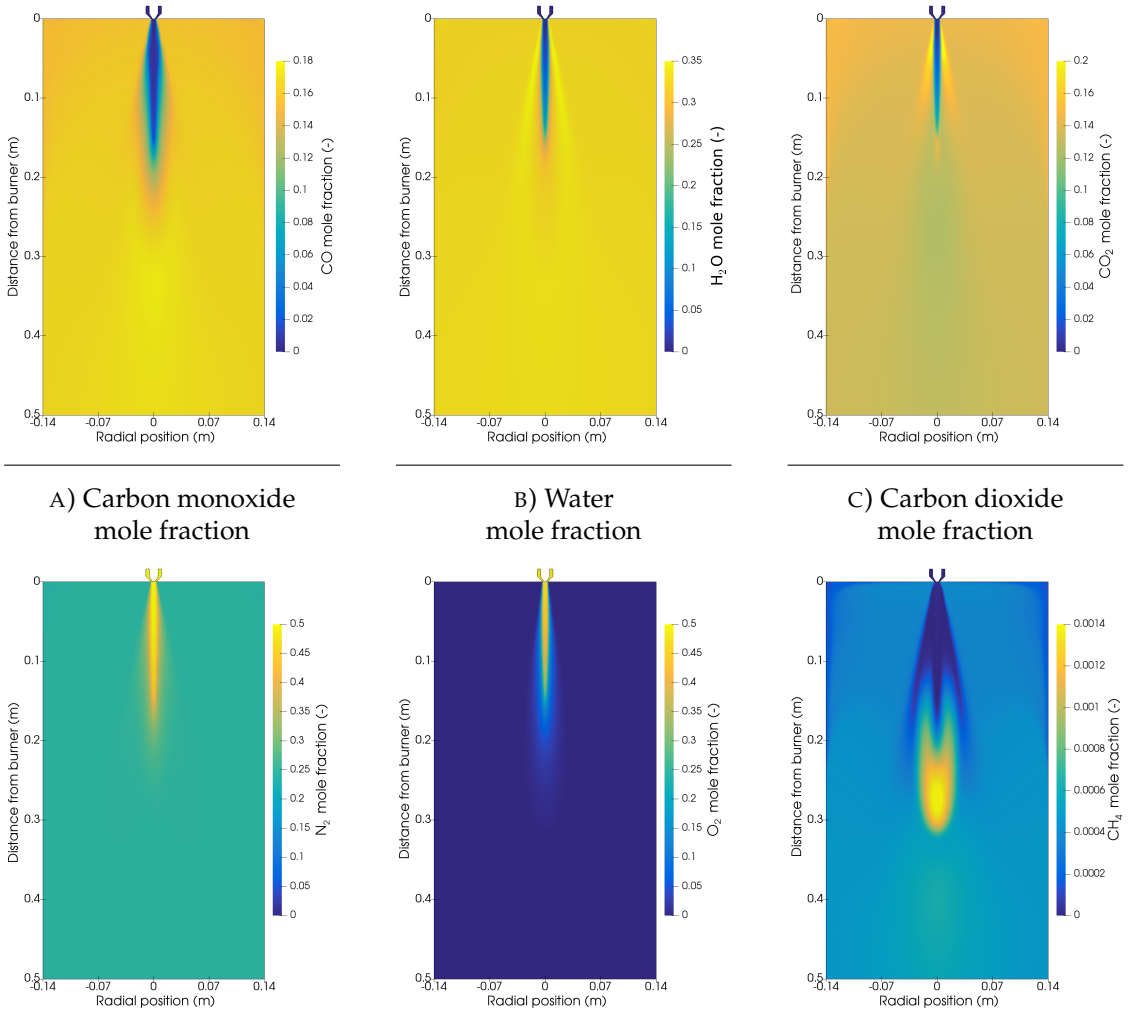

A) Carbon monoxide mole fraction

B) Water mole fraction

C) Carbon dioxide mole fraction

D) Nitrogen mole fraction

E) Oxygen mole fraction

F) Methane mole fraction

FIGURE 5.4: Major gas phase species of the data set REGA-glycol-T1

Quantitative results are shown in Figure 5.5. The experimental values have been taken at 300 mm and 680 mm downstream of the burner for the species concentration 5.5a, 5.5b and temperature 5.5c, 5.5d. The simulation (lines) and the experimental results (symbols) of Fleck et al. [97] agree quite well. In the experiment, H_2, CO, CO_2 and CH_4 have been measured while N_2 has been calculated by taking the difference. At 680 mm below the burner, experimental results show an almost flat profile for the species concentration, whose values

are almost retrieved in the simulation. At 300 mm, the concentrations evolve slightly along the radial position, and show either a minimum or a maximum at the center point. The profile is correct in the simulation for methane and carbon monoxide, the other species showing an inverse trend while approaching the center. This can be explained from the fact that radicals are present at this location. Therefore, oxidation of the fuel continues during the probe sampling and prior to the quench. For example, the simulation shows an important H radical concentration that will recombine during a probe sampling and increase the H_2 concentration. Concerning the temperature profiles, the simulation is able to retrieve with high enough accuracy the temperature peaks and the shape of the profiles.

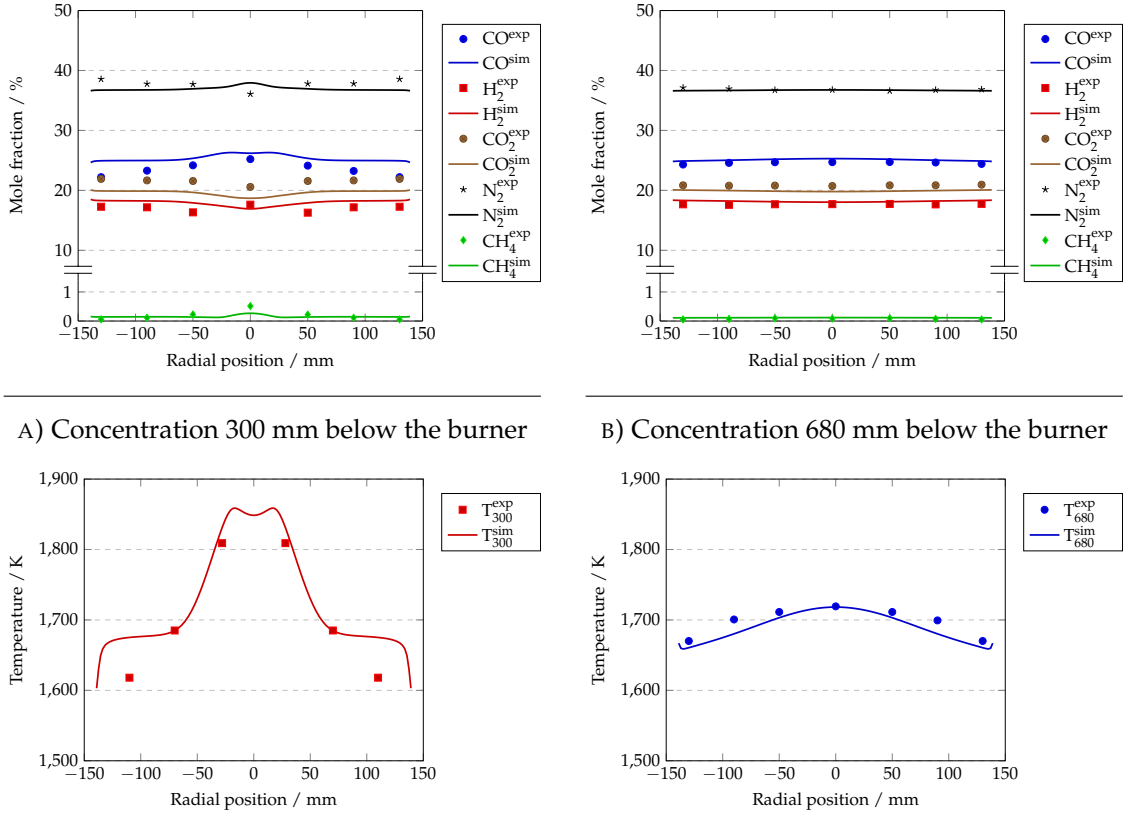

A) Concentration 300 mm below the burner

B) Concentration 680 mm below the burner

C) Temperature 300 mm below the burner

D) Temperature 680 mm below the burner

FIGURE 5.5: Experimental and simulation results for ethylene glycol gasification. Data taken from the dataset REGA-glycol-T1.

5.2.2 Effect of operating conditions on the gasification yield

In this section, we will try to determine to which extend some operating conditions alter the gasification yield. In particular, simulations will be run with

various nitrogen and oxygen flow rates and gasifier efficiency will be examined. To this extend, we will first examine the data set REGA-glycol-T2, whose operating condition are sensibly different from REGA-glycol-T1. In a second step, we will elaborate a matrix of plausible operating conditions and present the results of simulations.

The operating conditions of REGA-glycol-T2 are given in Table 5.1. The mass flow rate of fuel is almost the same as in the previous test case. What varies are the flow rates of oxygen and nitrogen. REGA-glycol-T2 operates with a smaller amount of oxygen and nitrogen. As the gasification medium is also the atomization medium, it implies bigger droplets. This was taken into account by adjusting the droplet size from 70 to 80 μm in the simulations. The simulation results are shown in Figure 5.6. The graphs are given in a consistent manner with Figure 5.5, to simplify a comparison. We can notice two main trends, an important increase of syngas but also a sharp increase in the methane concentration.

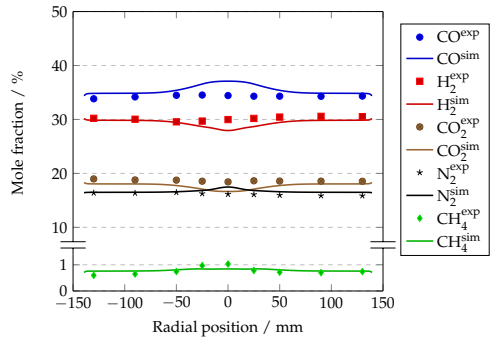

A) Concentration 300 mm below the burner

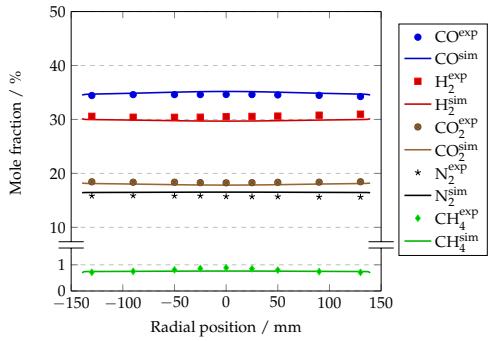

B) Concentration 680 mm below the burner

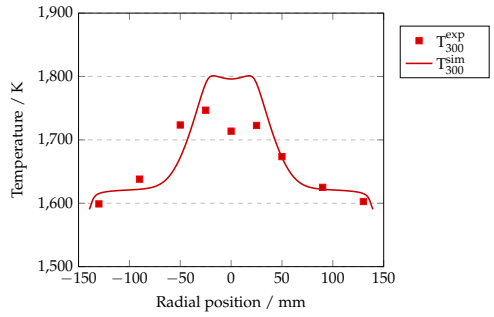

C) Temperature 300 mm below the burner

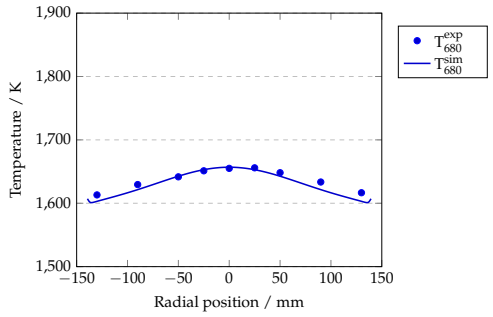

D) Temperature 680 mm below the burner

FIGURE 5.6: Experimental and simulation results for ethylene glycol gasification. Data taken from the dataset REGA-glycol-T2.

The simulation results for the two documented data sets give us enough confidence to simulate other operating conditions. Characteristic numbers are used

in combustion to describe operating conditions, such as stoichiometry, air-to-fuel ratio or equivalence ratio. Using air as an oxidant, these three numbers are inter-dependent. Here, enriched air is utilized, which means that we can vary oxygen and nitrogen separately. To describe the operating conditions, we will use the equivalence ratio ϕ and the **G**as-to-**F**uel **R**atio (**GFR**), respectively given by:

$$\phi = \frac{n_{O_2,st}}{n_{O_2}}, \tag{5.3}$$

and

$$GFR = \frac{\dot{m}_g}{\dot{m}_f}. \tag{5.4}$$

Thus, constant GFR and varying ϕ implies a constant total gas flow rate and varying O_2/N_2 ratio; constant ϕ and varying GFR implies a constant oxygen flow rate and varying nitrogen flow rate. Figure 5.7 shows every simulation condition that has been investigated. Operating conditions with flow rates comprised between REGA-glycol-T1 and REGA-glycol-T2 are tested, as well as operating conditions slightly below or above these two points. In total 29 simulations are run. The accumulation of all calculation times took less than 5,000 CPU-hours on a Intel Xeon CPU E5-2690 @ 2.90 GHz.

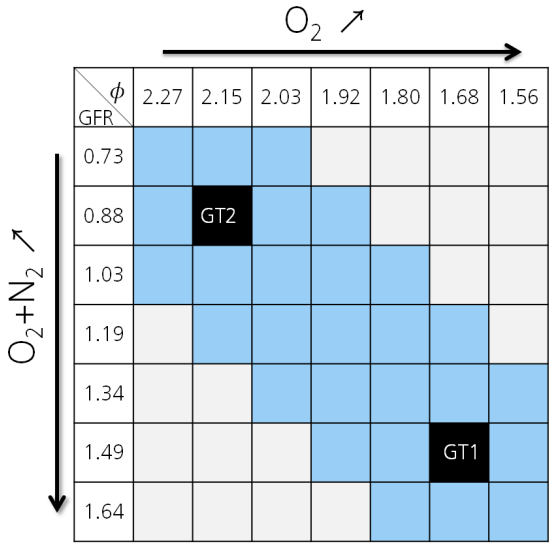

FIGURE 5.7: Operating conditions of the simulations run with conditions similar to the REGA-glycol-T1 (GT1) and REGA-glycol-T2 (GT2) datasets

Several quantities of interest can be analyzed to assess the gasification process. In the current case, the methane concentration and the **C**old **G**as **E**fficiency (**CGE**) have been retained. The methane content has been chosen because it is an undesired species, which is the main unburned hydrocarbon. To a lesser extent,

ethene can also be found. The second retained result is the Cold Gas Efficiency. It is a measure of the gasifier performance and accounts for the ratio between injected flow energy and the outlet gas energy. CGE is defined as:

$$CGE = \frac{\dot{m}^{\mathcal{I}} \mathrm{LHV}^{\mathcal{I}}}{\dot{m}^{\mathcal{O}} \mathrm{LHV}^{\mathcal{O}}}. \tag{5.5}$$

The results are shown in Figure 5.8. The methane content, given in Figure 5.8a, increases with higher equivalence ratio and air fuel ratio. The maximum being found at the point (2.27; 0.88) with 1.56 $\%_{mol}$ of the gas flow at dry conditions. At the lowest value of equivalence ratio and air fuel ratio (1.56; 1.34), an almost methane-free syngas can be found. The methane concentration at this point has been found to be 0.012 $\%_{mol}$.

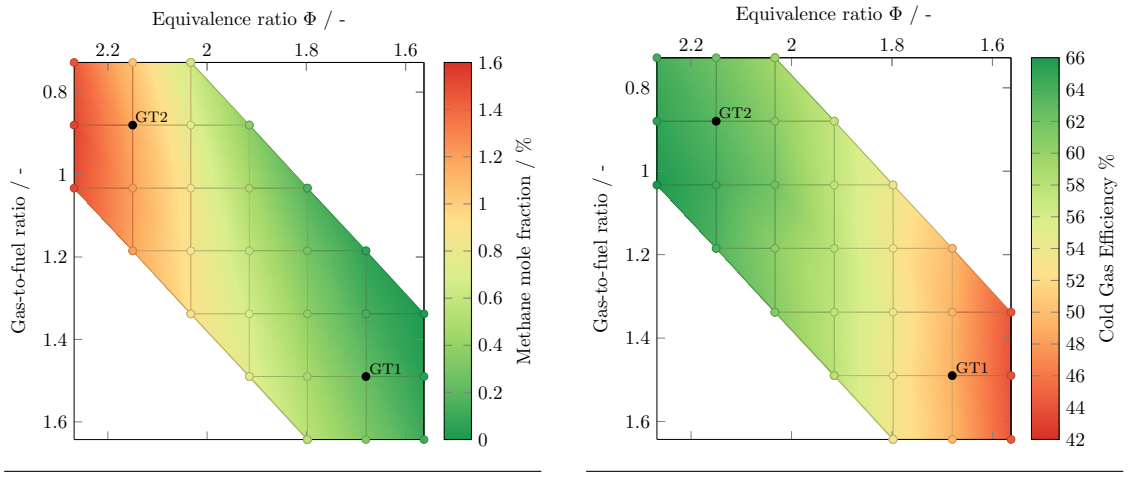

A) Methane mole fraction

B) Cold gas efficiency

FIGURE 5.8: Simulation results for the 29 simulations listed in Figure 5.7

It could have been expected that lower equivalence ratio decreases the methane produced, because, as we the get closer to stoichiometric condition, the amount of unburned hydrocarbons is reduced. More surprisingly, the amount of methane shows a marked dependency with the GFR, especially for lower equivalence ratio values. For example, the point (1.68; 1.19) and the point (1.68; 1.64) show a value of 0.065 and 0.329 $\%_{mol}$ respectively. Both points are characterized by the same amount of fuel and oxygen, only the nitrogen amount varies. The total flow rate of the point (1.68; 1.64) is much higher than for the point (1.68; 1.19), which mean that the difference in the net methane production is even higher than the difference in terms of concentration. This is due to a difference of flame properties. The CFD fields show a much longer high temperature zone for the

point (1.68; 1.19). A reason could be better mixing conditions at higher volumetric flow rate cases, leading to a faster combustion (shorter combustion zone). It has been shown that in REGA, the syngas that is formed recirculates and is partly oxidized in the injection zone, participating at the flame stabilization. The difference observed can then be explained by the flow structure, for example, by the part of gas that recirculates. This can modify the amount of syngas that is oxidized at the burner zone. More globally a better understanding of how much the oxidant is used for the syngas combustion and how much is used for the injected fuel in dependency of the operating conditions would be an asset for the reactor design.

The results for the Cold Gas Efficiency in Figure 5.8b show a clear dependency on the equivalence ratio, while the air fuel ratio has a very limited influence on the cold gas efficiency. Higher oxidant content, which was preferable to reduce the methane content, also reduces the efficiency. The gas composition is richer in carbon dioxide, which has a null calorific value. To reach a syngas composition that has a low methane content and a not too low efficiency, the best seems to be at intermediate equivalence ratios and a low GFR. This however means to have air highly enriched in oxygen. For example for the point (1.80; 1.03), we need to inject in terms of volumetric flow rate 1.6 times more oxygen than air, against only 0.4 for the point (1.80; 1.64). It means, if we make a better use of the fuel, the gasification medium is more expensive.

5.3 Gasification of ethylene glycol and char

5.3.1 REGA-slurry1-T2

REGA-slurry1-T2 [100] is the REGA data set with the most exhaustive information of the gasification cases with solid. The operating conditions can be found in Table 5.1; char originating from the fast pyrolysis of wood is used. The numerical setup relative to the solid and the sectional approach is reported in Appendix B. The data set is similar to REGA-glycol-T2. Almost the same fuel and nitrogen mass flow rates are used. The oxygen mass flow rate is however slightly more important in the slurry case (8.00 kg/h against 7.56 kg/h). Given these minor deviations, we can study the effects induced by the addition of solid solely.

The temperature results as well as the concentrations at 680 mm are displayed in Fig 5.9. For a better comparison, the results for the glycol case are

also shown on the left side. The simulations show here also a very good global agreement with the experimental data.

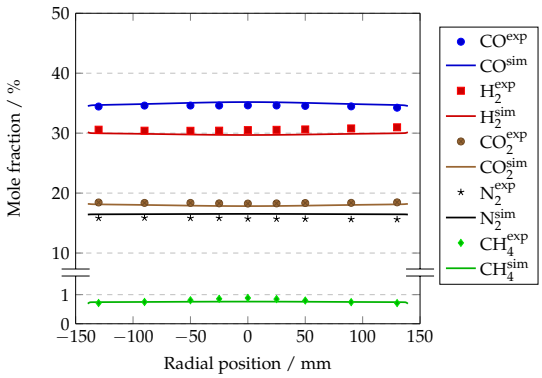

A) REGA-glycol-T2: concentration 680 mm below the burner

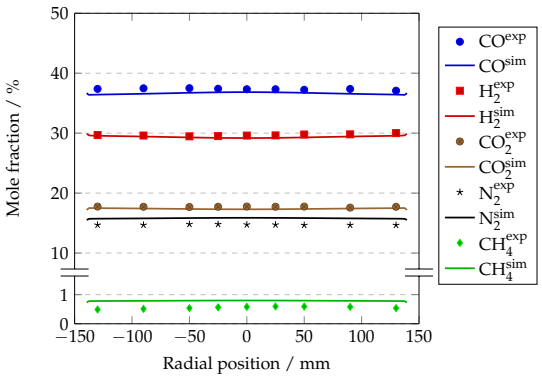

B) REGA-slurry1-T2: concentration 680 mm below the burner

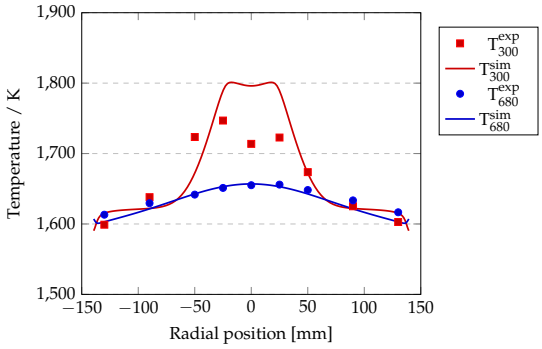

C) REGA-glycol-T2: temperature 680 mm below the burner

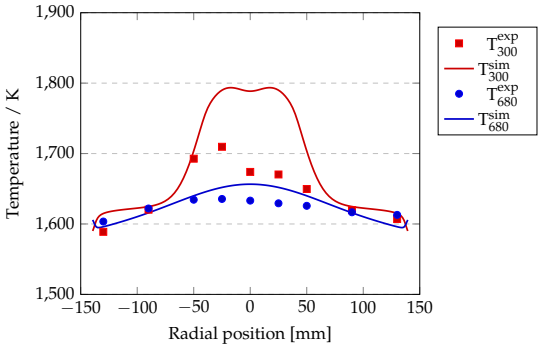

D) REGA-slurry1-T2: temperature 680 mm below the burner

FIGURE 5.9: Comparison of experimental and simulation results between ethylene glycol gasification (REGA-glycol-T2, left) and wood slurry gasification (REGA-slurry1-T2, right)

It is important to refer to the REGA-glycol-T2 results, because it is not possible to distinguish in the slurry simulation between the different error sources, originating from the glycol treatment or from the char modeling. Therefore, the examination of the trends between the two cases is more valuable. For example, the concentration results for REGA-slurry1-T2 show an overestimation for CO_2 and an underestimation for N_2. But these deviations were already observed for REGA-glycol-T2. The evolution of the species concentrations between the test case with only ethylene glycol and the slurry case is reported in Table 5.2. The data given in the Table are arithmetic means. For example, both experimental data sets count 9 result points R_p; the average evolution is then given by $\sum_{R_p}\left(X_{R_p}^{slurry} - X_{R_p}^{glycol}\right)/N_{R_p}$ (X expressed in %). The second line of the table corresponds to the simulation displayed in Figure 5.9b. This simulation was run

with the reference pre-exponential factor A_r^G as given in the numerical setup in Appendix B. The third and fourth line shows the results for varying gasification rates. The pre-exponential factor for all gasification rates has been multiplied or divided by a factor of 3. The simulation results are very sensitive to this parameter A_r^G. The reference kinetic parameters, A_r^G and E_a, proposed in this work are of the correct order of magnitude. Taking $A_r^G \cdot 10$ or $A_r^G/10$ would lead to high deviations for all species. Still, due to multiple error sources, it is difficult to refine more the accuracy on A_r^G. For example, following the results given in Table 5.2, the reference case gives the best results for CO_2, while the case $A_r^G \cdot 3$ tends to gives better results for CO, and $A_r^G/3$ better results for H_2.

TABLE 5.2: Evolution of the compositions at 680 mm below the burner between REGA-glycol-T1 and REGA-slurry1-T2

Average evolution / %	CO	H_2	CO_2	N_2	CH_4
In the experiments	+2.82	−0.91	−0.64	−1.03	−0.24
In the simulation with A_r^G	+1.70	−0.45	−0.59	−0.69	+0.04
In the simulation with $A_r^G \cdot 3$	+2.70	−0.01	−1.53	−1.25	+0.08
In the simulation with $A_r^G/3$	+0.84	−0.91	+0.24	−0.19	+0.01

It appears difficult to optimize one parameter due to the numerous modeling variables and experimental uncertainties. Nevertheless, two major modeling limitations may be raised. First, concerning the gasification rate: in the present modeling, the same constants have been used, independent of the oxidant (CO_2 or H_2O) and of the size class. Better results would be for example expected by decreasing the gasification rate with water steam to the profit of the gasification with carbon dioxide. Less hydrogen would be formed but more CO, which would respect more the trends. The second reason concerns the secondary pyrolysis. The assumption was made that the secondary char contains only carbon and ash. In reality, we would observe a few percent of hydrogen left in the char. This second issue was investigated in [145]. The use of a volatile set of species with a smaller hydrogen content implied a diminution in hydrogen content and an augmentation in CO content.

Methane is a particular species. The gasification rate has very little effect on its concentration. In the experiment, a decrease of methane is observed, while the methane content in the simulations stays almost constant. It can be assumed that the deviation observed does not originate from the uncertainty of the gasification kinetic rate. De facto, methane is not involved in the gasification reactions. The evolution between the different simulations should arise from dilution effect or temperature differences. Now, several causes may be attributed to

the discrepancy between experiments and simulations. One plausible reason is the modeling of the volatile set of species. The species CH_4 was chosen as a representative species of the volatiles. This assumption may be wrong and explain the overestimation of this species in the simulations.

The contour plots of the total mass fraction of the primary char, the secondary char, and the ashes can be seen in Figure 5.10. The plots for the class 2, 6, and 10 of each solid types are also given in Appendix C.2, to show the dependence on the particle size. As expected, the primary char appears in the zone of liquid evaporation and is then quickly converted. The conversion is faster for the smaller class, but the changes are minor. The wood char particles are even smaller than for the straw char. The wood char devolatilization is expected to be fast, and does not constitute a limiting step. The upper corners and the region below 70 cm correspond to a higher residence time and are impoverished in primary char. Due to the high momentum, secondary char and ash are mostly not present in the jet zone. In contrast to the primary char, ash occupies regions of long residence time. An important amount of char is found in the upper corners. Below, the concentration is higher as we get closer to the walls. Two reasons can be given: first, the walls are heated, the temperature difference between the center of the reactor and the wall increase along the axis. Secondly, the plug flow velocity profile induces a shorter residence time from the central streamlines.

In order to understand the dependence of the solid conversion on the particle size and on the position in the reaction, four points, denoted A, B, C, and D, have been extracted and the corresponding results can be seen in Figure 5.11. Some operations on the CFD fields must be performed to ensure a correct comparison. For example, we denote $Y^{sim.}_{\mathrm{BIN}_c^{Ash}}$ the mass fraction of ash of the class c as extracted from the simulation. To compare ash (which accounts for only 1.6 % of the primary char) with the other types of solid, we have to divide this mass fraction by $\%^{wood}_{Ash}$. Similarly, the mass fractions for the secondary char must be divided by $\%^{wood}_{C_{fix}} + \%^{wood}_{Ash}$. The second operation performed is a normalization. We denote Υ the normalized mass fractions obtained after these two operations. We have, for instance, for the mass fraction of ash of the class c:

$$\Upsilon_{\mathrm{BIN}_c^{Ash}} = \frac{1}{\sum_c Y^{sim.}_{\mathrm{BIN}_c^{1^{st}char}} + \frac{\sum_c Y^{sim.}_{\mathrm{BIN}_c^{2^{nd}char}}}{\%^{wood}_{C_{fix}} + \%^{wood}_{Ash}} + \frac{\sum_c Y^{sim.}_{\mathrm{BIN}_c^{Ash}}}{\%^{wood}_{Ash}}} \frac{Y^{sim.}_{\mathrm{BIN}_c^{Ash}}}{\%^{wood}_{Ash}}. \tag{5.6}$$

The left fraction corresponds to the normalization step and is invariant with the class and type of solid.

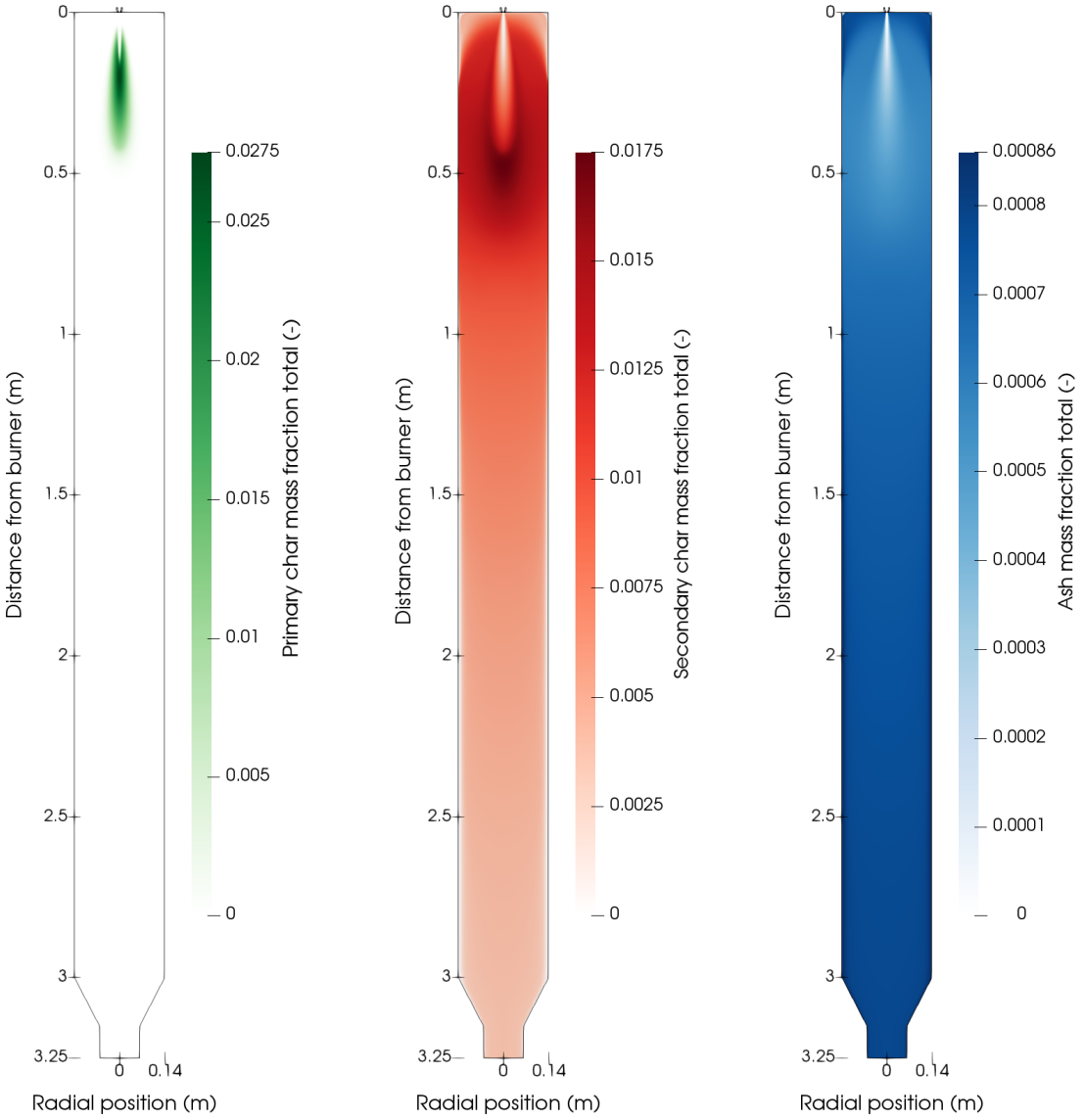

A) Primary char B) Secondary char C) Ash

FIGURE 5.10: Total mass fractions of the three types of solid

We can derive from these normalized mass fractions a global conversion percentage:

$$\chi_{char} = \sum_{c} \left(\Upsilon_{\mathrm{BIN}_c^{1^{st}char}} \cdot 0 + \Upsilon_{\mathrm{BIN}_c^{2^{nd}char}} \cdot 24.8 + \Upsilon_{\mathrm{BIN}_c^{Ash}} \cdot 100 \right). \tag{5.7}$$

With this formula, we obtain a number comprised between 0 and 100 %. 0 % if only primary char can be found, 100 % if all the solid has been converted to ash. With only secondary char, we would obtain an intermediate conversion $\chi_{char} = \%_{vol}^{wood}$ =24.8 %.

The first point A is located at (r=0 m; z=0.3 m), the point B at (r=0.1 m; z=0.3 m), C at (r=0 m; z=1.5 m), and D at (r=0 m; z=3 m). The point A corresponds to a point in the jet zone. It is the only point extracted that shows primary char. In the other points, all primary char has already been consumed. Also point A shows an important conversion of primary char; the global conversion is equal to 40 %. It can be assumed that an important part of the already converted solid (secondary char, ash) originates from recirculation inside the reactor. The points B, C, and D show gradual concentration in ash. The point B corresponds to the recirculation zone, the point C is located at the reactor center, and the point D at the reactor outlet. The solid is already converted at 61 % at the point B, which indicates that an important conversion in the first meter of the gasifier. The solids particles can recirculate several times in the reactor before going downstream, which participate in their gasification. The solid conversion continues along the reactor, as a slower rate. The global conversion goes from 72 % at the point C to 78 % at the point D.

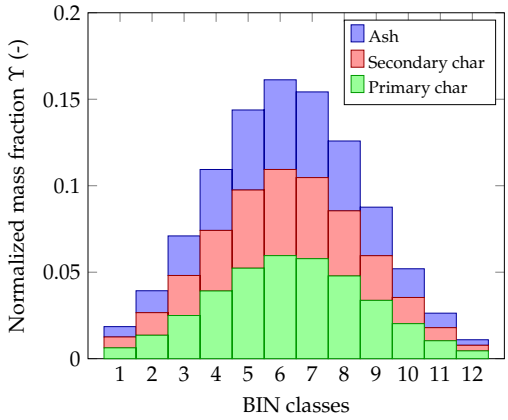

A) Point A (r=0 m; z=0.3 m), $\chi_{char} = 40$ %

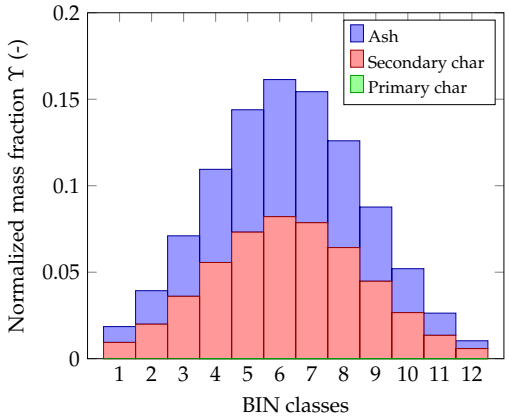

B) Point B (r=0.1 m; z=0.3 m), $\chi_{char} = 61$ %

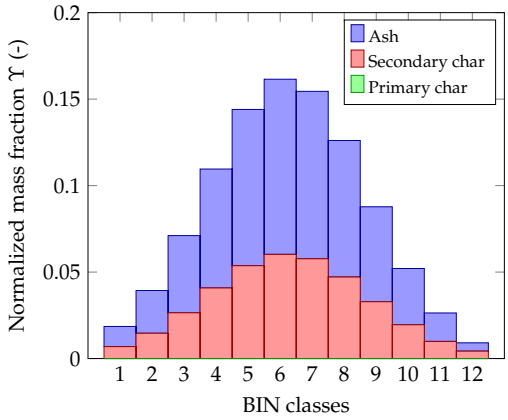

C) Point C (r=0 m; z=1.5 m), $\chi_{char} = 72$ %

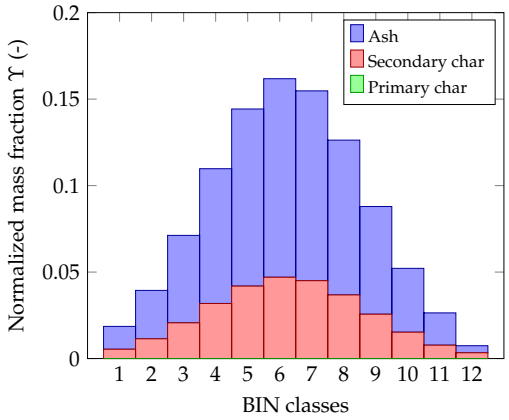

D) Point D (r=0 m; z=3 m), $\chi_{char} = 78$ %

FIGURE 5.11: Char conversion at different positions in the reactor

5.3.2 Comparison with a second char

In this section, the simulation related to the data set GSKS10 will be discussed. Thus, a second type of solid, char originating from the fast pyrolysis of straw, will be considered. However, less data are available: the infiltration air is unknown and the nitrogen results are not available.

The operating conditions are summarized in Table 5.1 and the char modeling in Appendix B. As the mass flow rate of infiltration air is unknown, different simulations have been performed. We denote $\dot{m}_{Inf.\ Air}$ the mass flow rate of infiltration air of REGA-slurry1-T1. Three simulations have been performed, one without infiltration air, one with $\dot{m}_{Inf.\ Air}$ and one with two times $\dot{m}_{Inf.\ Air}$. Table 5.3 shows the average deviation between experiment and simulations. As it can be seen, the simulation without infiltration air shows very high deviations, and the one with $2 \cdot \dot{m}_{Inf.\ Air}$ shows the overall best agreement. Simulation with this last operating condition is reported in Figure 5.12b.

TABLE 5.3: GSKS10: Comparison of the compositions at 680 mm below the burner between experiment and simulation

Average deviation / %	CO	H_2	CO_2	CH_4
Simulation with $2 \cdot \dot{m}_{Inf.\ Air}$	−0.60	+1.27	−1.03	+0.34
Simulation with $1 \cdot \dot{m}_{Inf.\ Air}$	−0.49	+1.81	−1.85	+0.52
Simulation with $0 \cdot \dot{m}_{Inf.\ Air}$	−0.59	+2.94	−3.24	+0.87

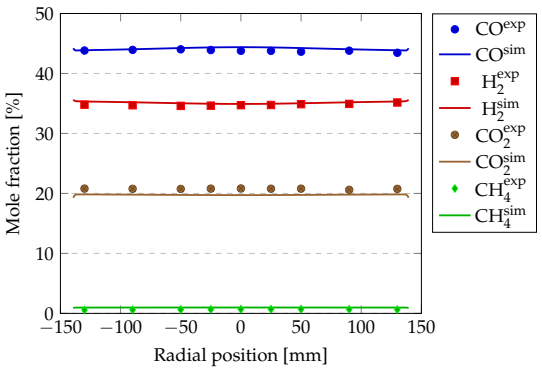

A) REGA-slurry1-T2: concentration 680 mm below the burner

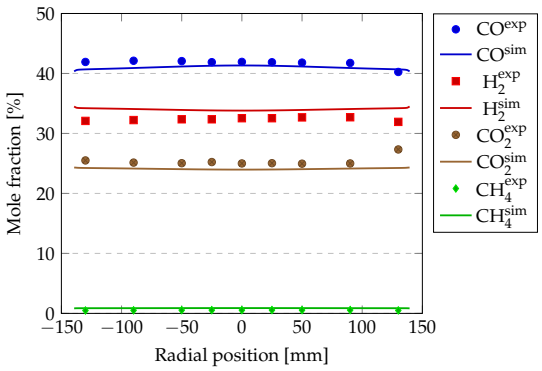

B) GSKS10: concentration 680 mm below the burner

FIGURE 5.12: Comparison of experimental and simulation results between wood slurry gasification (REGA-slurry1-T2, left) and straw slurry gasification (GSKS10, right)

Even if the experimental conditions for the slurry with straw char are more uncertain, Figure 5.12 shows sufficient agreement to perform an analysis on the

impact of the nature of the solid. If we compare the two types of solids, the straw char particles are much larger than those of wood char (factor 10 for the mass). It is not expected to have a major impact on the secondary pyrolysis. The duration for completion will be higher for straw but is not supposed to be a limiting step in both cases. However, the composition of both char differs greatly, and thus the volatiles quantity and composition is different. Straw char shows a higher hydrogen and oxygen content, but a smaller volatile content. The fact that straw char has a lower volatile content may explain the sharp increase in CO_2, because it may lower the fuel quantity locally and get closer to stoichiometric conditions.

However, the hydrogen decrease noticed in the results cannot be explained from the chars' composition, where the trend is inverse. A possible explanation is the better carbon conversion with water for the wood char. As a matter of fact, if the wood char seems to have an almost total conversion, the simulation suggests that straw char is only partially converted. This can be seen in Figure 5.13, the global conversion factor χ_{char} reaches nearly 50 % at the reactor outlet. This lower reactivity can be multifactorial, with for example the ash content and composition, the solid morphology, or the fact that the straw char particle were much larger.

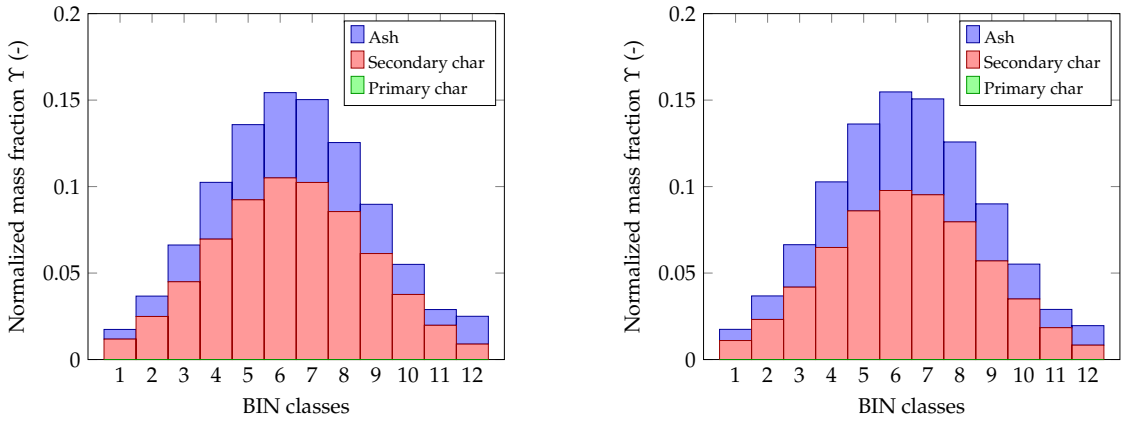

A) Point C (r=0 m; z=1.5 m), $\chi_{char} = 44$ %

B) Point D (r=0 m; z=3 m), $\chi_{char} = 48$ %

FIGURE 5.13: Char conversion at different positions in the reactor

5.3.3 Higher char content

In this last section, the gasification of a slurry with a higher solid content is investigated. REGA-slurry1-T2 and GSKS10 contained only 10 % of solids, masking partially the uncertainties related to the solid modeling. For this reason, simulation with a slurry containing 30 % of wood char is performed. Experimental data can be found in [102]. The N_2 concentration is not given and only data at 680 mm are available. However, infiltration air is known. The purpose is to further validate the model developed for the wood char. In this attempt, the exact same parameters as in REGA-slurry1-T2 are used, with the inlet values, gas and slurry velocities being an exemption.

Similarly to the simulation performed with 10 % of wood char, three simulations with varying gasification rate A_r^G have been performed. The deviation between the experimental data and the simulation are displayed in Table 5.4.

TABLE 5.4: REGA-slurry2-T2: Comparison of the compositions at 680 mm below the burner between experiment and simulation

Average deviation / %	CO	H_2	CO_2	CH_4
Simulation with A_r^G	-0.3	-0.6	$+0.8$	$+0.17$
Simulation with $A_r^G \cdot 3$	$+2.0$	$+0.2$	-2.5	$+0.25$
Simulation with $A_r^G / 3$	-3.0	-2.1	$+5.1$	$+0.00$

The numerical tools show their ability to perform simulations with a higher char content. In particular, the simulation with A_r^G shows an excellent agreement with the experiment.

As it could be expected, the sensitivity on the parameter A_r^G is much higher than in the simulation with 10 % of char. Indeed, the solid accounts here for 30 % of the fuel, and thus, the results are more sensitive to all modeling choices related to the solid. In consequence, this data set allows us to further reduce the uncertainty of this reaction rate.

By performing successive simulations, it is possible to refine the gasification pre-exponential factor and find a value that minimize the sum of the average deviations. We find an optimized value find $A_{r,opt}^G = 2.1 \cdot 10^9\ 1/\mathrm{s}/(\mathrm{mol}/\mathrm{m}^3)^{0.6}$, which corresponds to $A_r^G \cdot 1.42$. The results are displayed in Figure 5.14. A further improvement of the model would consist in having differentiated gasification rates whether the oxidant is water or CO_2. Nevertheless, in the present case, the use of a unique rate was sufficient to obtain good results, as the figure shows. The contours of the total mass fractions with varying gasification rate are

also shown in Appendix C.3. Concerning the global conversion, the simulation shows similar solid consumption. For example, $\chi_{char} = 71\%$ at the point D.

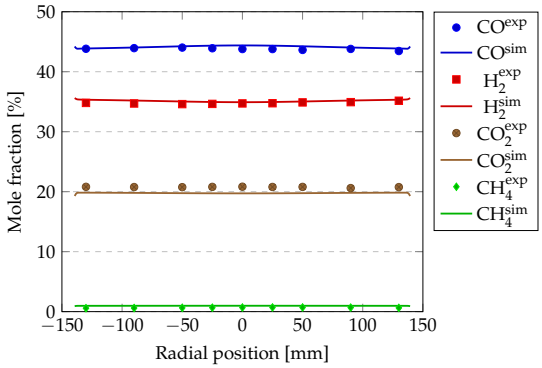

A) REGA-slurry1-T2: concentration 680 mm below the burner

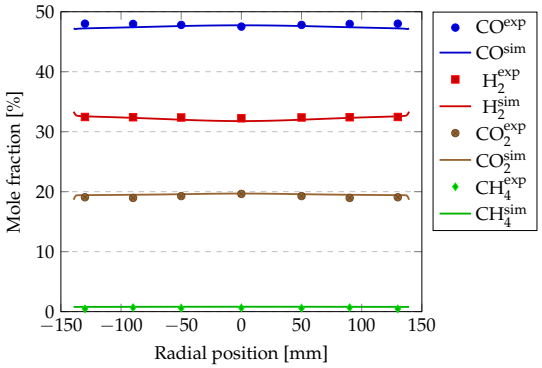

B) REGA-slurry2-T2: concentration 680 mm below the burner

FIGURE 5.14: Comparison of experimental and simulation results between wood slurry gasification with 10 % of solid (REGA-slurry1-T2, left) and wood slurry gasification with 30 % of solid (REGA-slurry2-T2, right)

Chapter 6

Conclusion

Synthetic fuels derived from biogenic resources may play a crucial role to meet the challenging effort that greenhouse gases mitigation requires. Many demonstration units have proven the feasibility of the process. Though, the production seems to stagnate, mainly because of economical constraints. As of now, Biomass-to-Liquid processes, such as the bioliq process, needs to be optimized. Simulation based on Computational Fluid Dynamics can help have a better insight of entrained-flow gasification processes. Throughout this thesis, fundamental models, along with novel approaches, have been presented. Then, the simulation tools have been validated against the experimental data of the REGA gasifier.

Chapter 2 has presented the basic concepts of CFD applied to combustion cases. It was shown that the necessary framework consists of the extended Navier-Stokes equations (continuity, momentum and energy), as well as chemical species transport equations. Partial differential equations that transcribe these conservation principles can be derived in a generic way, which facilitate the numerical task. The present work is based on OpenFOAM, a simulation toolbox that relies on the Finite Volume Method. The discretization step of the domain and the equations has been presented, as well as the algorithm that resolves the pressure-velocity coupling. Finite rate chemistry is employed to model multicomponent reactive cases, and in this context, the numerical treatment of the chemical source term has been presented. A laminar hydrogen flame was investigated to validate the simulation tool at this point. The foreseen application, entrained-flow gasification, is characterized by high Reynolds numbers, which implies the necessity to model the turbulence. The principle of the RANS approach as well as its pros and cons have been discussed. Further models were presented such as the SST $k - \omega$ for the turbulence closure model and the PaSR model for the Turbulence Chemistry Interaction.

Chapter 3 was dedicated to the treatment of multiphase systems, as involved in entrained-flow gasification. In particular, a two-phase Eulerian model, applied to the case of a liquid spray in a gas continuum, was presented. This model is based on the so-called conditional volume-averaging. As a result, two sets of governing equations have been derived, which show similarities to the Reynolds-Averaged NS equations. Each phase is described by a set of conservation equation that features, in particular, its volume fraction. This term is a key variable of the approach, which requires a right treatment to ensure conservation and boundedness. The sets of equation also exhibit coupling terms, which need to be modeled according to the studied case. Here, evaporation is one of the main sub-processes that induces transfers between the two phases. Its modeling includes mass, momentum, energy, and species transfer. The core equation relies on the Spalding's evaporation rate; correlations are employed to close the model. The momentum transfer needs particular terms, especially due to the drag force and the turbulent dispersion. This chapter was concluded by a validation case, which aimed at pointing out the similarity with a traditional lagrangian solver and the natural transition of the two-phase Eulerian solver from a 3D grid to a 2D one.

Chapter 4 has extended the modeling for the entrained-flow gasification to the case of solids. A sectional approach has been developed and adapted to the peculiarities of char gasification. The solid elements have been, not only divided according to their mass into representative classes, but also grouped into three conversion stages, namely primary char, secondary char, and ash. It has resulted in a set of $3 \cdot N_c$ species that can be used freely in a mechanism. The next steps consist in: defining reactions linking the newly created species; finding the corresponding stoichiometric coefficients; estimating kinetic rates based on experiment conducted at KIT. Then, the evaporation model developed in the previous chapter has been extended to include the presence of solid particles. Finally, a method to derive the thermodynamic properties of the three types of solid has been presented. The sectional approach proposed in this chapter was conducted with straw char, by way of illustration. This method can nevertheless be reemployed in a systematic way for other solids, based on a particle size distribution, a proximate, and an ultimate analysis.

Chapter 5 has employed the models developed and has validated them with experimental data of entrained-flow gasification. In particular, the numerous data sets delivered by the REGA gasifier were reproduced. This laboratory-scale reactor with in-situ measurement possibilities can operate with ethylene glycol, as a surrogate for pyrolysis oil, or with a slurry made of EG and char.

First, ethylene glycol gasification was studied. The good agreement for two distinct operating conditions has comforted the current modeling. On this basis, further conditions were tested and the associated results in term of process efficiency and pollutant concentration were presented. Secondly, gasification of slurries was investigated. The sectional approach's capabilities were shown. It was also observed that the char nature, as well as the quantity of solid in the slurry, induces major changes in the gasification performance. With appropriate parameters, the sectional approach can reproduce the observed changes.

Further enhancement and use of the models can be foreseen. In the current state, predictive simulations of ethylene glycol gasification in the REGA conditions (atmospheric pressure, similar flow rates) are possible. Concerning the slurry gasification, however, a priori values for the gasification kinetic rates are missing. REGA results were necessary to find these parameters. Determining these data in advance, either from analytical techniques or from a theoretical model, would close this gap. The current model also makes no distinction between the different oxidants. In the view of performing reactor scaling-up, the simulation tools should be expanded notably to include high-pressure induced phenomena. These changes would comprise the equation of state, the spray behavior, or the gasification rates. Despite this necessary model extension, the fundamental approaches proposed would be particularly suited for a transition into high-pressure conditions. The two-phase Eulerian approach provides a more accurate description of the physics for dense sprays and the sectional approach would perform equally at higher particle loading in contrast to a Lagrangian approach.

Bibliography

[1] R. Probstein, R. Hicks, Synthetic Fuels, Dover Books on Aeronautical Engineering Series, Dover Publications, 2006, p. 1. URL: https://books.google.de/books?id=7mAl_1f2XzQC.

[2] S. Markov, Biofuels and synthetic fuels, in: D. R. Franceschetti (Ed.), Applied Science, Salem Press, 2012, pp. 199–204. URL: https://www.researchgate.net/publication/281596949_Biofuels_and_Synthetic_Fuels.

[3] S. De, A. Agarwal, V. S. Moholkar, T. Bhaskar, Coal and Biomass Gasification: Recent Advances and Future Challenges, Springer Singapore, 2017, p. 4. doi:10.1007/978-981-10-7335-9.

[4] K. Aasberg-Petersen, I. Dybkjær, C. Ovesen, N. Schjødt, J. Sehested, S. Thomsen, Natural gas to synthesis gas – catalysts and catalytic processes, Journal of Natural Gas Science and Engineering 3 (2011) 423–459. doi:10.1016/j.jngse.2011.03.004.

[5] M. Stelmachowski, L. Nowicki, Fuel from the synthesis gas—the role of process engineering, Applied Energy 74 (2003) 85–93. doi:10.1016/S0306-2619(02)00134-4.

[6] J. van de Loosdrecht, F. Botes, I. Ciobica, A. Ferreira, P. Gibson, D. Moodley, A. Saib, J. Visagie, C. Weststrate, J. Niemantsverdriet, 7.20 - fischer–tropsch synthesis: Catalysts and chemistry, in: J. Reedijk, K. Poeppelmeier (Eds.), Comprehensive Inorganic Chemistry II, Elsevier, Amsterdam, 2013, pp. 525–557. doi:10.1016/B978-0-08-097774-4.00729-4.

[7] C. Lechthaler, J. Wise, P. Weisz, A. Silvestri, Novel technology for conversion of methanol and synthesis gas to hydrocarbons, in: Proceedings of the 13th Intersociety Energy Conversion Engineering Conference, San Diego, California, Society of Automotive Engineers, 1978, pp. 476–481. URL: https://www.researchgate.net/publication/253172830_Novel_

technology_for_conversion_of_methanol_and_synthesis_gas_to_hydrocarbons.

[8] L. E. Lücking, Methanol Production from Syngas, Master's thesis, Delft University of Technology, Delft, 2017. URL: http://resolver.tudelft.nl/uuid:c0c5ebd2-c336-4f2d-85d1-014dae9fdf24.

[9] J. Berg, van den, The conversion of methanol to gasoline on zeolite H-ZSM-5 : a mechanistic study, Ph.D. thesis, Eindhoven university of technology, Eindhoven, 1981. doi:10.6100/IR30334.

[10] F. Bergius, Die Anthracitbildung, Zeitschrift für Elektrochemie und angewandte physikalische Chemie 19 (1913) 858–860. URL: https://onlinelibrary.wiley.com/doi/abs/10.1002/bbpc.19130192106.

[11] F. Fischer, H. Tropsch, Die Erdölsynthese bei gewöhnlichem Druck aus den Vergangsprodukten der Kohlen, Brennstoff-Chemie 7 (1926) 97–104.

[12] S. P. Keller, Turning Point: A history of German petroleum in world war II and its lessons for the role of oil in modern air warfare, Report, Air university-Maxwell, Air Force Base United States, 2011. URL: https://apps.dtic.mil/dtic/tr/fulltext/u2/1020261.pdf.

[13] M. Höök, D. Fantazzini, A. Angelantoni, S. Snowden, Hydrocarbon liquefaction: viability as a peak oil mitigation strategy, Philosophical Transactions of the Royal Society A: Mathematical, Physical and Engineering Sciences 372 (2014) 36. doi:10.1098/rsta.2012.0319.

[14] J. Gurney, B. Petroleum Company, BP Statistical Review of World Energy, Technical Report 67, British Petroleum Co., 2018. URL: https://www.bp.com/content/dam/bp/business-sites/en/global/corporate/pdfs/energy-economics/statistical-review/bp-stats-review-2018-full-report.pdf.

[15] Intergovernmental Panel on Climate Change, available at https://www.ipcc.ch/about/, accessed: July 6, 2020.

[16] United Nations Treaty Collection, Paris agreement, 2015. URL: https://treaties.un.org/doc/Treaties/2016/02/20160215%2006-03%20PM/Ch_XXVII-7-d.pdf.

[17] V. Masson-Delmotte, P. Zhai, H.-O. Pörtner, D. Roberts, J. Skea, P. Shukla, A. Pirani, W. Moufouma-Okia, C. Péan, R. Pidcock, S. Connors, J. Matthews, Y. Chen, X. Zhou, M. Gomis, E. Lonnoy, T. Maycock, M. Tignor, T. Waterfield, Global Warming of 1.5°C. An IPCC Special Report on the impacts of global warming of 1.5°C above pre-industrial levels and related global greenhouse gas emission pathways, in the context of strengthening the global response to the threat of climate change, sustainable development, and efforts to eradicate poverty, Technical Report, Intergovernmental Panel on Climate Change, 2018. URL: https://www.ipcc.ch/site/assets/uploads/sites/2/2019/06/SR15_Full_Report_High_Res.pdf.

[18] WBA, Global bioenergy statistics 2018, Technical Report, World Bioenergy Association, 2018. URL: https://worldbioenergy.org/global-bioenergy-statistics.

[19] Working Group on Renewable Energy-Statistics (AGEE-Stat), Time series for the development of renewable energy sources in Germany, Report, Federal Ministry for Economics Affairs and Energy, 2019. URL: https://www.erneuerbare-energien.de/EE/Navigation/DE/Service/Erneuerbare_Energien_in_Zahlen/Zeitreihen/zeitreihen.html.

[20] BMU, Arbeitsgruppe IK III 1, Klimaschutzplan 2050 Klimaschutzpolitische Grundsätze und Ziele der Bundesregierung, Report, Bundesministerium für Umwelt, Naturschutz und nukleare Sicherheit, 2019. URL: https://www.bmu.de/fileadmin/Daten_BMU/Download_PDF/Klimaschutz/klimaschutzplan_2050_bf.pdf.

[21] J. Speight, 7 - synthetic liquid fuel production from gasification, in: R. Luque, J. G. Speight (Eds.), Gasification for Synthetic Fuel Production, Woodhead Publishing Series in Energy, Woodhead Publishing, 2015, pp. 147–174. doi:10.1016/B978-0-85709-802-3.00007-2.

[22] J. Koornneef, P. van Breevoort, C. Hamelinck, C. Hendriks, M. Hoogwijk, K. Koop, M. Koper, T. Dixon, A. Camps, Global potential for biomass and carbon dioxide capture, transport and storage up to 2050, International Journal of Greenhouse Gas Control 11 (2012) 117–132. doi:10.1016/j.ijggc.2012.07.027.

[23] Choren Industries GmbH, 2nd Generation Biofuel Company Declares Insolvency, Report, Global Agricultural Information Network, 2011.

URL: https://gain.fas.usda.gov/Recent%20GAIN%20Publications/2nd%20Generation%20Biofuel%20Company%20Declares%20Insolvency_Berlin_Germany_07-13-2011.pdf.

[24] Neste Oil Corporation, Neste Oil and Stora Enso to end their biodiesel project and continue cooperation on other bio products, Press Release, Neste, 2012-08-17. URL: https://www.neste.com/neste-oil-and-stora-enso-end-their-biodiesel-project-and-continue-cooperation-other-bio-products.

[25] Linde Engineering Dresden GmbH, Linde and Forest BtL sign licensing agreement for Carbo-V® technology, Press Release, Linde, 2013-01-24. URL: http://www.linde.com.ve/en/news_and_media/press_releases/news_130125.html.

[26] Board of Directors of Vapo Oy, Vapo Oy freezes the Kemi biodiesel project, Press Release, Vapo Oy, 2014-02-21. URL: https://www.vapo.com/en/media/news/1997/vapo_oy_freezes_the_kemi_biodiesel_project.

[27] Kaidi Finland Media Desk, Kiinalainen Kaidi Suunnittelee miljardin Euron biojalostamao Kemiin, Press Release, Kaidi Finland, 2016-02-10. URL: http://www.kaidi.fi/uutiset-tiedotteet/2015/12/3/tiedote.

[28] P. Koponen, EU: Lta vahva tuki Kemin biojalostamon toteutumiselle, Press Release, Kaidi Finland, 2016-06-23. URL: http://www.kaidi.fi/uutiset-tiedotteet/2016/7/22/eulta-vahva-tuki-kemin-biojalostamon-toteutumiselle.

[29] Fachagentur Nachwachsende Rohstoffe e.V. (FNR), Biofuels, Technical Report, Federal Ministry of Food and Agriculture, 2016. URL: http://www.fnr.de/fileadmin/allgemein/pdf/broschueren/brosch_biofuels_web.pdf.

[30] Fachagentur Nachwachsende Rohstoffe e.V. (FNR), Basisdaten Bioenergie Deutschland 2018, Technical Report, Federal Ministry of Food and Agriculture, 2018. URL: https://www.landwirtschaft.sachsen.de/download/CMS/29_Broschuere_Basisdaten_Bioenergie_2017_2.pdf.

[31] G. J. Lyons, F. Lunny, H. P. Pollock, A procedure for estimating the value of forest fuels, Biomass 8 (1985) 283–300. doi:10.1016/0144-4565(85)90061-7.

[32] J. S. Lee, Clarifying the terms of heating values, Graduate research [non-thesis], University of British Columbia Library, Vancouver, 2017. doi:10.14288/1.0343474.

[33] FAO (Ed.), UBET – Unified Bioenergy Terminology, FAO, 2004, pp. 22, 25. URL: http://www.fao.org/docrep/007/j4504e/j4504e00.htm.

[34] H. Abdullah, D. Mourant, C.-Z. Li, H. Wu, Bioslurry as a fuel. 3. fuel and rheological properties of bioslurry prepared from the bio-oil and biochar of mallee biomass fast pyrolysis, Energy & Fuels 24 (2010) 5669–5676. doi:10.1021/ef1008117.

[35] A. Rimkus, J. Žaglinskis, P. Rapalis, P. Skačkauskas, Research on the combustion, energy and emission parameters of diesel fuel and a biomass-to-liquid (BTL) fuel blend in a compression-ignition engine, Energy Conversion and Management 106 (2015) 1109–1117. doi:10.1016/j.enconman.2015.10.047.

[36] A. Bridgwater, D. Meier, D. Radlein, An overview of fast pyrolysis of biomass, Organic Geochemistry 30 (1999) 1479–1493. doi:10.1016/S0146-6380(99)00120-5.

[37] P. de Wild, H. Reith, E. Heeres, Biomass pyrolysis for chemicals, Biofuels 2 (2011) 185–208. doi:10.4155/bfs.10.88.

[38] C. Pfitzer, N. Dahmen, N. Tröger, F. Weirich, J. Sauer, A. Günther, M. Müller-Hagedorn, Fast pyrolysis of wheat straw in the bioliq pilot plant, Energy & Fuels 30 (2016) 8047–8054. doi:10.1021/acs.energyfuels.6b01412.

[39] A. Funke, E. Henrich, N. Dahmen, J. Sauer, Dimensional analysis of auger-type fast pyrolysis reactors, Energy Technology 5 (2017) 119–129. doi:10.1002/ente.201600095.

[40] E. Henrich, N. Dahmen, F. Weirich, R. Reimert, C. Kornmayer, Fast pyrolysis of lignocellulosics in a twin screw mixer reactor, Fuel Processing Technology 143 (2016) 151–161. doi:10.1016/j.fuproc.2015.11.003.

[41] N. Dahmen, E. Dinjus, T. Kolb, U. Arnold, H. Leibold, R. Stahl, State of the art of the bioliq process for synthetic biofuels production, Environmental Progress & Sustainable Energy 31 (2012) 176–181. doi:10.1002/ep.10624.

[42] E. Hagen, P. Konst, A. van Horssen, Deliverable 6.5 - Market implementation plan, Technical Report, BioBoost, 2015. URL: http://www.bioboost.eu/uploads/files/bioboost_d6.5_market_implementation_plan_vers1.2-final.pdf.

[43] H. Gruber, P. Groß, R. Rauch, A. Reichhold, R. Zweiler, C. Aichernig, S. Müller, N. Ataimisch, H. Hofbauer, Fischer-tropsch products from biomass-derived syngas and renewable hydrogen, Biomass Conversion and Biorefinery (2019) 1–12. doi:10.1007/s13399-019-00459-5.

[44] C. Boyer, J. Gazarian, V. Lecocq, S. Maury, A. Forret, J.-M. Schweitzer, V. Souchon, Development of the fischer-tropsch process: From the reaction concept to the process book, Oil & Gas Science and Technology 71 (2016) 44. doi:10.2516/ogst/2015032.

[45] Helmholtz Virtual Institute for Gasification Technology, available at http://www.hvigastech.org/, accessed: July 6, 2020.

[46] T. Kolb, M. Aigner, R. Kneer, M. Mueller, R. Weber, N. Djordjevic, Tackling the challenges in modelling entrained-flow gasification of low-grade feedstock, Journal of the Energy Institute 89 (2016) 485–503. doi:10.1016/j.joei.2015.07.007.

[47] E. Henrich, N. Dahmen, A. Niebel, Deliverable 5.8 - Study on energy carrier use for entrained flow gasification, Technical Report, BioBoost, 2015. URL: http://www.bioboost.eu/uploads/files/bioboost_d5.8_study_on_energy_carrier_use_for_entrained_flow_gasification_vers1.0-final.pdf.

[48] Y. Zhu, H. Frey, 3 - Integrated gasification combined cycle (IGCC) power plant design and technology, in: D. Roddy (Ed.), Advanced Power Plant Materials, Design and Technology, Woodhead Publishing Series in Energy, Woodhead Publishing, 2010, pp. 54–88. doi:10.1533/9781845699468.1.54.

[49] B. Wang, Z. Zhu, A brief report and analysis on the july 19, 2019, explosion in the Yima gasification plant in Sanmenxia, China, Process Safety Progress (2019) 5. doi:10.1002/prs.12095.

[50] C. Higman, State of the gasification industry - the updated worldwide gasification database, Annual International Pittsburgh Coal Conference 2013, PCC 30 (2013) 226–247.

[51] A. Lefebvre, V. McDonell, Atomization and Sprays, Second edition, CRC Press, Boca Raton, 2017. doi:10.1201/9781315120911.

[52] J. Shinjo, Recent advances in computational modeling of primary atomization of liquid fuel sprays, Energies 11 (2018) 2971. doi:10.3390/en11112971.

[53] E. Berrocal, Multiple scattering of light in optical diagnostics of dense sprays and other complex turbid media, Ph.D. thesis, Cranfield University, Cranfield, 2006. URL: http://hdl.handle.net/1826/3983.

[54] M. Z. v. Krzywoblocki, Jets–review of literature, Journal of Jet Propulsion 26 (1956) 760–779. doi:10.2514/8.7138.

[55] E. Giffen, A. Muraszew, The Atomisation of Liquid Fuels, Chapman & Hall Lond, London, 1953.

[56] C. Habchi, The energy spectrum analogy breakup (sab) model for the numerical simulation of sprays, Atomization and Sprays 21 (2011) 1033–1057. doi:10.1615/AtomizSpr.2012004531.

[57] A. Bensakhria, A. Quignard, P. A, B. F, Rheological characterisation of biomass fast pyrolysis oil, in: Proceedings of the 18th European Biomass Conference and Exhibition, Lyon, France, 2010, pp. 977–980. doi:10.5071/18thEUBCE2010-VP2.3.7.

[58] T. Jakobs, N. Djordjevic, S. Fleck, M. Mancini, R. Weber, T. Kolb, Gasification of high viscous slurry R&D on atomization and numerical simulation, Applied Energy 93 (2012) 449–456. doi:10.1016/j.apenergy.2011.12.026.

[59] T. Jakobs, Einfluss des Reaktordrucks auf die Spraygüte außenmischender Zweistoffdüsen, Ph.D. thesis, Fakultät für Chemieingenieurwesen und Verfahrenstechnik des Karlsruher Institut für Technologie (KIT), Karlsruhe, 2015. doi:10.5445/IR/1000048862.

[60] T. Jakobs, N. Djordjevic, S. Fleck, N. Zarzalis, T. Kolb, Influence of ambient pressure on twin fluid atomization - R&D work for high pressure entrained flow gasification, in: Proceedings of the 12th International Conference on Liquid Atomization and Spray Systems, Heidelberg, Germany, 2012, p. 1122.

[61] T. Sfetsas, C. Michailof, A. Lappas, Q. Li, B. Kneale, Qualitative and quantitative analysis of pyrolysis oil by gas chromatography with flame ionization detection and comprehensive two-dimensional gas chromatography with time-of-flight mass spectrometry, Journal of Chromatography A 1218 (2011) 3317–3325. doi:10.1016/j.chroma.2010.10.034.

[62] A. Oasmaa, D. Meier, Norms and standards for fast pyrolysis liquids: 1. round robin test, Journal of Analytical and Applied Pyrolysis 73 (2005) 323–334. doi:10.1016/j.jaap.2005.03.003.

[63] C. Mullen, A. Boateng, N. M. Goldberg, I. Lima, D. A. Laird, K. B. Hicks, Bio-oil and bio-char production from corn cobs and stover by fast pyrolysis, Biomass and Bioenergy 34 (2010) 67–74. doi:10.1016/j.biombioe.2009.09.012.

[64] D. Meier, New methods for chemical and physical characterization and round robin testing, in: Fast Pyrolysis of Biomass: A Handbook, volume 1, CPL Press, United Kingdom, 1999, pp. 92–101. URL: https://books.google.de/books?id=ofYNAQAACAAJ.

[65] P. R. Patwardhan, Understanding the product distribution from biomass fast pyrolysis, Ph.D. thesis, Iowa State University, Iowa, 2010. URL: https://lib.dr.iastate.edu/etd/11767.

[66] J. M. Piskorz, P. D. Radlein, Pyrolysis of biomass–aerosol generation: Properties, applications and significance for process engineers, in: Proceedings of the 4th biomass conference of the Americas, Oakland, United States, 1999, p. 1153–1159.

[67] R. J. Evans, T. A. Milne, Molecular characterization of the pyrolysis of biomass, Energy & Fuels 1 (1987) 123–137. doi:10.1021/ef00002a001.

[68] P. R. Patwardhan, R. C. Brown, B. H. Shanks, Understanding the fast pyrolysis of lignin, ChemSusChem 4 (2011) 1629–1636. doi:10.1002/cssc.201100133.

[69] Y. Chhiti, S. Salvador, J.-M. Commandré, F. Broust, Thermal decomposition of bio-oil: Focus on the products yields under different pyrolysis conditions, Fuel 102 (2012) 274–281. doi:10.1016/j.fuel.2012.06.098.

[70] Y. Chhiti, S. Salvador, J.-M. Commandré, F. Broust, C. Couhert, Wood bio-oil noncatalytic gasification: Influence of temperature, dilution by an

alcohol and ash content, Energy & Fuels 25 (2011) 345–351. doi:10.1021/ef101247m.

[71] M. J. Wornat, B. G. Porter, N. Y. C. Yang, single droplet combustion of biomass pyrolysis oils, Energy & Fuels 8 (1994) 1131–1142. doi:10.1021/ef00047a018.

[72] Y. Solantausta, N.-O. Nylund, M. Westerholm, T. Koljonen, A. Oasmaa, Wood-pyrolysis oil as fuel in a diesel-power plant, Bioresource Technology 46 (1993) 177–188. doi:10.1016/0960-8524(93)90071-I.

[73] A. Shihadeh, S. Hochgreb, Diesel engine combustion of biomass pyrolysis oils, Energy & Fuels 14 (2000) 260–274. doi:10.1021/ef990044x.

[74] S. Gros, Pyrolysis oil as diesel fuel, in: Proceedings of the Seminar on Power Production from Biomass II, Espoo, Finland, 1995, p. 225–238.

[75] A. Williams, Fundamentals of oil combustion, Progress in Energy and Combustion Science 2 (1976) 167–179. doi:10.1016/0360-1285(76)90011-3.

[76] A. R. Teixeira, R. J. Hermann, J. S. Kruger, W. J. Suszynski, L. D. Schmidt, D. P. Schmidt, P. J. Dauenhauer, Microexplosions in the upgrading of biomass-derived pyrolysis oils and the effects of simple fuel processing, ACS Sustainable Chemistry & Engineering 1 (2013) 341–348. doi:10.1021/sc300148b.

[77] R. Calabria, F. Chiariello, P. Massoli, Combustion fundamentals of pyrolysis oil based fuels, Experimental Thermal and Fluid Science 31 (2007) 413–420. doi:10.1016/j.expthermflusci.2006.04.010.

[78] J. D'Alessio, M. Lazzaro, P. Massoli, V. Moccia, Thermo-optical investigation of burning biomass pyrolysis oil droplets, Symposium (International) on Combustion 27 (1998) 1915–1922. doi:10.1016/S0082-0784(98)80035-0.

[79] C. K. Law, Internal boiling and superheating in vaporizing multicomponent droplets, AIChE Journal 24 (1978) 626–632. doi:10.1002/aic.690240410.

[80] P. Stoesser, J. Ruf, R. Gupta, N. Djordjevic, T. Kolb, Contribution to the understanding of secondary pyrolysis of biomass-based slurry under entrained-flow gasification conditions, Energy & Fuels 30 (2016) 6448–6457. doi:10.1021/acs.energyfuels.6b00935.

[81] L. Smoot, P. Smith, Coal Combustion and Gasification, The Plenum Chemical Engineering Series, Springer US, 1985. doi:10.1007/978-1-4757-9721-3.

[82] T. H. Fletcher, 6 - gasification fundamentals, in: T. Wang, G. Stiegel (Eds.), Integrated Gasification Combined Cycle (IGCC) Technologies, Woodhead Publishing, 2017, pp. 223–256. doi:10.1016/B978-0-08-100167-7.00006-8.

[83] M. de Souza-Santos, Solid Fuels Combustion and Gasification: Modeling, Simulation, and Equipment Operations, Mechanical Engineering, CRC Press, 2004. doi:10.1201/9781420047509.

[84] J. G. Speight, Chapter 3 - gasifier types, in: J. G. Speight (Ed.), Gasification of Unconventional Feedstocks, Gulf Professional Publishing, Boston, 2014, pp. 54–90. doi:10.1016/B978-0-12-799911-1.00003-0.

[85] A. Tremel, H. Spliethoff, Gasification kinetics during entrained flow gasification – Part II: Intrinsic char reaction rate and surface area development, Fuel 107 (2013) 653–661. doi:10.1016/j.fuel.2012.10.053.

[86] P. Walker, F. Rusinko, L. Austin, Gas reactions of carbon, in: D. Eley, P. Selwood, P. B. Weisz (Eds.), Advances in Catalysis, volume 11, Academic Press, 1959, pp. 133–221. doi:10.1016/S0360-0564(08)60418-6.

[87] N. M. Laurendeau, Heterogeneous kinetics of coal char gasification and combustion, Progress in Energy and Combustion Science 4 (1978) 221–270. doi:10.1016/0360-1285(78)90008-4.

[88] N. Slavinskaya, U. Riedel, V. Messerle, A. Ustimenko, Chemical kinetic modeling in coal gasification processes: an overview, Eurasian Chemico-Technological Journal 15 (2013) 1–18. doi:10.18321/ectj134.

[89] A. Tremel, H. Spliethoff, Gasification kinetics during entrained flow gasification – Part III: Modelling and optimisation of entrained flow gasifiers, Fuel 107 (2013) 170–182. doi:10.1016/j.fuel.2013.01.062.

[90] O. Maurstad, An Overview of Coal Based Integrated Gasification Combined Cycle (IGCC) Technology, Technical Report, Massachusetts Institute of Technology - Laboratory for Energy and the Environment, 2005. URL: http://sequestration.mit.edu/pdf/LFEE_2005-002_WP.pdf.

[91] D. Brooker, Chemistry of deposit formation in a coal gasification syngas cooler, Fuel 72 (1993) 665–670. doi:10.1016/0016-2361(93)90579-Q.

[92] C. Higman, M. van der Burgt, Gasification, Gulf Professional Publishing, Burlington, 2003. doi:10.1016/B978-0-7506-7707-3.X5000-1.

[93] G. Urbain, Viscosity estimation of slags, Steel research 58 (1987) 111–116. doi:10.1002/srin.198701513.

[94] S. V. Vassilev, D. Baxter, L. K. Andersen, C. G. Vassileva, An overview of the composition and application of biomass ash. Part 1. phase–mineral and chemical composition and classification, Fuel 105 (2013) 40–76. doi:10.1016/j.fuel.2012.09.041.

[95] S. Seebold, M. Eberhard, G. Wu, E. Yazhenskikh, D. Sergeev, T. Kolb, M. Müller, Thermophysical and chemical properties of bioliq slags, Fuel 197 (2017) 596–604. doi:10.1016/j.fuel.2017.02.027.

[96] E. Yazhenskikh, T. Jantzen, K. Hack, M. Müller, A new multipurpose thermodynamic database for oxide systems, Melts (2019) 116–124. doi:10.1134/S0235010619010237.

[97] S. Fleck, U. Santo, C. Hotz, T. Jakobs, G. Eckel, M. Mancini, R. Weber, T. Kolb, Entrained flow gasification Part 1: Gasification of glycol in an atmospheric-pressure experimental rig, Fuel 217 (2018) 306–319. doi:10.1016/j.fuel.2017.12.077.

[98] T. Kathrotia, C. Naumann, P. Oßwald, M. Köhler, U. Riedel, Kinetics of ethylene glycol: The first validated reaction scheme and first measurements of ignition delay times and speciation data, Combustion and Flame 179 (2017) 172–184. doi:10.1016/j.combustflame.2017.01.018.

[99] S. Hafner, Modellentwicklung zur numerischen Simulation eines Flugstromvergasers für Biomasse, Ph.D. thesis, Ruprechts-Karls-Universität Heidelberg, Heidelberg, 2010. doi:10.11588/heidok.00011309.

[100] M. Mancini, M. Alberti, M. Dammann, U. Santo, G. Eckel, T. Kolb, R. Weber, Entrained flow gasification. Part 2: Mathematical modeling of the gasifier using rans method, Fuel 225 (2018) 596–611. doi:10.1016/j.fuel.2018.03.100.

[101] G. Eckel, P. L. Clercq, T. Kathrotia, A. Saenger, S. Fleck, M. Mancini, T. Kolb, M. Aigner, Entrained flow gasification. Part 3: Insight into the injector near-field by large eddy simulation with detailed chemistry, Fuel 223 (2018) 164–178. doi:10.1016/j.fuel.2018.02.176.

[102] M. Dammann, M. Mancini, S. Fleck, R. Weber, T. Kolb, Entrained flow gasification: experiments and mathematical modelling based on RANS, in: Proceedings of the 29th Deutscher Flammentag, Bochum, Germany, VDI-Berichte, 2019, p. 8. Not yet published.

[103] S. C. Hill, L. D. Smoot, A comprehensive three-dimensional model for simulation of combustion systems. PCGC-3, Energy & Fuels 7 (1993) 874–883. doi:10.1021/ef00042a025.

[104] M. Kumar, A. F. Ghoniem, Multiphysics simulations of entrained flow gasification. Part II: Constructing and validating the overall model, Energy & Fuels 26 (2012) 464–479. doi:10.1021/ef2008858.

[105] N. Abani, A. F. Ghoniem, Large eddy simulations of coal gasification in an entrained flow gasifier, Fuel 104 (2013) 664–680. doi:10.1016/j.fuel.2012.06.006.

[106] J. Ma, S. E. Zitney, Computational fluid dynamic modeling of entrained-flow gasifiers with improved physical and chemical submodels, Energy & Fuels 26 (2012) 7195–7219. doi:10.1021/ef301346z.

[107] J. Warnatz, U. Maas, R. Dibble, Combustion: Physical and Chemical Fundamentals, Modeling and Simulation, Experiments, Pollutant Formation, 2006. doi:10.1007/978-3-540-45363-5.

[108] T. Poinsot, D. Veynante, Theoretical and Numerical Combustion, Second edition, Edwards, 2005.

[109] V. Toro, A. Mokhov, H. Levinsky, M. Smooke, Combined experimental and computational study of laminar, axisymmetric hydrogen–air diffusion flames, Proceedings of the Combustion Institute 30 (2005) 485 – 492. doi:10.1016/j.proci.2004.08.221.

[110] P. W. Marinov N.M., Westbrook C.K., Detailed and global chemical kinetics model for hydrogen, in: Proceedings of the 8th symposium on transport properties, San Francisco, United States, Lawrence Livermore National Laboratory, 1995, pp. 118–129. URL: https://digital.library.unt.edu/ark:/67531/metadc794810/.

[111] O. Reynolds, XXIX. An experimental investigation of the circumstances which determine whether the motion of water shall be direct or sinuous, and of the law of resistance in parallel channels, Philosophical Transactions of the Royal Society of London 174 (1883) 935–982. doi:10.1098/rstl.1883.0029.

[112] A. N. Kolmogorov, The Local Structure of Turbulence in Incompressible Viscous Fluid for Very Large Reynolds' Numbers, Doklady Akademii Nauk SSSR 30 (1941) 299–303.

[113] S. B. Pope, Turbulent Flows, Cambridge University Press, Cambridge, 2000. doi:10.1017/CBO9780511840531.

[114] O. Reynolds, IV. On the dynamical theory of incompressible viscous fluids and the determination of the criterion, Philosophical Transactions of the Royal Society of London 186 (1895) 123–164. doi:10.1098/rsta.1895.0004.

[115] P. Gerlinger, Investigation of an assumed pdf approach for finite-rate chemistry, Combustion Science and Technology 175 (2003) 841–872. doi:10.1080/00102200302410.

[116] S. Pope, PDF methods for turbulent reactive flows, Progress in Energy and Combustion Science 11 (1985) 119–192. doi:10.1016/0360-1285(85)90002-4.

[117] M. Ishii, Thermo-fluid dynamic theory of two-phase flow, Eyrolles, Paris, 1975.

[118] D. A. Drew, Mathematical modeling of two-phase flow, Annual Review of Fluid Mechanics 15 (1983) 261–291. doi:10.1146/annurev.fl.15.010183.001401.

[119] M. Baer, J. Nunziato, A two-phase mixture theory for the deflagration-to-detonation transition (ddt) in reactive granular materials, International Journal of Multiphase Flow 12 (1986) 861–889. doi:10.1016/0301-9322(86)90033-9.

[120] R. Saurel, R. Abgrall, A multiphase godunov method for compressible multifluid and multiphase flows, Journal of Computational Physics 150 (1999) 425–467. doi:10.1006/jcph.1999.6187.

[121] G. Allaire, S. Clerc, S. Kokh, A five-equation model for the simulation of interfaces between compressible fluids, Journal of Computational Physics 181 (2002) 577 – 616. doi:10.1006/jcph.2002.7143.

[122] H. Rusche, Computational Fluid Dynamics of Dispersed Two-phase Flows at High Phase Fractions, Ph.D. thesis, University of London, London, 2002. URL: https://spiral.imperial.ac.uk/handle/10044/1/8110.

[123] C. Dopazo, On conditioned averages for intermittent turbulent flows, Journal of Fluid Mechanics 81 (1977) 433–438. doi:10.1017/S0022112077002158.

[124] H. Marschall, Towards the Numerical Simulation of Multi-Scale Two-Phase Flows, Ph.D. thesis, Technische Universität München, München, 2011. URL: http://mediatum.ub.tum.de?id=1080878.

[125] D. P. Hill, The computer simulation of dispersed two-phase flow, Ph.D. thesis, University of London, London, 1998. URL: https://spiral.imperial.ac.uk/handle/10044/1/8733.

[126] S. Politis, Prediction of Two-Phase Solid-Liquid Turbulent Flow in Stirred Vessels, Ph.D. thesis, University of London, London, 1989. URL: https://spiral.imperial.ac.uk/handle/10044/1/8708.

[127] P. De Oliveira, Computer modelling of multidimensional flow and application to T-junctions, Ph.D. thesis, University of London, London, 1992. URL: https://spiral.imperial.ac.uk/handle/10044/1/8637.

[128] G. Wallis, D. Drew, Fundamentals of two-phase flow modeling, Multiphase Science and Technology 8 (1994) 1–67. doi:DOI:10.1615/MultScienTechn.v8.i1-4.20.

[129] I. Kataoka, A. Serizawa, Basic equations of turbulence in gas-liquid two-phase flow, International Journal of Multiphase Flow 15 (1989) 843–855. doi:10.1016/0301-9322(89)90045-1.

[130] H. G. Weller, Derivation, modelling and solution of the conditionally averaged two-phase flow equations, Technical Report TR/HGW/02, Nabla Ltd, 2002.

[131] J. P. Boris, D. L. Book, Flux-corrected transport. I. SHASTA, a fluid transport algorithm that works, Journal of Computational Physics 11 (1973) 38–69. doi:10.1016/0021-9991(73)90147-2.

[132] S. T. Zalesak, Fully multidimensional flux-corrected transport algorithms for fluids, Journal of Computational Physics 31 (1979) 335–362. doi:10.1016/0021-9991(79)90051-2.

[133] S. Márquez Damián, An Extended Mixture Model for the Simultaneous Treatment of Short and Long Scale Interfaces, Ph.D. thesis, Universidad Nacional del Litoral, Argentina, 2013. doi:10.13140/RG.2.1.3182.8320.

[134] W. Sirignano, Fluid Dynamics and Transport of Droplets and Sprays, Cambridge University Press, Cambridge, 1999. doi:10.1017/CBO9780511529566.

[135] C. Law, Recent advances in droplet vaporization and combustion, Progress in Energy and Combustion Science 8 (1982) 171–201. doi:10.1016/0360-1285(82)90011-9.

[136] D. Spalding, The combustion of liquid fuels, in: Proceedings of the 4th Symposium (International) on Combustion, Massachusetts Institute of Technology Cambridge, Massachusetts, 1953, pp. 847–864. doi:10.1016/S0082-0784(53)80110-4.

[137] R. L. Rowley, W. V. Wilding, J. Oscarson, Y. Yang, N. Zundel, T. Daubert, R. Danner, DIPPR® Data Compilation of Pure Chemical Properties, Design Institute for Physical Properties, AIChE, New York, 2010.

[138] N. Frössling, Atomic Energy Research Establishment, The Evaporation of Falling Drops, U.K.A.E.A. Research Group, Atomic Energy Research Establishment, Harwell, Oxfordshire, 1963.

[139] G. Hubbard, V. Denny, A. Mills, Droplet evaporation: Effects of transients and variable properties, International Journal of Heat and Mass Transfer 18 (1975) 1003–1008. doi:10.1016/0017-9310(75)90217-3.

[140] C. K. Law, H. K. Law, Quasi-steady diffusion flame theory with variable specific heats and transport coefficients, Combustion Science and Technology 12 (1976) 207–216. doi:10.1080/00102207608946722.

[141] W. E. Ranz, W. R. Marshall, Evaporation from drops, Chemical Engineering Progress 48 (1952) 173–180.

[142] L. Shiller, A. Naumann, A drag coefficient correlation, Zeitschrift des Vereins Deutscher Ingenieure 77 (1935) 318–320.

[143] Q. Fradet, N. Fernando, M. Braun-Unkhoff, U. Riedel, Numerische Untersuchung der Flugstromvergasung mit einem Euler-Euler ansatz, in: Proceedings of the 29th Deutscher Flammentag, Bochum, Germany, VDI-Berichte, 2019, p. 7. Not yet published.

[144] A. Burns, T. Frank, I. Hamill, J.-M. Shi, The favre averaged drag model for turbulent dispersion in eulerian multi-phase flows, in: 5th International Conference on Multiphase Flow, ICMF 04 paper No. 392, Yokohama, Japan, volume 392, 2004, pp. 1–17.

[145] Q. Fradet, M. Braun-Unkhoff, U. Riedel, A sectional approach for the entrained-flow gasification of slurry fuels, Energy & Fuels 32 (2018) 12532–12544. doi:10.1021/acs.energyfuels.8b02785.

[146] F. Gelbard, J. H. Seinfeld, Simulation of multicomponent aerosol dynamics, Journal of Colloid and Interface Science 78 (1980) 485–501. doi:10.1016/0021-9797(80)90587-1.

[147] C. J. Pope, J. B. Howard, Simultaneous particle and molecule modeling (SPAMM): An approach for combining sectional aerosol equations and elementary gas-phase reactions, Aerosol Science and Technology 27 (1997) 73–94. doi:10.1080/02786829708965459.

[148] T. Blacha, M. D. Domenico, P. Gerlinger, M. Aigner, Soot predictions in premixed and non-premixed laminar flames using a sectional approach for PAHs and soot, Combustion and Flame 159 (2012) 181–193. doi:10.1016/j.combustflame.2011.07.006.

[149] C. Eberle, P. Gerlinger, M. Aigner, A sectional PAH model with reversible PAH chemistry for CFD soot simulations, Combustion and Flame 179 (2017) 63–73. doi:10.1016/j.combustflame.2017.01.019.

[150] T. Lin, E. Goos, U. Riedel, A sectional approach for biomass: Modelling the pyrolysis of cellulose, Fuel Processing Technology 115 (2013) 246–253. doi:10.1016/j.fuproc.2013.03.048.

[151] K. Netzell, H. Lehtiniemi, F. Mauss, Calculating the soot particle size distribution function in turbulent diffusion flames using a sectional method, Proceedings of the Combustion Institute 31 (2007) 667–674. doi:10.1016/j.proci.2006.08.081.

[152] A. D'Anna, Detailed kinetic modeling of particulate formation in rich premixed flames of ethylene, Energy & Fuels 22 (2008) 1610–1619. doi:10.1021/ef700641u.

[153] C. Saggese, N. E. Sánchez, A. Frassoldati, A. Cuoci, T. Faravelli, M. U. Alzueta, E. Ranzi, Kinetic modeling study of polycyclic aromatic hydrocarbons and soot formation in acetylene pyrolysis, Energy & Fuels 28 (2014) 1489–1501. doi:10.1021/ef402048q.

[154] M. D. Domenico, P. Gerlinger, M. Aigner, Development and validation of a new soot formation model for gas turbine combustor simulations, Combustion and Flame 157 (2010) 246–258. doi:10.1016/j.combustflame.2009.10.015.

[155] T. Blacha, M. Di Domenico, M. Koehler, P. Gerlinger, M. Aigner, Soot modeling in a turbulent unconfined C2H4/Air jet flame, AIAA Aerospace Sciences Meeting Including the New Horizons Forum and Aerospace Exposition 49 (2011) 114–124. doi:10.2514/6.2011-114.

[156] C. Eberle, P. Gerlinger, M. Aigner, Large eddy simulations of a sooting lifted turbulent jet-flame, in: Proceedings of the 55th AIAA Aerospace Sciences Meeting, Lyon, Grapevine, Texas, 2017, p. 1785. doi:10.2514/6.2017-1785.

[157] H. Richter, S. Granata, W. H. Green, J. B. Howard, Detailed modeling of PAH and soot formation in a laminar premixed benzene/oxygen/argon low-pressure flame, Proceedings of the Combustion Institute 30 (2005) 1397–1405. doi:10.1016/j.proci.2004.08.088.

[158] J. Moss, I. Aksit, Modelling soot formation in a laminar diffusion flame burning a surrogate kerosene fuel, Proceedings of the Combustion Institute 31 (2007) 3139–3146. doi:10.1016/j.proci.2006.07.016.

[159] S. Fleck, C. Hotz, P. Stoesser, T. Kolb, Gasification of biomass-based suspension fuels in an atmospheric entrained flow gasifier, in: Proceedings of the 27th Deutscher Flammentag, Clausthal-Zellerfeld, Germany, VDI-Berichte 2267, 2015, pp. 207–217.

[160] N. Dahmen, Personal communication, 2016.

[161] J. Heintzenberg, Properties of the log-normal particle size distribution, Aerosol Science and Technology 21 (1994) 46–48. doi:10.1080/02786829408959695.

[162] W. Klose, M. Woelki, On the intrinsic reaction rate of biomass char gasification with carbon dioxide and steam, Fuel 84 (2005) 885–892. doi:10.1016/j.fuel.2004.11.016.

[163] C. Schneider, P. Stoesser, S. Rincon, T. Kolb, Determination of heterogeneous reaction kinetics of high-temperature biomass char, in: Proceedings of the 28th Deutscher Flammentag, Darmstadt, Germany, VDI-Berichte 2302, 2017, pp. 331–343.

[164] I. Bews, A. Hayhurst, S. Richardson, S. Taylor, The order, arrhenius parameters, and mechanism of the reaction between gaseous oxygen and solid carbon, Combustion and Flame 124 (2001) 231–245. doi:10.1016/S0010-2180(00)00199-1.

[165] C. Di Blasi, Combustion and gasification rates of lignocellulosic chars, Progress in Energy and Combustion Science 35 (2009) 121–140. doi:10.1016/j.pecs.2008.08.001.

[166] A. Müller, H. D. Haustein, P. Stoesser, T. Kreitzberg, R. Kneer, T. Kolb, Gasification kinetics of biomass- and fossil-based fuels: Comparison study using fluidized bed and thermogravimetric analysis, Energy & Fuels 29 (2015) 6717–6723. doi:10.1021/acs.energyfuels.5b01123.

[167] A. Lee, C. Law., Gasification and shell characteristics in slurry droplet burning, Combustion and flame 85 (1991) 77–93. doi:10.1016/0010-2180(91)90178-E.

[168] B. J. McBride, S. Gordon, M. A. Reno, Coefficients for calculating thermodynamic and transport properties of individual species, NASA-TM-4513, Technical Report, National Aeronautics and Space Administration, Office of Management, Scientific and Technical Information Program, Washington, DC, 1993. URL: https://ntrs.nasa.gov/search.jsp?R=19940013151.

[169] J. Speight, Handbook of Coal Analysis, Chemical Analysis: A Series of Monographs on Analytical Chemistry and Its Applications, John Wiley & Sons, Ltd, 2015. doi:10.1002/9781119037699.

[170] D. Merrick, Mathematical models of the thermal decomposition of coal: 2. specific heats and heats of reaction, Fuel 62 (1983) 540–546. doi:10.1016/0016-2361(83)90223-5.

[171] N. Y. Kirov, Specific heats and total heat contents of coals and related materials at elevated temperatures, British Coal Utilization Research Association, Monthly Bulletin 29 (1965) 33–57.

[172] D. van Krevelen, Coal: Typology, Chemistry, Physics, Constitution, Elsevier Publishing Company, Amsterdam, 1961.

[173] S. Postrzednik, Analiza termodynamiczna procesu odgazowania paliw stałych, Ph.D. thesis, Silesian University of Technology, Gliwice, Poland, 1981.

[174] A. Einstein, Die plancksche theorie der strahlung und die theorie der spezifischen wärme, Annalen der Physik 327 (1907) 180–190. doi:10.1002/andp.19063270110.

[175] A. T. D. Butland, R. J. Maddison, The specific heat of graphite: An evaluation of measurements, Journal of Nuclear Materials 49 (1973) 45–56. doi:10.1016/0022-3115(73)90060-3.

[176] M. W. Chase, National Institute of Standards and Technology (U.S.), NIST-JANAF Thermochemical Tables, 4th Edition, Journal of Physical and Chemical Reference Data Monographs, American Chemical Society, Washington DC and American Institute of Physics for the National Institute of Standards and Technology, Woodbury, 1998. doi:10.18434/T42S31.

[177] K. Kelley, Contributions to the Data on Theoretical Metallurgy: II. High-temperature specific-heat equations for inorganic substances, Technical Report, Bulletin 371, Bureau of Mines, U.S. Government Printing Office, 1934. URL: https://digital.library.unt.edu/ark:/67531/metadc12540/.

[178] W. Eisermann, P. Johnson, W. Conger, Estimating thermodynamic properties of coal, char, tar and ash, Fuel Processing Technology 3 (1980) 39–53. doi:10.1016/0378-3820(80)90022-3.

[179] The OpenFOAM Foundation, available at http://openfoam.org, accessed: July 6, 2020.

[180] T. Methling, M. Braun-Unkhoff, U. Riedel, A novel linear transformation model for the analysis and optimisation of chemical kinetics, Combustion Theory and Modelling 21 (2017) 503–528. doi:10.1080/13647830.2016.1251616.

[181] P. Cheng, Two-dimensional radiating gas flow by a moment method, AIAA Journal 2 (1964) 1662–1664. doi:10.2514/3.2645.

[182] Q. Fradet, N. Fernando, M. Braun-Unkhoff, U. Riedel, Cfd simulation of bio-slurry gasification using a sectional approach, in: Proceedings of the 26th European Biomass Conference and Exhibition, Copenhagen, Denmark, 2018, pp. 753–759. doi:10.5071/26thEUBCE2018-2CV.4.16.

[183] R. L. Rowley, W. V. Wilding, J. Oscarson, Y. Yang, N. Zundel, T. Daubert, R. Danner, DIPPR® Data Compilation of Pure Chemical Properties, Design Institute for Physical Properties, AIChE, New York, 2006.

[184] CARMEN - Centrales Agrar-Rohstoff Marketing- und Energie-Netzwerk, available at www.carmen-ev.de, accessed: July 6, 2020.

[185] H. Boerrigter, Economy of Biomass-to-Liquids (BTL) plants, Technical Report, ECN-C-06-019, Energy research Centre of the Netherlands ECN, Petten (Netherlands), 2006.

[186] E. Searcy, P. Flynn, E. Ghafoori, A. Kumar, The relative cost of biomass energy transport, Applied biochemistry and biotechnology 137-140 (2007) 639–652. doi:10.1007/s12010-007-9085-8.

Appendix A

Gasification cost estimation

The cost for one liter of synthetic fuel (in €/l_{sf}) using a BtL process is shown in Table A.1. It is estimated by splitting the costs into 4 contributions.

- Cost of biomass: the cost for wood residues with 35 % of water was around 70 € in 2019 [184]. The cost per unit decreases when purchased in greater volumes. This was taken into account with a cost decrease relative to the plant size.
- Cost of transport: in 2017, the unused potential of biogenic residues and wastes in Germany was 448 PJ [30]. Half of it was wood residues and one-third straw. With a total surface of 357,386 km^2, it gives the average biomass availability per year and per square kilometer. We can further calculate the mean distance from where biomass has to be conveyed. The transport cost has two costs, the **D**istance **V**ariable **C**ost (**DVC**) and the **D**istance **F**ixed **C**ost (**DFC**).
- Cost of conversion: this cost is the most difficult to estimate because it depends directly of the process chosen and its conditions. However, it is clear that scaling up decreases the cost of operation when it is brought back to 1 liter of fuel. Estimations are given in [185]. It can be seen that scaling up the facility of a factor 10 decreases the conversion cost of a factor 2. The conversion efficiency is also utilized here, with a gasifier efficiency of 80 % and a fuel synthesis efficiency of 71 %.
- Cost of taxes: amounting for 45.03 cent/l_{sf}, the tax on biodiesel is only slightly lower than on regular diesel (47.04 cent/l_{sf}) [29].

TABLE A.1: Estimation of the costs associated to the production of one liter of synthetic fuels

		Plant size		
Biomass input	MW_{th}	10	100	1,000
Synthetic fuel production	bpd	85	850	8,500
Cost of biomass				
Biomass [184]	€/t	70	65	60
Biomass	€/GJ	6	5.6	5.1
Biomass	€/l_{sf}	0.38	0.36	0.33
Cost of transport				
Biomass input	kton/year	1	10	100
Surface needed	km^2	943	9,430	94,300
Mean distance	km	23	73	231
DFC [186]	€/t	3	3	3
DVC [186]	€/t/km	0.08	0.08	0.08
Transport	€/t	4.8	8.8	21.5
Transport	€/GJ	0.41	0.76	1.84
Transport	€/l_{sf}	0.026	0.048	0.12
Cost of conversion				
Conversion [185]	€/GJ_{sf}	20	10	5
Conversion	€/l_{sf}	0.73	0.36	0.18
Cost of taxes				
Taxes [30]	€/l_{sf}	0.4503	0.4503	0.4503

TABLE A.2: Constants used for the costs estimation

Biomass HHV [184]	MJ/kg	18
Biomass water content [184]	$\%_{mass}$	35
Total biomass availability in Germany [30]	PJ/a	448
Total surface of Germany [30]	Mha	35.7
Recovery factor: percentage of available biomass effectively used for this process	%	1
Biomass availability per surface	t/a/km^2	1.1
Road efficiency: ratio of the distance by land transport to the direct distance between points	-	1.2
Gasification conversion efficiency [185]	%	56.8
Energy value of synthetic fuel [185]	GJ_{sf}/l_{sf}	0.0363

Appendix B

Summary of wood and straw char input parameters

TABLE B.1: Input parameters for wood and straw chars

	Straw	Wood
1. Primary char size distribution $[\mu m]$ from [159] and [160]	D_{50} 22.3 μm; D_{84} 40.0 μm	D_{50} 4.5 μm; D_{84} 8.0 μm
2. Primary char size distribution $[g/mol]$ Discretized from 1.	M^{min}_{BIN1} $1.11 \cdot 10^{14}$; M^{max}_{BIN12} $4.54 \cdot 10^{17}$	M^{min}_{BIN1} $9.81 \cdot 10^{11}$; M^{max}_{BIN12} $4.02 \cdot 10^{15}$
3. Primary char proximate analysis $[\%_{mass}]$ From [159]	Moisture 1.9; Volatiles 14.6; C_{fix} 65.6; Ash 17.9	Moisture 4.7; Volatiles 20.0; C_{fix} 73.6; Ash 1.6
4. Primary char ultimate analysis waf $[\%_{mass}]$ From [159]	C 85.59; H 3.92; O 9.12; N, S, Cl 1.363	C 89.68; H 3.19; O 6.45; N, S, Cl 0.686
5. Primary char C, H, O composition af $[\%_{mass}]$ Calculated from 3. and 4.	C 84.8; H 4.1; O 11.1	C 86.0; H 3.6; O 10.4
6. Secondary char C, H, O composition af $[\%_{mass}]$ Approximated from [163]	C 100; H 0; O 0	C 100; H 0; O 0
7. Volatile C, H, O composition $[\%_{mass}]$ Calculated from 3. 5. and 6.	C 24.2; H 20.6; O 55.2	C 44.2; H 14.3; O 41.5
8. Volatile C, H, O composition $[\%_{mol}]$ Converted from 7.	C 7.8; H 78.9; O 13.3	C 18.0; H 69.3; O 12.7
9. Volatile species model Derived from 8.	1 CO; 2 CH_4; 7 H_2; 4 H_2O	1 $C_2H_6O_2$; 1 CO; 2 CH_4; 1 C_2H_2; 4 H_2; 2 H_2O

TABLE B.1 (continued): Input parameters for wood and straw chars

	Straw			Wood		
10. Ash composition $[\%_{mass}]$ Rearranged From [159]	SiO_2 64.4	CaO 9.7	K_2O 25.9	SiO_2 38.8	CaO 36.2	K_2O 25.0
11. Pyrolysis reaction rate r_c^{Pyr} $A_{r,c}^{Pyr} \exp\left(\frac{-E_a^{Pyr}}{RT}\right)$ See section 4.3.2	$A_{r,c}^{Pyr}$ $5,202.5 \cdot \left(\frac{M_{\mathrm{BIN}_6^{1st\,char}}}{M_{\mathrm{BIN}_{c,straw}^{1st\,char}}}\right)^{\frac{1}{3}}$		E_a^{Pyr} $-50,000$	$A_{r,c}^{Pyr}$ $5,202.5 \cdot \left(\frac{M_{\mathrm{BIN}_6^{1st\,char}}}{M_{\mathrm{BIN}_{c,straw}^{1st\,char}}}\right)^{\frac{1}{3}}$		E_a^{Pyr} $-50,000$
12. Gasification reaction rate r_G $A_r^G \exp\left(\frac{-E_a^G}{RT}\right)\left[\mathrm{BIN}_c^{2nd\,char}\right][\mathrm{Ox}]^{0.6}$ See section 4.3.2	A_r^G $4 \cdot 10^8$		E_a^G $-236,000$	A_r^G $1.5 \cdot 10^9$		E_a^G $-236,000$
13. Thermodynamic coefficients primary char b_1 to b_7 low T See section 4.4	165.3 $6.381 \cdot 10^{-3}$ $3.889 \cdot 10^{-9}$ -546.3	1.721 $-9.700 \cdot 10^{-6}$ $-6.525 \cdot 10^6$		157.1 $6.066 \cdot 10^{-3}$ $3.697 \cdot 10^{-9}$ -478.3	1.637 $-9.222 \cdot 10^{-6}$ $-7.656 \cdot 10^5$	
14. Thermodynamic coefficients primary char b_1 to b_7 high T See section 4.4	738.9 $-1.853 \cdot 10^{-3}$ $-5.419 \cdot 10^{-11}$ $-4,309$	3.114 $5.126 \cdot 10^{-7}$ $-6.704 \cdot 10^6$		702.4 $-1.762 \cdot 10^{-3}$ $-5.151 \cdot 10^{-11}$ $-4,055$	2.960 $4.874 \cdot 10^{-7}$ $-4.378 \cdot 10^5$	
15. Thermodynamic coefficients secondary char b_1 to b_7 low T See section 4.4	-525.8 $-3.791 \cdot 10^{-3}$ $3.872 \cdot 10^{-10}$ 1,914	5.210 $4.786 \cdot 10^{-7}$ $-4.241 \cdot 10^4$		-525.8 $-3.791 \cdot 10^{-3}$ $3.872 \cdot 10^{-10}$ 1,914	5.210 $4.786 \cdot 10^{-7}$ $-4.241 \cdot 10^4$	
16. Thermodynamic coefficients secondary char b_1 to b_7 high T See section 4.4	656.6 $-1.062 \cdot 10^{-3}$ $-2.845 \cdot 10^{-11}$ $-3,839$	1.914 $2.797 \cdot 10^{-7}$ $-2.719 \cdot 10^5$		656.6 $-1.062 \cdot 10^{-3}$ $-2.845 \cdot 10^{-11}$ $-3,839$	1.914 $2.797 \cdot 10^{-7}$ $-2.719 \cdot 10^5$	
17. Thermodynamic coefficients ash b_1 to b_7 low T See section 4.4	-132.6 $-1.020 \cdot 10^{-2}$ $-3.074 \cdot 10^{-9}$ -160.4	5.385 $9.182 \cdot 10^{-6}$ $-7.350 \cdot 10^5$		-44.66 $-9.377 \cdot 10^{-3}$ $-2.838 \cdot 10^{-9}$ -512.0	4.902 $8.464 \cdot 10^{-6}$ $-7.457 \cdot 10^5$	
18. Thermodynamic coefficients ash b_1 to b_7 high T See section 4.4	781.9 $-7.338 \cdot 10^{-5}$ $-2.074 \cdot 10^{-12}$ $-3,826$	0.4391 $2.037 \cdot 10^{-8}$ $-8.606 \cdot 10^5$		790.7 $-6.787 \cdot 10^{-5}$ $-1.865 \cdot 10^{-12}$ $-3,854$	0.367 $1.859 \cdot 10^{-8}$ $-8.601 \cdot 10^5$	

Appendix C

CFD contours

C.1 REGA-glycol-T1

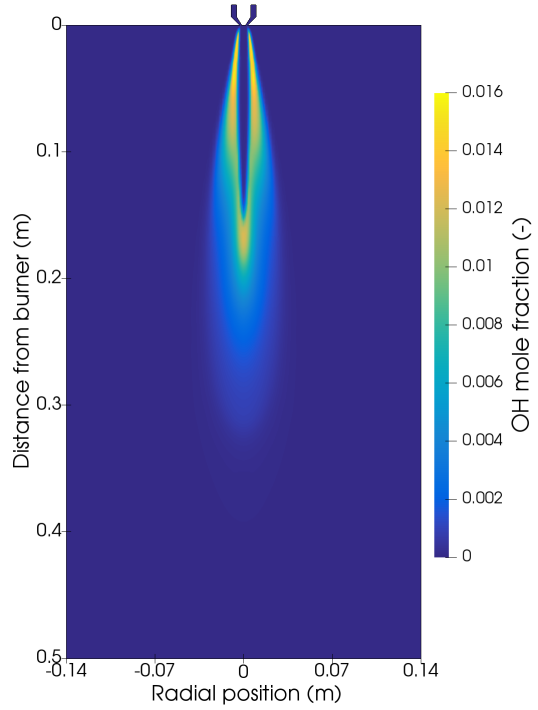

A) Hydroxyl radical mole fraction

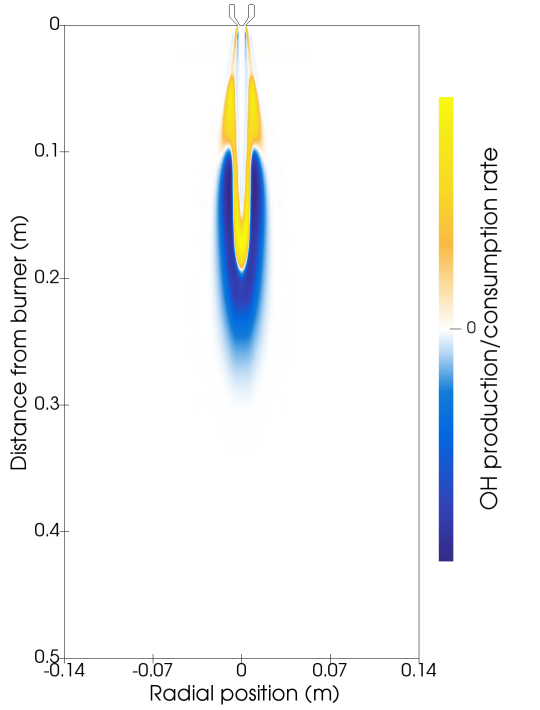

B) Hydroxyl radical reaction rate

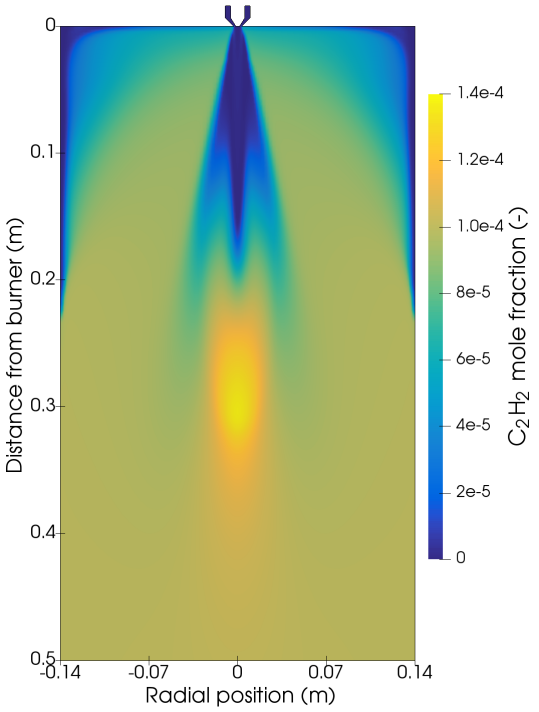

C) Acetylene mole fraction

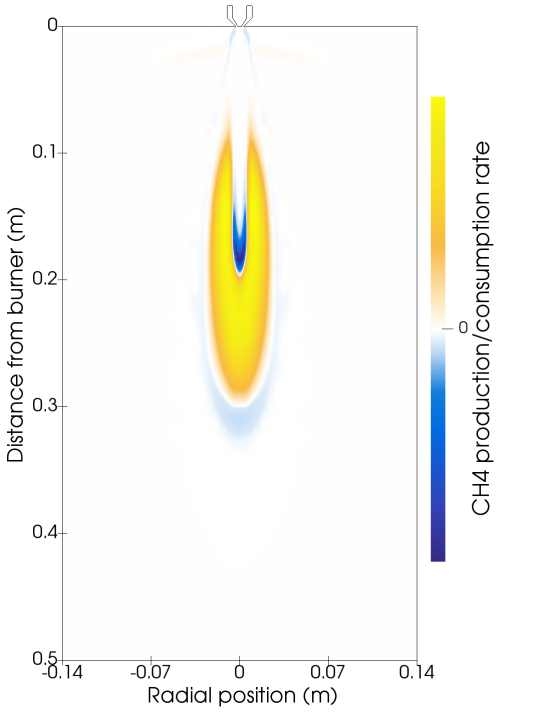

D) Methane reaction rate

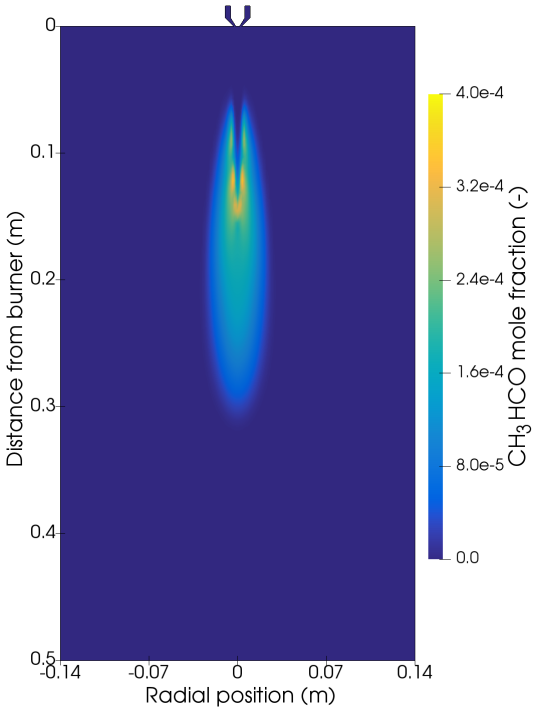

E) Acetaldehyde mole fraction

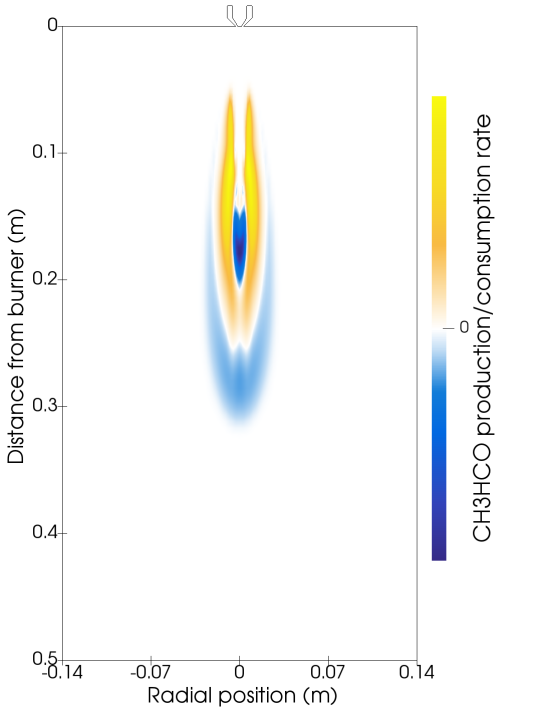

F) Acetaldehyde reaction rate

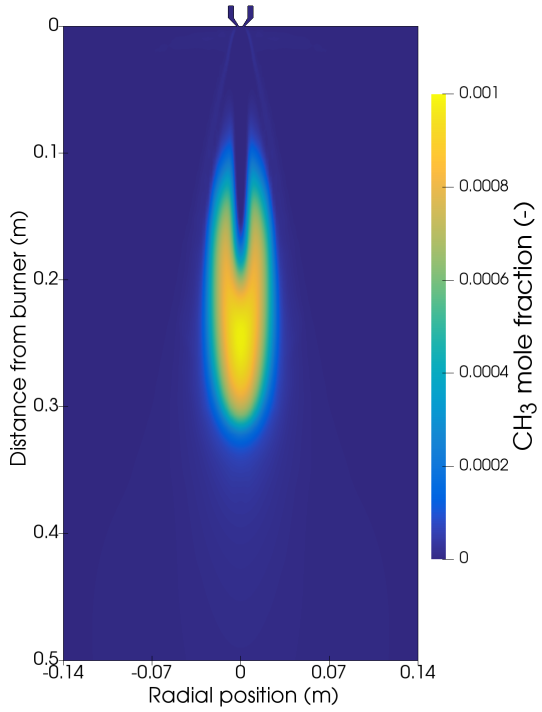

G) Methyl radical mole fraction

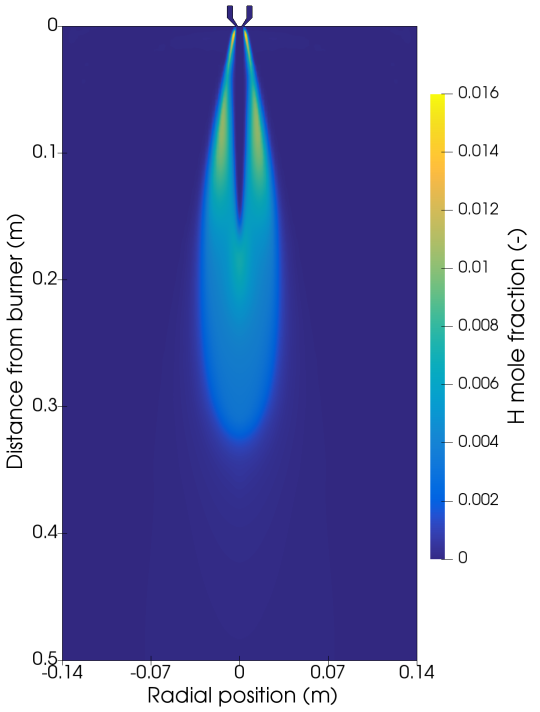

H) Hydrogen radical mole fraction

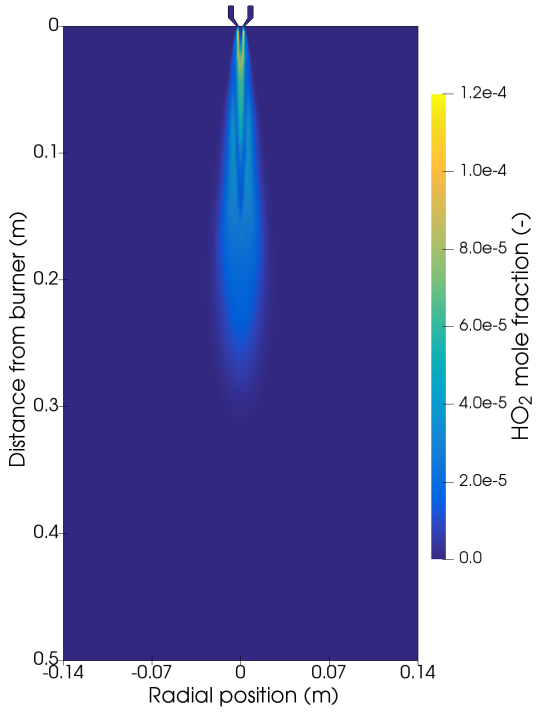

I) Hydroperoxyl radical mole fraction

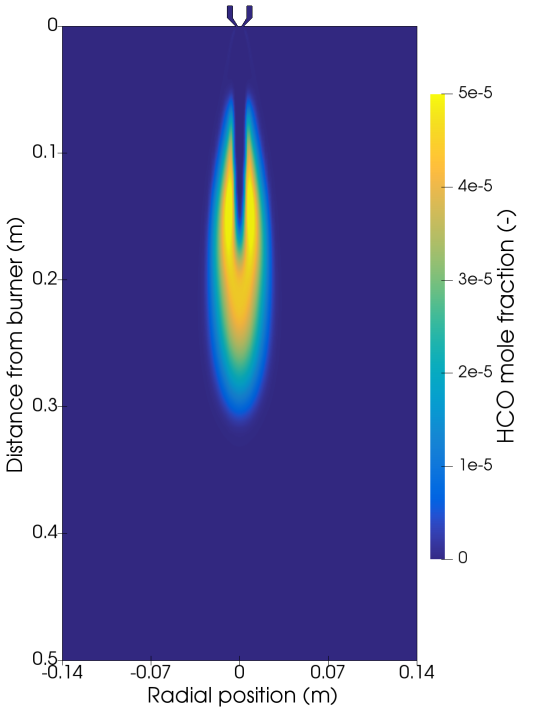

J) Formyl radical mole fraction

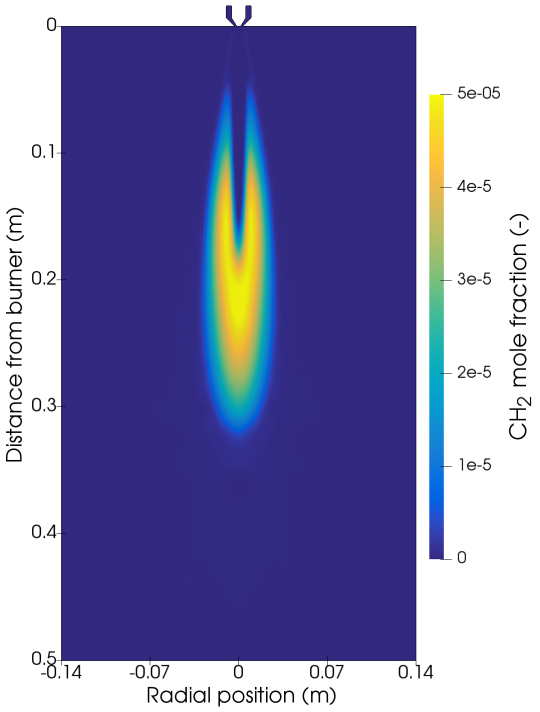

K) Methylene radical mole fraction

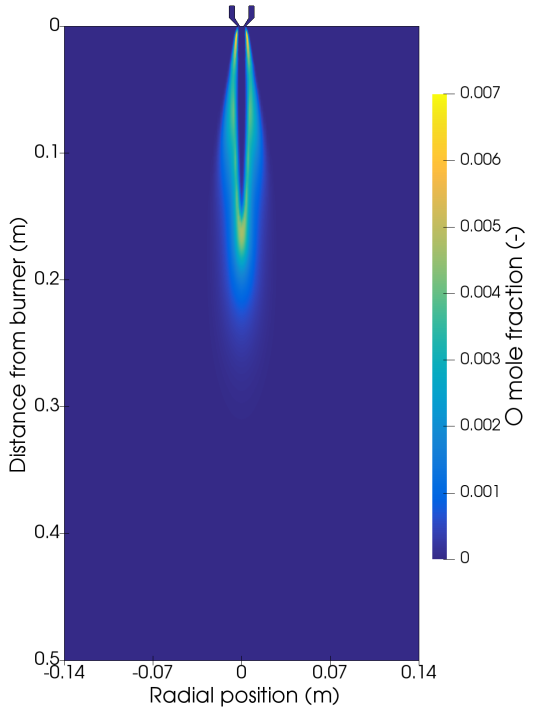

L) O radical mole fraction

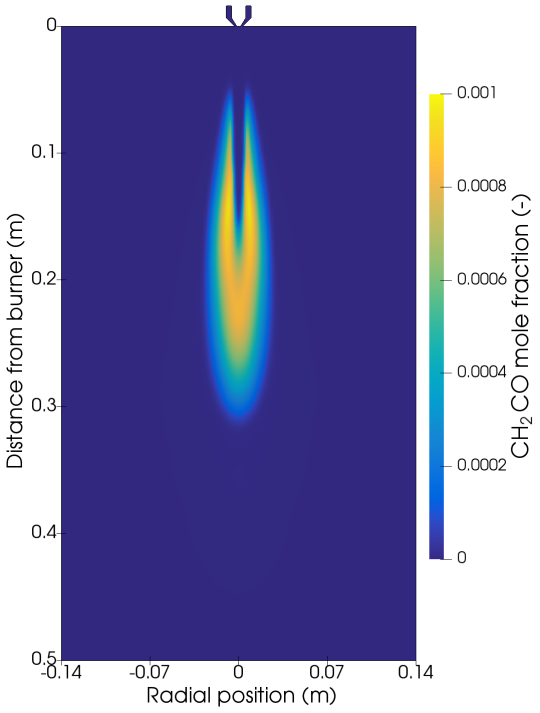

M) Ketene mole fraction

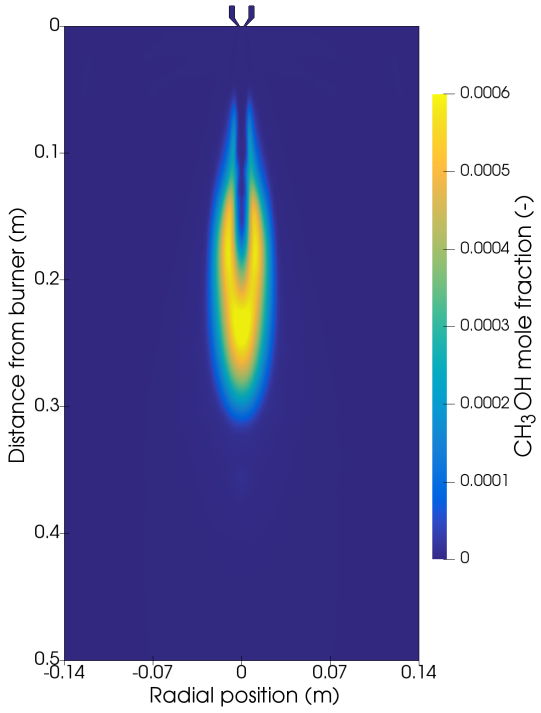

N) Methanol mole fraction

FIGURE C.1: CFD contours of the gas phase for the data set REGA-glycol-T1

C.2 REGA-slurry1-T2

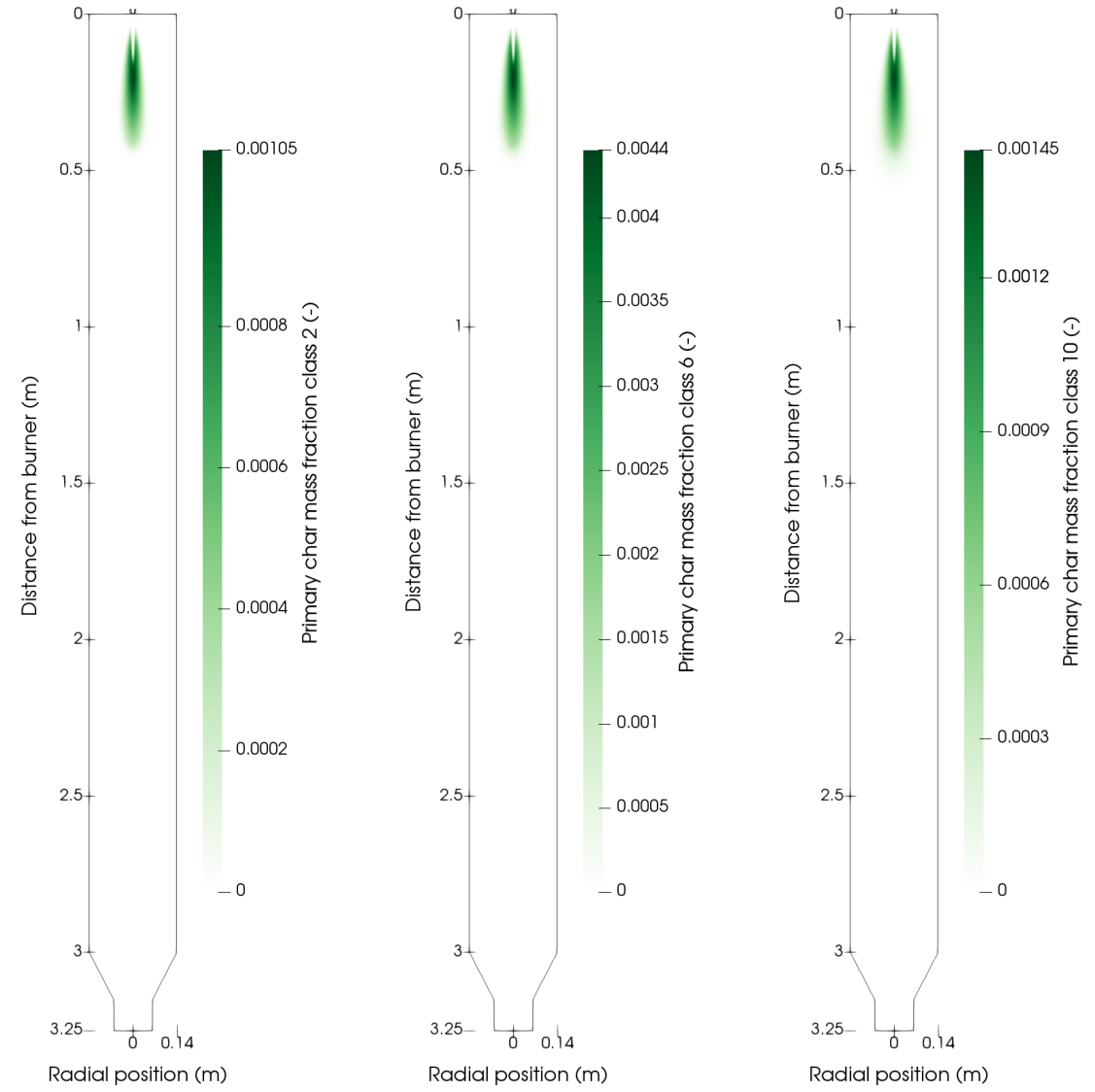

A) 2^{th} class B) 6^{th} class C) 10^{th} class

FIGURE C.2: CFD contours of the primary char mass fraction

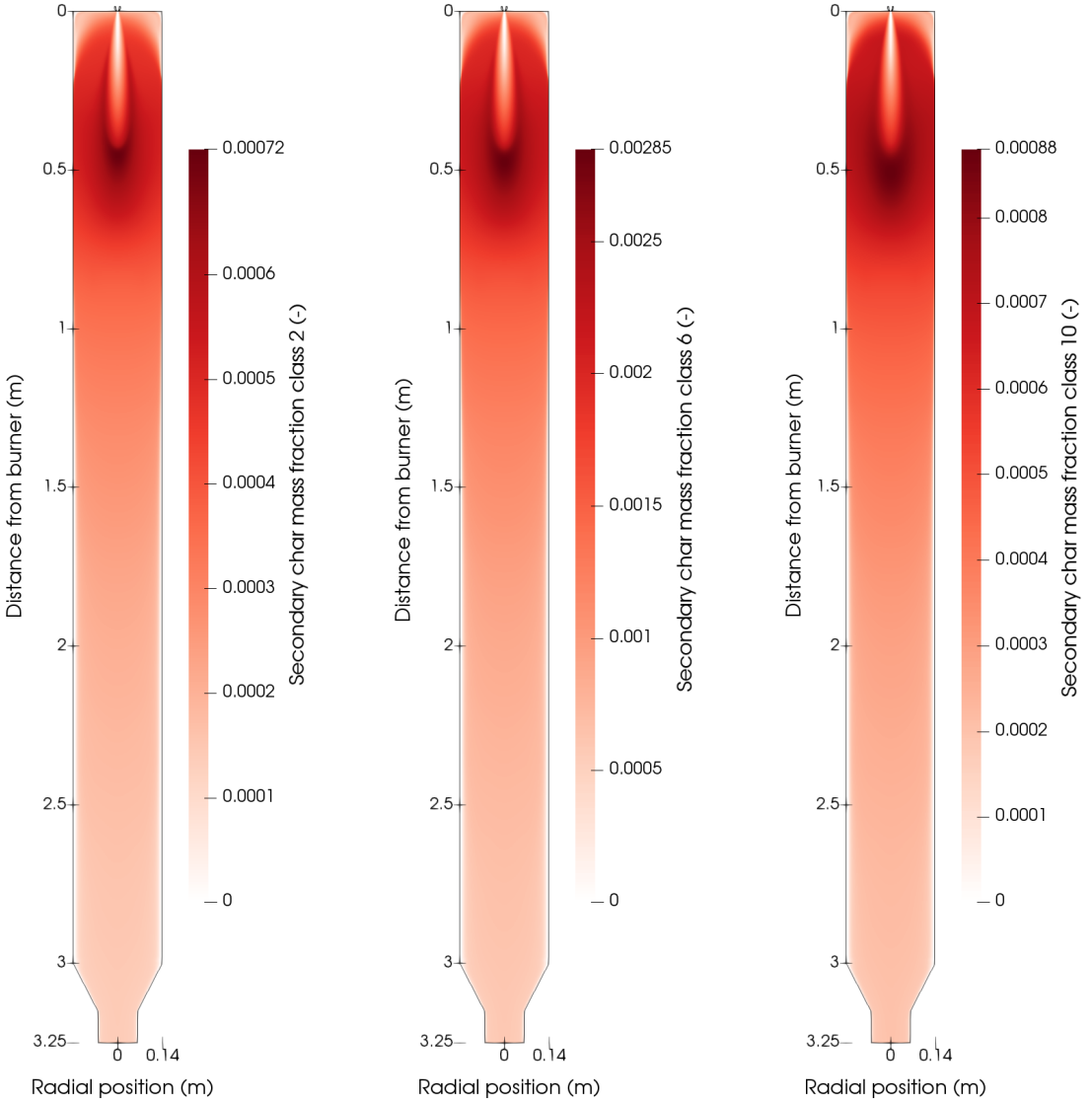

A) 2^{th} class B) 6^{th} class C) 10^{th} class

FIGURE C.3: CFD contours of the secondary char mass fraction

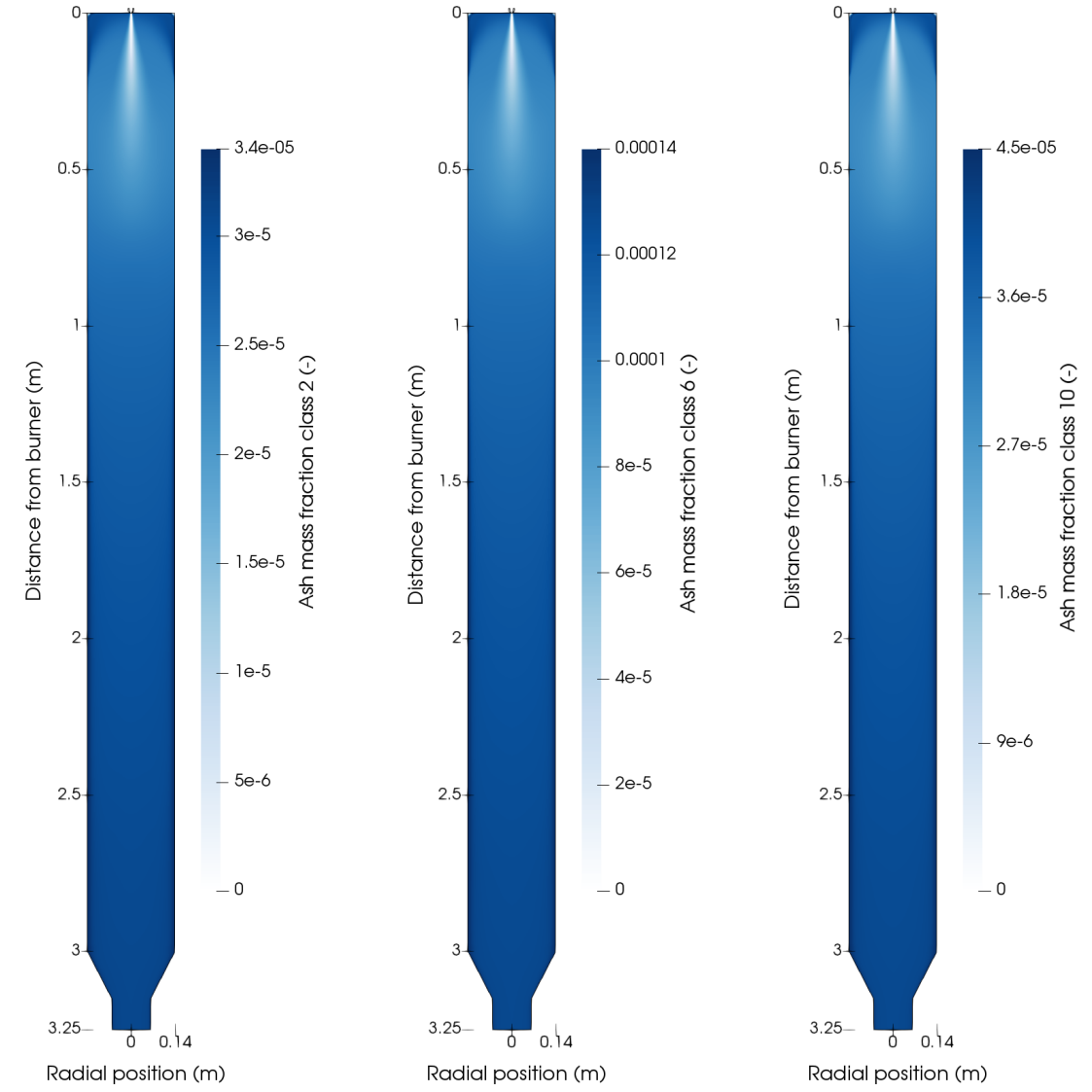

A) 2^{th} class B) 6^{th} class C) 10^{th} class

FIGURE C.4: CFD contours of the ash mass fraction

C.3 REGA-slurry2-T2

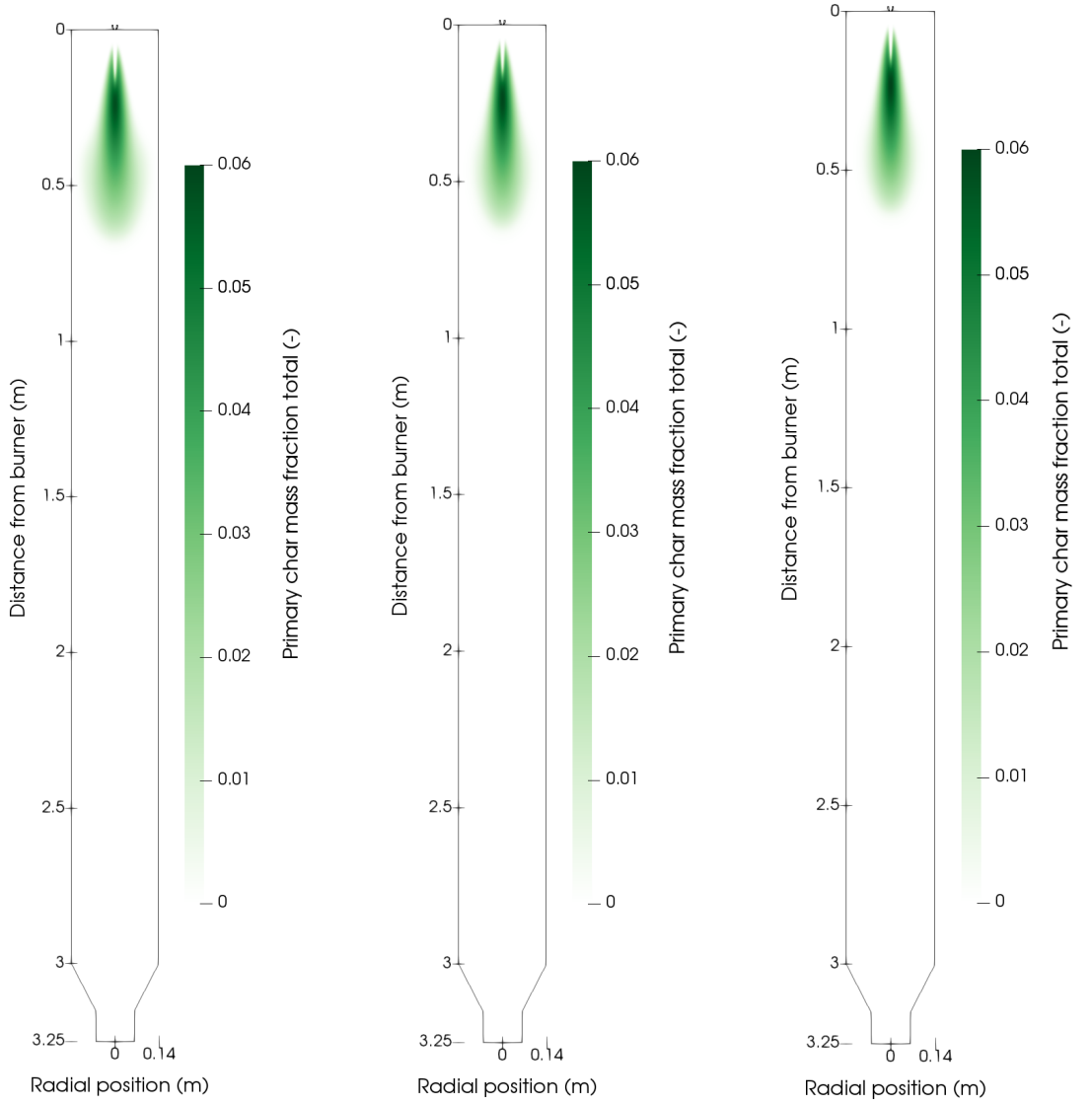

A) Simulation with $A_r^G/3$ B) Simulation with $A_{r,opt}^G$ C) Simulation with $A_r^G \cdot 3$

FIGURE C.5: CFD contours of the primary char total mass fraction

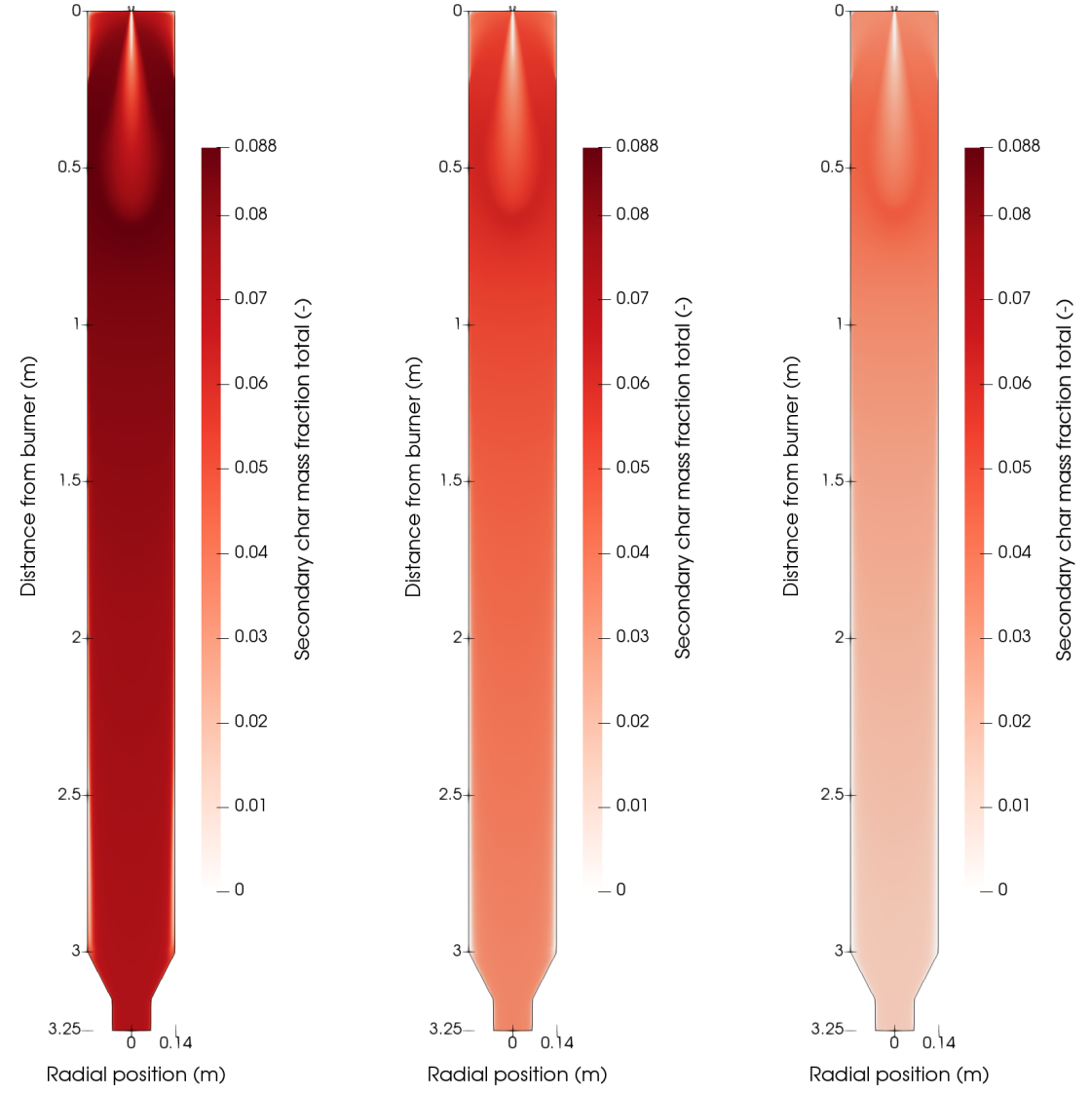

A) Simulation with $A_r^G/3$ B) Simulation with $A_{r,opt}^G$ C) Simulation with $A_r^G \cdot 3$

FIGURE C.6: CFD contours of the secondary char total mass fraction

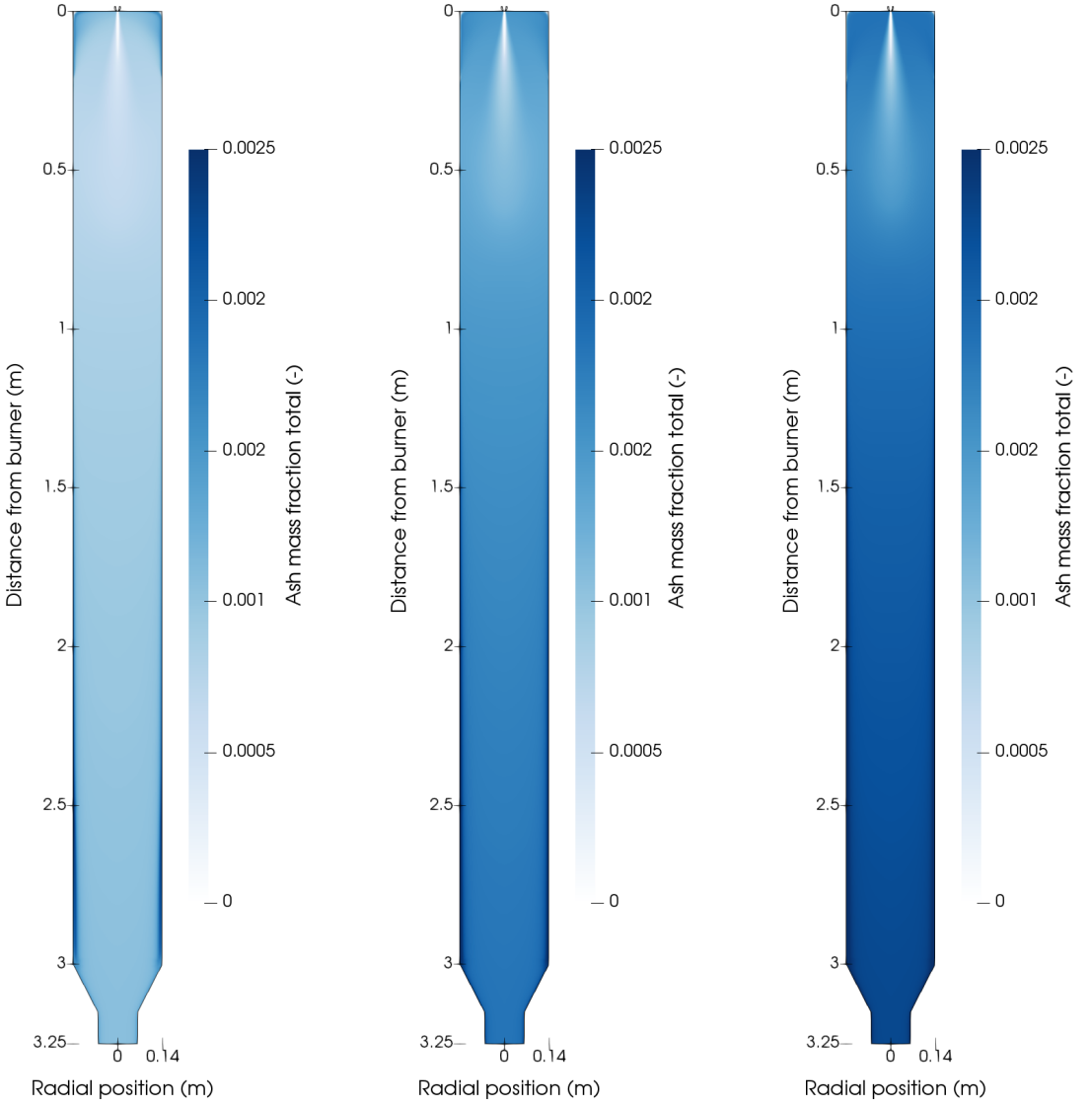

A) Simulation with $A_r^G/3$ B) Simulation with $A_{r,opt}^G$ C) Simulation with $A_r^G \cdot 3$

FIGURE C.7: CFD contours of the ash total mass fraction